# Development of a Non-Destructive Interfacial Imaging Technique

Edward Jackson

**Doctor of Philosophy**

University of York
Electronic Engineering

November 2019

# Abstract

An idea to utilise a scanning electron microscope to investigate buried interfaces within samples non-destructively has been developed. A repeatable methodology to apply this non-destructive interfacial imaging technique has been devised and tested. In addition a Monte Carlo simulation tool, CASINO, has been used to optimise the depth at which the imaging technique probes. This technique was further developed to study devices *in situ*. This was used to define and measure an effective area in lateral spin valves.

This technique has been applied to numerous systems, including thin films and devices. When used to investigate the effects of varying the Ta seed layer thickness in a series of Si/Ta/CoFeB/MgO/Ta thin films it identified differing densities of domain wall pinning sites, increasing as the seed layer became thicker. The effect on the magnetic moment was observed by sweeping a ±1 T field in a vibrating sample magnetometer. This identified a preferred seed layer thickness of 0.5 nm.

Magnetic tunnel junction devices were also investigated. These devices are designed for use in either data storage or magnetic sensor applications. The non-destructive imaging technique, as well as energy dispersive X-ray spectroscopy, was used to optimise the fabrication of these devices. This combined study increased the total yield by 15% by identifying the formation of an aluminium carbide along the edge of failed devices. Production quality devices were characterised using the non-destructive interfacial imaging technique. This demonstrated the varying dome on the pillar and also allowed the encapsulation layer to be measured.

The thin film for an organic magnetic tunnel junction was also investigated. The organic molecule, Cobalt(II) Phthalocyanine, was deposited in 0.32 and 3.2 nm thick layers. The non-destructive imaging technique identified the formation of channels in this organic layer. The channels were more dense in the 3.2 nm sample. Cross-sectional transmission electron microscopy was employed to investigate the structure. This identified the likely cause of these channels to be mis-orientation of the organic molecule during deposition. These results unambiguously prove the applicability of this imaging technique developed for interface assessment and improvement, for a wide variety of spintronic devices.

# Contents

# List of Tables

# List of Figures

# Acknowledgements

During my time on this work and the production of this thesis, I have found myself indebted to many individuals and wanted to take the time to acknowledge their support and contribution.

First and foremost I would like to thank my supervisor, Prof. Atsufumi Hirohata. Without his insight and guidance and infinite patience this project would not have become the success I feel it did. In addition I would like to thank Prof. Kevin O'Grady. The production of this thesis has benefited significantly from his encouragement and balanced review.

Secondly, the fellow post-graduates/doctorates I had the joy to work alongside. Will, Joe, John, Dan, Jun-Young, Ioan, Teo, Marjan and Kelvin, with your discussions, ideas, interest and friendship the whole ride was much easier.

Additionally I would like to thank all of my collaborators. Without your interest in this new technique the project would have been far less interesting and the materials studied would be far less varied. Without the support from JEOL UK this project would not have been possible. The technical expertise within the York-JEOL Nanocentre was also vital. In addition the support from the staff in the Department of Electronic Engineering was invaluable.

Finally I would like to thank my friends, family and particularly my fiancée. Without their support from the shadows my experiences during this time may have been very different. They have also helped me to develop a good answer for the hardest question 'so what is your PhD about?'.

# Author Declaration

I declare that this thesis is a presentation of original work and I am the sole author. This work has not previously been presented for an award at this, or any other, University. All sources are acknowledged as References.

Signed:

Edward Jackson

# Chapter 1

# Introduction

The first transistor, invented in 1947 [1], sparked a wave of research into solid state devices. This led to the development of the metal oxide semiconductor field effect transistor, the most widely used transistor type, in 1959 [2]. These transistors rely on precisely characterised materials and the production of devices with a known interface quality. Over time these transistors have been miniaturised placing more demand on production methods and creating a need for more precise characterisation techniques. This was driven by the need for increased computing power, following the proposed Moore's Law, where the number of transistors on a chip double every couple of years [3].

Alongside the development and miniaturisation of transistors, other computing components were being developed using new techniques and architectures. An example of one of these new developments is magnetoresistive random access memory (MRAM) [4]. MRAM is typically made from a complex multilayer magnetic thin film. This film is then shaped into nanostructures, usually with plasma etching or focussed ion beam (FIB) bombardment. The characteristics that make MRAM so suitable as a non-volatile replacement for high speed (>1 GHz) memory are highly dependent on the interface quality of the thin film [5]. This means that it is important to have a precise knowledge of the characteristics of these devices, particularly their interfaces. Being able to do measure these characteristics, not only aids optimisation, it also allows production devices to be tested for their quality.

As shown in fig. 1.1, there are many options to investigate devices or thin films. However not all of these options are suitable for probing a sub-surface interface. On the extreme ends of the graphs lie some for the better options

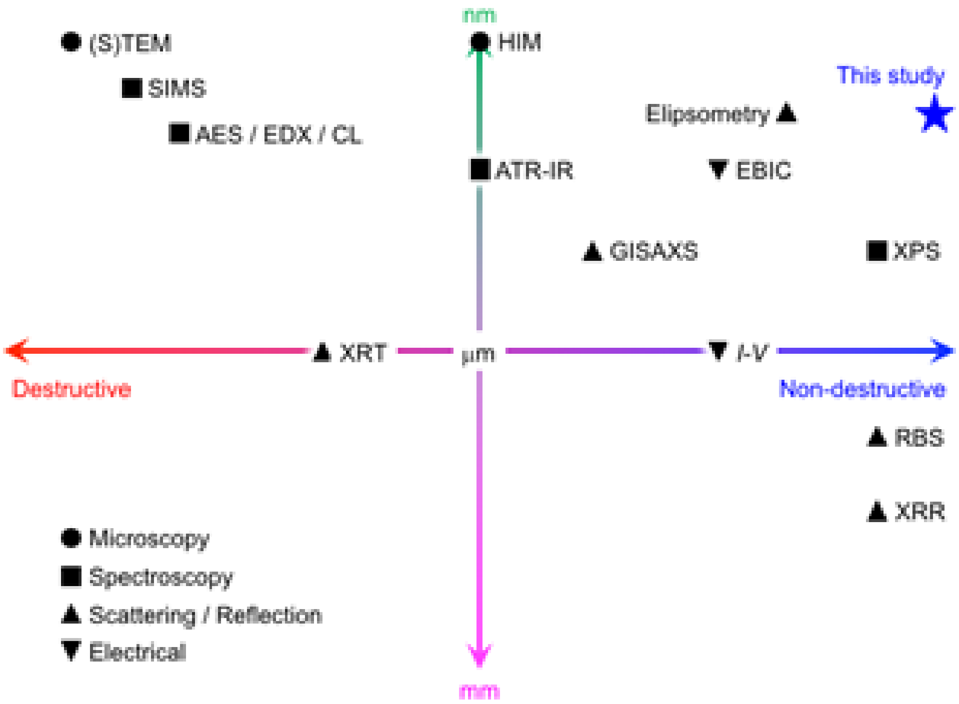

Figure 1.1: A representation of the current interfacial characterisation techniques available. This compares how destructive a technique is, including preparation for use, with the scale it works on [6].

to do this. Transmission electron microscope (TEM) and X-ray reflectivity (XRR) are both suitable for investigating the surface roughness and to estimate intermixing. XRR uses the total external reflection of X-rays to probe the interfaces within a sample [7]. This results in a distribution of X-ray intensity based on the angle of incidence of the coherent X-ray beam. This is then fitted with and optimised, starting with the best guess of the layer thickness of the sample. There is little preparation required for XRR, all that is needed is a highly clean sample surface, hence it is highly non-destructive. Whilst it can be used to measure layer thickness to the nearest 0.1 nm, XRR requires a sample to be uniform across a couple of mm, which means it is not suitable for device applications. Due to this only the macroscopic surface roughness can be measured, an average across the illuminated area. In addition the actual process of fitting requires a skilled user, to ensure that the results remain physical.

TEM, particularly the cross-sectional variant, provides atomic scale detail. It can image the atomic columns at an interface, allowing the surface roughness to be measured in terms of number of atoms displaced, and it is also useful for spotting dislocations and other crystal defects. TEM has a very small field of view, around 100 nm when trying to achieve atomic resolution, so it is suitable for investigating both devices and thin films. This smaller field of view does mean it is incredibly sensitive to the imaging area chosen. Whilst it is typically assumed, it is difficult to say that such a small area is representative of the whole sample. The biggest downsides of TEM are the time taken to prepare and image a sample and the incredibly destructive nature of the sample preparation process. As the sample needs to be <50 nm thick and polished, to allow for electron transmission, it is necessary to remove a lot of material from the sample of interest. The process of preparing the sample, described later in section 2.2 is irreversible, meaning that any findings from the TEM study have to be enacted in the next set of samples. This is fine in an iterative development, but less useful when testing the quality of production devices.

With the idea in mind that in both research and production there will be an interest in investigating devices at nm resolution in a non-destructive manner, this project was started. The aim for functionality of this new technique is marked as 'This Study' on fig. 1.1. The idea driving this technique, explained more fully in section 3.1.1, is that two electron images taken using a scanning electron microscope (SEM) at different accelerating voltages can be subtracted from each other. Due to the different sizes of the respective interaction volumes, this would leave behind only sub-surface information. If a tool was used to simulate and predict the exact difference between the sizes of these interaction volumes, the subtracted area could easily be calibrated to focus on an interface of interest. This would be able to be used to quickly analyse the interface over as large or a small and area as was needed, without damaging any of the samples under the beam.

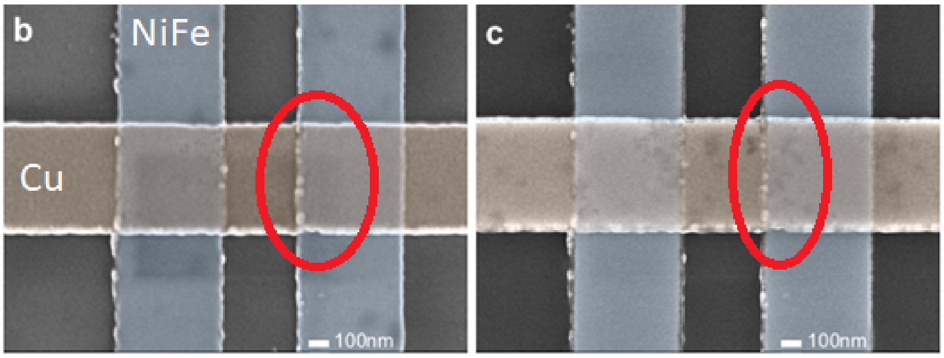

Figure 1.2: SEM images taken with an electron beam acceleration of b. 1 and c. 5 kV. These were used to demonstrate the differences in information that can be gathered at different accelerating voltages [6].

To ensure support for this project a demonstrative experiment was performed, and later published [6]. This acts as both the proof of concept and was the starting point for this study. Shown in fig. 1.2, images were taken of two crossing wires. One wire is 30 nm thick $Ni_{0.8}Fe_{0.2}$, with a blue false colour, and the other wire is 70 nm thick Cu, with an orange false colour. It is worth noting that the way the false colour was layered, placing one bar across the other, does make the interfacial region seem artificially different from the non-interface region. The accelerating voltages used were 1 and 5 kV. These images demonstrate a marked difference along the boundary between the two wires, circled in red. These visible features are attributed to imperfect bonding or a separation at the boundary.

Given this clear demonstration, the aim of this project was to further develop this concept into a usable tool. As part of this it would be necessary to produce an image processing tool, develop procedures, and test and define the limits of this technique. During the study the technique will be applied alongside more traditional techniques to both demonstrate its power and provide more information to assist with the optimisation or production of devices. The work that has gone into achieving these goals is detailed throughout the other chapters.

## 1.1 Units and Errors

Throughout this project most units that have been used follow the standard definition. In addition, there are occasional mentions of combined units, but these are defined as they appear. The most important non-SI unit used throughout this document is the electron volt (eV). This is defined as the amount of energy gained by the charge equivalent to a single electron when it is moved across a potential difference of one volt. One electron volt is equal to $1.602\times10^{-19}$ Joules.

A significant amount of this work is treated qualitatively. However there is also a large quantitative element. When handling errors associated with these measurements the usual methods for combining them are followed. However in almost all cases it has been a preference to instead take multiple readings and use the mean result and discuss the errors in the context of its standard deviation. There may be some cases where numbers have been stated without error. In most of these cases this will be due to the fact that the value is taken from literature and should be accompanied by its reference. However there may be cases where the error is not known and as such cannot be stated. When this occurs it will be discussed.

# Chapter 2

# Experimental Techniques

Given the task to develop a new technique to investigate sub-surface defects non-destructively it is important to understand fully the base equipment which will be used to develop the idea and the complimentary techniques that can be used to corroborate the results gathered. Initially this chapter will cover all the processes and underlying physics required to generate and direct an electron beam towards a sample an SEM. As well as the incident beam methods of detection for any of the resultant products will be discussed in detail. A comparison of the similarities and differences between a TEM and an SEM will then be made covering the aspects which vary in detail.

The correct microscope is important, but there are also benefits to ensuring that the sample and particularly its surface are well prepared. This will also be covered alongside methodology to reduce charging in non-metallic samples. A different technique, energy dispersive X-ray spectroscopy (EDX), was also used during the investigation to provide more detailed elemental information. The merits and limitations of this will also be discussed. This chapter strongly follows the work done in Goldstein *et al.* [8] when discussing the SEM and the work by Williams and Carter [9] in reference to TEM.

## 2.1 Scanning Electron Microscopy

An SEM uses a filament to emit electrons which are then focussed into a beam by lenses. This beam is rastered across the surface of a sample by a deflection system where the step size controls the magnification. Whilst the beam is rastered detectors gather signal information and that is converted to a displayable image for the user. A user needs to be sufficiently skilled to be able to manipulate all of these factors and interpret the data. For this reason a detailed analysis of each step in the creation of an image will be described. Additional focus will be given to those factors relevant to the machine used, i.e. the JEOL JSM-7800F *Prime*. There are a few unique features of this machine, even before modifications for the study were made, there will be significant reference to material taken from the machine's user manual, [10].

### 2.1.1 Electron Sources

Electron microscopes all require a source of electrons that can provide a stable beam of electrons with a current that can be calibrated reliably, commonly referred to as electron guns. There are two main categories of gun: thermionic guns and field emission guns. Each of these categories have their own characteristics, advantages and disadvantages for use which will be discussed in relation to the needs of this project.

The most important properties of an electron gun are brightness, energy spread and stability. The stability of the electron source measures how much the emission current varies with time, typically per hour. A low stability causes problems with the exposure for images as well as any attempted microanalysis. Brightness, $\beta$, is a measure of the current density per unit area and it is given by [9]:

$$\beta = \frac{\text{current}}{\text{probe area} \times \text{solid angle}} = \frac{4i_e}{\left(\pi d_0 \alpha_0\right)^2} \tag{2.1}$$

where $i_e$ is the total emission current, $d_0$ is the diameter of the crossover or focus point and $\alpha_0$ is the beam divergence. This is an important parameter as it directly impacts the intensity of the signal used for imaging. Brightness scales linearly with acceleration voltage. Also higher brightness values allows the beam to be focused to a smaller spot size whilst still having a usable value of $i_e$. The brightness is strongly affected by the size of the source. As the source gets smaller the brightness increases.

It is important to know what wavelength an electron has at a given kinetic energy. This can indicate how it will interact with lenses and also creates a limit on how large a source of electrons can be, that still produces coherent light. This wavelength, $\lambda$, is given by:

$$\lambda = \frac{h}{\sqrt{2m_0eV}} \tag{2.2}$$

where $h$ is Planck's constant, $m_0$ is the rest mass of the electron, $e$ is the charge of an electron and $V$ is the applied acceleration voltage. This equation is based on the ideas of wave-particle duality proposed by de Broglie stating the momentum in terms of acceleration voltage.

Another parameter that is strongly dependant on the source size is the spatial coherence. If spatial coherence was perfect, all electrons would be emitted from exactly the same point. As the source size increases, spatial coherence decreases. The effective source size for coherent illumination, $d_c$, is given by:

$$d_c << \frac{\lambda}{2\alpha_S} \tag{2.3}$$

where $\lambda$ is the electron wavelength and $\alpha_S$ is the angle subtended by the source on the specimen. Equation (2.3) demonstrates that smaller source sizes increase spatial coherence. It also indicates that using smaller apertures within the beam line, which reduces $\alpha_S$, increases the spatial coherence. Larger coherence is responsible for a more parallel beam. This improves the quality of diffraction patterns and increases the spatial resolution.

Another type of coherence, temporal coherence, measures the energy spread of the electrons. High temporal coherence ensures that the electrons all have the same wavelength, i.e. are monochromatic, which is important for very high resolution applications. A measure of temporal coherence is the coherence length, $\lambda_c$ given by:

$$\lambda_c = \frac{\overline{\nu} h}{\Delta E_B} \tag{2.4}$$

where $\overline{\nu}$ is the electron velocity, $h$ is Planck's constant and $\Delta E_B$ is the energy spread of the beam. This coherence is strongly dependent on the hardware in place within an electron microscope particularly the stability of both the electron source and the power supply.

$\Delta E_B$ represents the range of electron energies leaving the source within the gun. The spread of electron energies are typically measured with a hemispherical electron energy analyser [11]. This measures the electron energies at a position close to that of the sample incidence. The energy spread is then measured as the full width at half maximum of the distribution. As this project requires control over the depth of penetration of electrons within the sample this is a very important parameter.

### Thermionic Electron Guns

There are two main types of thermionic gun: the tungsten filament gun and the Lanthanum Hexaboride ($LaB_6$) gun. The tungsten filament electron gun is the oldest commonly used device, favoured for its reliability and low cost [12]. The fact that it has over 70 years of development also means that it is well understood [13]. This electron gun is made from three parts: a wire filament cathode, a negatively biased grid cap and an anode plate. A schematic diagram of the device is shown in fig. 2.1.

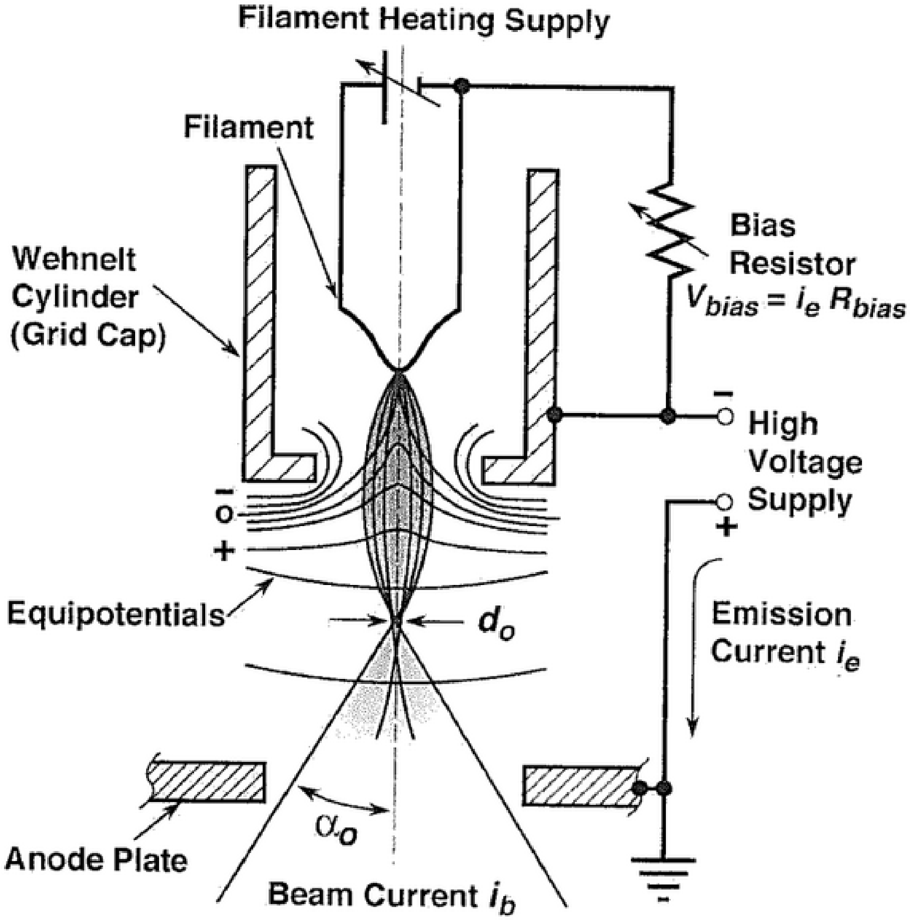

Figure 2.1: A tungsten hairpin filament, a self-biasing thermionic electron gun, [8].

The wire filament cathode is the source of electrons within the electron gun. This traditionally uses a tungsten wire with a diameter of approximately 100 $\mu$m, which is bent into a v-shaped hairpin filament. This results in a typical tip size of approximately 100 $\mu$m. The electron source is thermionic. This means the electron emission is only significant when the filament is white hot, between 2000 and 2700 K. The wire is heated using resistive heating providing an area of approximately 0.01 mm$^2$ which emits thermionic electrons in a broad cone towards the anode through the focussing grid cap. The current density, $J_C$, for thermionic sources is given by:

$$\mathrm{J_C} = \mathrm{A_C T^2} \exp\left( - \frac{\Phi}{\mathrm{k_B T}} \right) \tag{2.5}$$

where T is the temperature, $\Phi$ is the work function, $k_B$ is the Boltzmann's constant and $A_C$ is the Richardson's constant. The Richardson's constant [14] is dependent on the source material and values can be found listed in the literature [15].

As already described the tungsten wire filament has a source size of approximately 100 $\mu$m. With an acceleration voltage of 20 kV the brightness of this electron source is found to be $10^5$ A/cm$^2$ sr using eq. (2.1). The size of the source ensures that a large amount of electron optics needs to be in place to ensure a small enough spot size to investigate a sample. It also means that the spatial coherence is not ideal for high resolution applications. The energy spread of the electrons emitted by the tungsten filament is $\pm 3$ eV. Whilst this is not a large value it does mean that at low acceleration voltages ($<5$ kV) the temporal coherence is very low making it an unsuitable gun for the development of this technique. Despite its unsuitability, there are several positive aspects to the use of tungsten filaments. For example the stability of the gun is excellent. It varies by $<1\%$ in an hour. The gun is also able to operate in a vacuum of only $10^{-2}$ Pa. This makes it ideal for the investigation of pressure sensitive samples such as cells or other biological specimens.

$LaB_6$ is a single-crystal replacement for the tungsten filament in the thermionic emission gun described above [16]. The crystal has a lower work function, $\Phi$, ($LaB_6$ - 2.7 eV, W - 4.54 eV) and a much lower Richardson constant, $A_C$, ($LaB_6$ - 29, W - 60) when compared to tungsten. When inspecting eq. (2.5) it can be seen that this results in a much higher current density from $LaB_6$ at the same temperature. At the same time the crystal can be polished to a point which is approximately 1 $\mu$m. This enhances the effect of the electric field at the tip, lowering the barrier for electron escape. Simultaneously the small area of the tip makes for a smaller crossover size. This results in a brightness of approximately 10 times that of tungsten, $10^6$ A/cm$^2$ sr. The reduced area also increases spatial coherency. These improvements make it a much more ideal choice for the development of this technique.

$LaB_6$, shown in fig. 2.2, is produced as a unit ready to replace the tungsten filament in the electron gun setup shown in fig. 2.1. To accommodate the $LaB_6$ electron gun a small adjustment to the bias voltage needs to be made, alongside a slight adjustment of the grid cap. As the crystal is prone to contamination it is necessary to keep it at higher vacuum, approximately $10^{-4}$ Pa, compared to that required for tungsten of approximately $10^{-2}$ Pa.

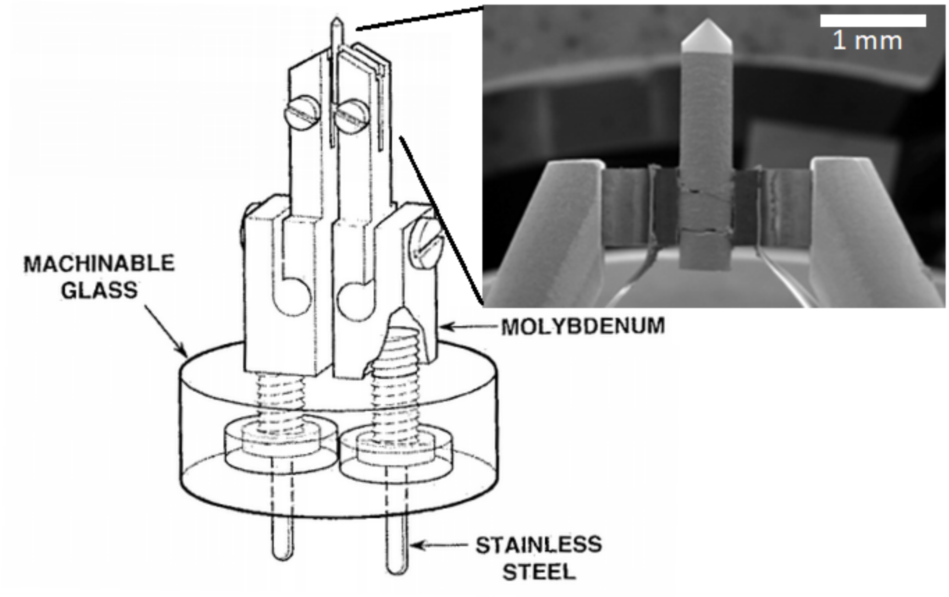

Figure 2.2: A $LaB_6$ electron source. The single crystal and its housing is magnified, [8].

A $LaB_6$ gun is also heated resistively. The current for this heating is passed through the support rods, shown in fig. 2.2. These rods are made of either graphite or rhenium as the two materials do not react with the crystal. This setup and the properties of the crystal not only provide a brightness upgrade and a significant improvement to spatial coherency when compared with tungsten, the energy spread is also improved. At 20 kV this spread is ±1 eV. This makes it more suited to low energy applications. As the beam stability is also approximately 1% an hour this makes it a very suitable candidate for the needs of this project.

### Field Emission Electron Guns

Thermionic electron sources all require high temperatures to release electrons. A cold field emission gun uses an applied potential, concentrated at its tip, to lower the potential barrier allowing electrons to be excited via the tunnelling effect [17]. This tip will typically have a radius of <100 nm and a virtual source size of <5 nm. Tungsten is the usual material for this tip as it

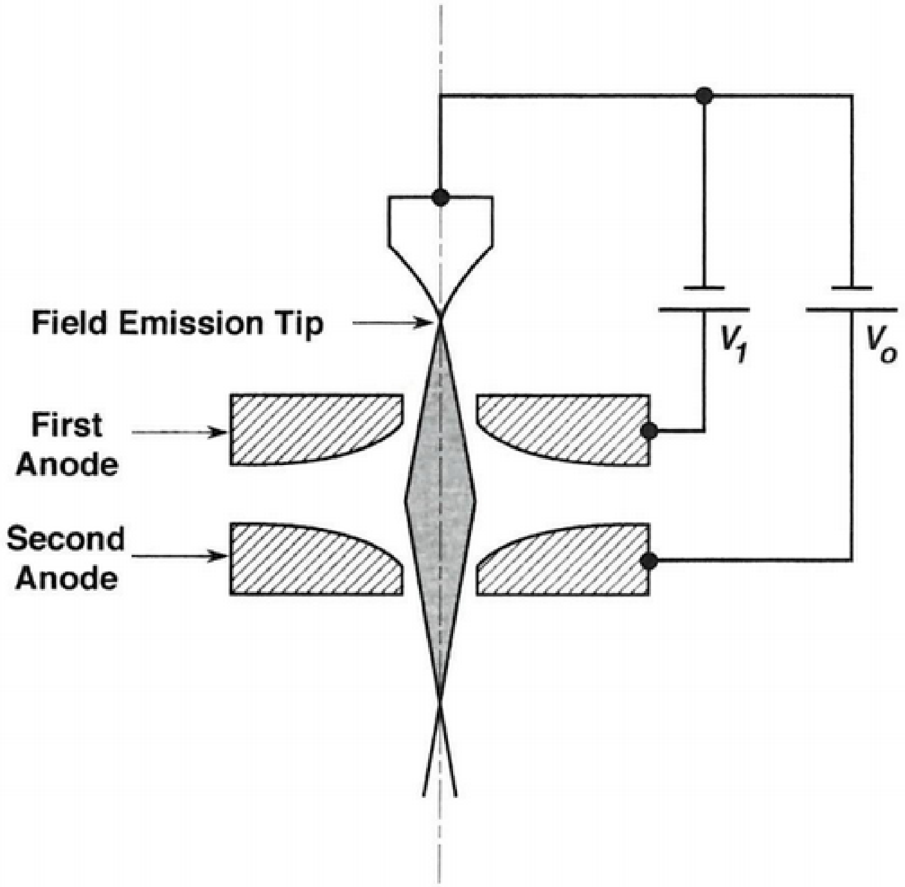

Figure 2.3: A Butler triode field emission source, [8]. $V_1$ is applying the 10V/nm field to assist tunnelling. $V_0$ accelerates the emitted electron to the acceleration voltage.

is mechanically robust, but carbon and silicon nanotubes have also been used [18]. This tip is then supported by a tungsten filament. The typical setup utilises two anodes, shown in fig. 2.3. The second anode is responsible for accelerating and focussing the emitted electrons. The first is responsible for applying a field of 10 V/nm to the tip to facilitate the tunnelling effect. The current density, $\mathrm{J}_C$, for field emission sources is given by [19]:

$$\mathrm{J_C} = k_1 \mathrm{E}_{ap}^2 \exp\left( - \frac{k_2 \Phi^{3/2}}{\mathrm{E}_{ap}} \right) \tag{2.6}$$

where $\mathrm{E}_{ap}$ is the applied electric field and $k_1$ (typically 1.54 $\mu$eVV$^{-2}$) and $k_2$ (approximately 6.83 eV$^{-3/2}$Vnm$^{-1}$) are the first and second Fowler-Nordheim constants respectively [20]. These were named after Fowler and Nordheim as they proposed the theory of field emission from bulk metals [19].

This set up achieves a brightness of approximately $10^8$ A/cm$^2$ sr at 20 keV due to both the small source size and the strong confinement of the beam.

In addition this is achieved without any heating within the source. The lack of heating allows an energy spread of 0.3 eV to be achieved. This makes it an excellent source for low energy applications. This performance relies on a pristine tip. If the cathode is not atomically clean the emission current can fluctuate by $>>5\%$ per hour. The tip can be heated rapidly, or flashed, to remove any gas molecules giving a clean tip before use. The use of ultra high vacuum, approximately $10^{-8}$ Pa, also reduces the rate of gaseous build up allowing for sustained imaging. The difficulty of maintaining such a vacuum within an SEM and the fact that even with the ultra high vacuum the emission fluctuation is still approximately 5%, means that a cold field source is not suitable for a lot of applications, including this investigation, despite its ideal energy spread.

The Schottky emitter is a hybrid tip. Instead of ending in a monoatomic tip it is flattened to create a single facet with a larger radius that is able to maintain a virtual source size of approximately 20 nm. Just like with the cold field emission gun a field is applied to the tip, lowering the work function. Due to the larger size of this source a coating of zirconium dioxide, $ZrO_2$, is applied to the surface to further reduce the work function [21]. The tip is also kept at between 1700 and 2000 K to ensure the surface is clean even when not in use. This also assists the emission of electrons. The setup is similar to the one shown in fig. 2.3 with the addition of a suppression grid above the first anode, designed to reduce excess thermionic electrons. This setup results in a thermionic emitter which has the brightness similar to that of the cold field emitter of approximately $10^8$ A/cm$^2$ sr at 20 keV [22].

As well as ensuring a clean surface the application of heat to the tip increases stability to around 1% per hour. This also allows the tip to be used in lower vacuums, approximately $10^{-6}$ Pa, although in practice an ultra high vacuum is used to ensure longevity of the sample. Whilst the implementation of a suppression grid helps, heating the Schottky emitter does broaden the energy spread when compared with a cold field emitter to between 0.3 and 1 eV depending on the system. This range is very useful for low energy operations. The source size also has a surprising benefit as it allows for a larger range of spot sizes when compared with the cold field emitter despite the extra demagnification required for high resolution imaging.

Overall the Schottky emitter proved to be the most practicable electron source for this project and is part of the reason the JEOL JSM-7800F *Prime* has been employed. The Schottky emitter within the SEM is similar to the standard one described above. It utilises a tungsten tip flattened across the $< 100 >$ surface, where zirconium oxide is applied. The cathode is maintained at 1800 K with a vacuum of $10^{-7}$ Pa. This source has an energy spread of between 0.3 and 0.7 eV. In this case the acceleration voltage which can be applied by the anode is between 0.1 and 30 kV. This range is in 10 V steps between 0.01 and 2.9 kV and 100 V steps from then on.

### 2.1.2 Creating a Probe

Electron lenses are used to demagnify the beam to the spot size required by the user. They also shape and guide the beam along the column to the sample. Electron lenses are either electrostatic or electromagnetic. Within an SEM electromagnetic lenses are exclusively used as they create smaller aberrations than electrostatic lenses. Despite this it is still necessary to employ beam limiting apertures both at the source and within the column of SEMs. An aperture is typically a circular hole of a chosen diameter, usually between 0.5 and 0.1 mm, within a diaphragm which is usually made of platinum. These apertures are responsible for allowing a certain diameter of electron beam through. The diaphragm excludes the other electrons by simply being opaque to them.

In general electromagnetic lenses, an example shown in fig. 2.4, consist of a coil of wire or windings which create a field, and polepieces which focus the field to the required position. This simple design leads to an expression for focal length, $f$, given by [9]:

$$f = \frac{V_0}{(NI_c)^2} \tag{2.7}$$

where $V_0$ is the beam acceleration voltage, $N$ is the number of turns in a coil and $I_c$ is the current through the coil. A quick inspection of eq. (2.7) shows that, unlike optical lenses, $f$ can be adjusted by changing $I_c$. This allows the demagnification to be changed as well. When $V_0$ is changed this also adjusts $f$, but all modern SEMs account for this automatically.

To understand exactly how these lenses demagnify an electron beam it is necessary to look to the Lorentz force, $\overline{\mathrm{F}}_L$. This describes the force on a charge, $q$, travelling through an electric and magnetic field. The Lorentz force is given

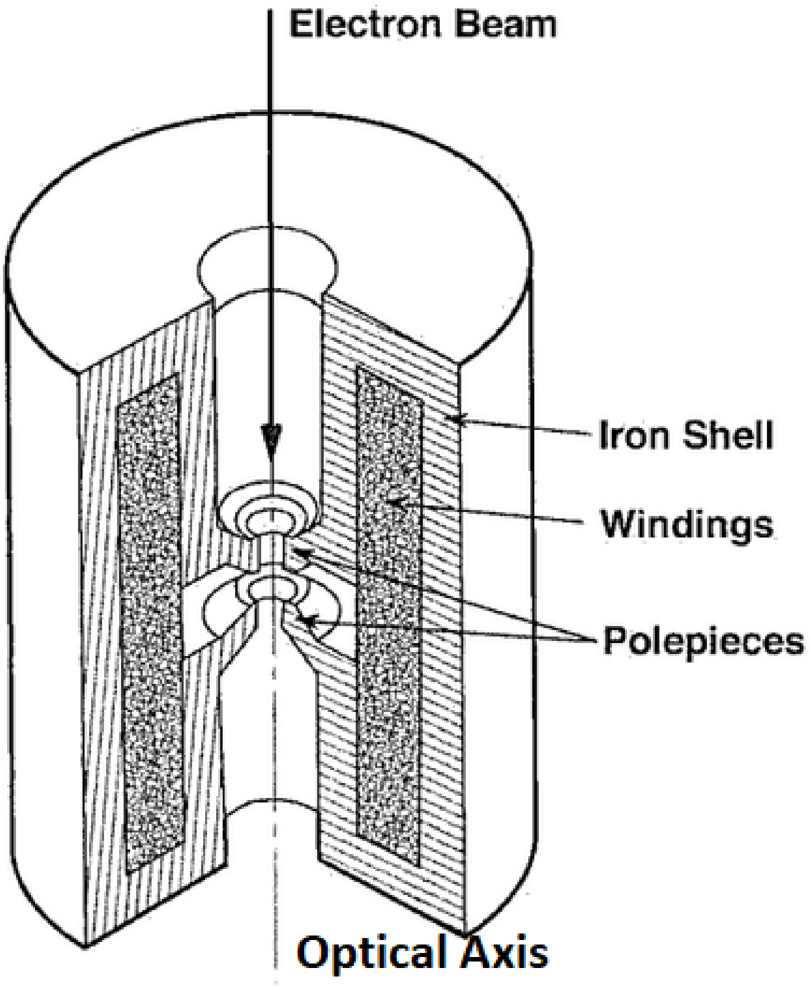

Figure 2.4: An electromagnetic focussing lens, [8].

by:

$$\overline{\mathrm{F}}_L = q(\overline{\mathrm{E}} + \overline{\nu} \times \overline{\mathrm{B}}) \tag{2.8}$$

where $\overline{\mathrm{E}}$ is the electric field strength, $\overline{\mathrm{B}}$ is the magnetic field strength, $q$ is the electrostatic charge (in this case $e$) and $\overline{\nu}$ is the velocity of the electrostatic charge. An electron travelling through the field at less than 90° from $\overline{\mathrm{B}}$ will helically spiral towards the optical axis [23]. This motion results in a narrower, demagnified beam.

### Lenses within the JSM-7800F *Prime*

An SEM has several different electromagnetic lenses within it. There are the condenser lenses, the objective lens and the scanning coils. As there are lots of different designs of lenses only the ones included within the JEOL JSM-7800F *Prime* will be covered. In this case the condenser lens is a two stage electromagnetic lens, the objective lens is a variant on a snorkel lens and there is an electromagnetic aperture-angle control lens.

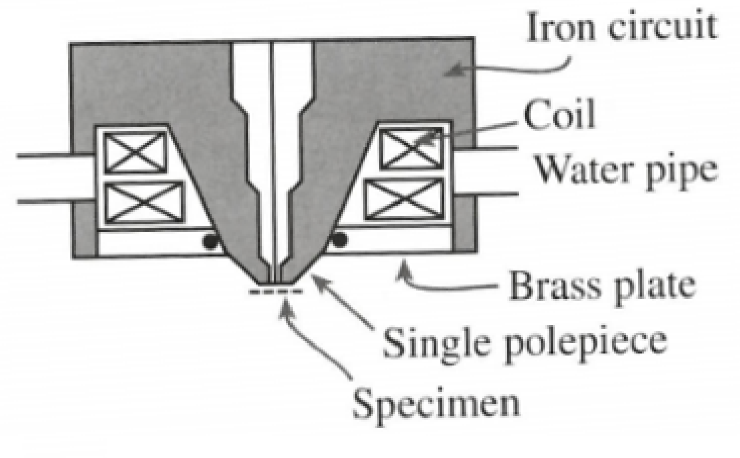

Figure 2.5: A typical snorkel lens. The scanning coils, stigmators and apertures have been excluded for simplicity, [9].

Condenser lenses look similar to the schematic shown in fig. 2.4. Within this SEM the two lenses are controlled simultaneously to demagnify the beam to the required spot size. The most important lens within the SEM is the objective lens. As already stated this is a snorkel lens in the JEOL JSM-7800F *Prime*. The snorkel lens is an iteration or combination of two previous lens types, the immersion lens and the pinhole lens [24]. It takes the best attributes from both, being designed in a way which extends the magnetic field below the polepiece onto the sample, allowing for a large range of sample sizes like the pinhole lens. In extending the field onto the sample like an immersion lens, lens aberrations are greatly reduced when compared with other lens designs.

As the objective lens provides several times (typically 1 T) the field that the condenser lenses do they are almost always water cooled. As well as having a more intricate geometry to allow for probe focussing, the objective lens also contains the stigmators. Stigmators are used to correct a large number of distortions in the beam which are discussed in section 2.1.2. The objective lens in an SEM also has to house the scanning coils. These are two pairs of small coils housed in or above the objective lens, which use an applied voltage to create a magnetic field which can deflect the beam. This allows the probe to be rastered across the surface, with the first set of coils bending the beam away from the optical axis and the second bending it back at the desired crossover point.

### Aberrations

Whilst lenses are an essential part of beam production, they introduce their own problems. Electromagnetic lenses have many different kinds of defects [25] whose contributions culminate to produce four distinct issues: spherical aberration, aperture diffraction, chromatic aberration and astigmatism. However whilst these defects do limit the resolution they are responsible for the impressive depth of field seen within electron microscopes.

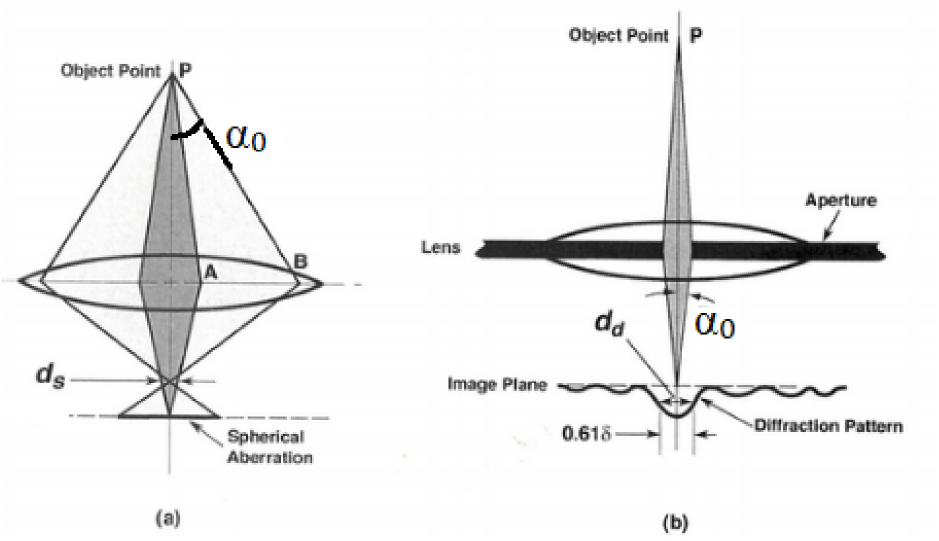

Figure 2.6: Aberrations found in an electromagnetic lens. (a) is spherical aberration and (b) is aperture diffraction, [8].

Spherical aberrations, shown in fig. 2.6(a), occur as electrons passing through the lens further from the optical path experience a stronger focussing force. These electrons have a crossing point which is closer to the lens. This results in a disk as opposed to a spot as intended. The point where this disk is smallest is known as the disk of least confusion. This is found above the image plane. A measure of the diameter of this disk, $d_\mathrm{s}$, is given by [8]:

$$d_\mathrm{s} = \frac{1}{2} C_\mathrm{s} \alpha_0^3 \tag{2.9}$$

where $C_\mathrm{s}$ is the spherical aberration coefficient and $\alpha_o$ is the angle the outer ray subtends with the lens. Spherical aberration is felt most at the objective lens where it has a direct effect on the resolution. $C_\mathrm{s}$ is approximately equal to $f$. Therefore an objective lens with a short $f$ is preferred. An alternative way to reduce the spherical aberration is to limit $\alpha_o$ by employing a small aperture. Whilst this would reduce $d_\mathrm{s}$ it would also act to reduce the beam current. Also if the aperture is small enough an effect known as aperture diffraction may be seen.

Aperture diffraction, shown in fig. 2.6(b), stems from the wave-like nature of electrons. When the beam passes through a small enough aperture a circular diffraction pattern is observed instead of a point as expected. This creates an intensity distribution known traditionally as the Airy disk. It has been shown [26] that half the diameter of the Airy disk can be taken to be the contribution of the aperture diffraction to the spot size, $d_{\mathrm{d}}$. This is given by:

$$d_{\mathrm{d}} = \frac{0.61\lambda}{\alpha_a} \tag{2.10}$$

where $\alpha_a$ is the angle subtended after the aperture, marked in fig. 2.6(b). These two aberrations have opposing relationships. This requires an optimum at each beam energy to be found to ensure the smallest probe size.

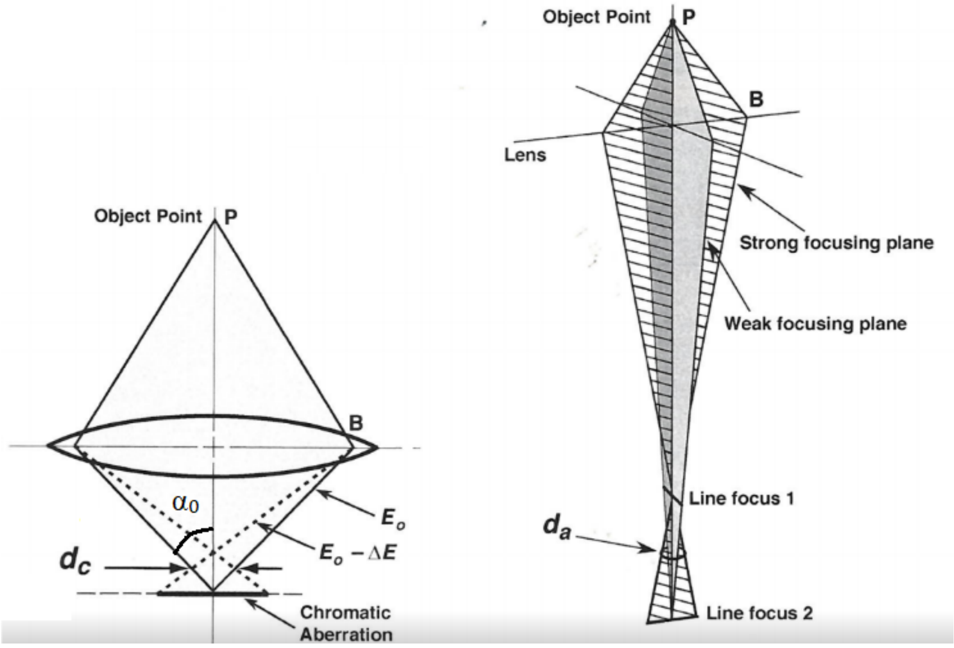

Figure 2.7: Aberrations found in an electromagnetic lens. (a) is chromatic aberration and (b) is astigmatism, [8].

The field in a lens will focus electrons of different energy to different points. This is known as chromatic aberration, shown in fig. 2.7(a). Once again this can be defined by a disk of least confusion, $d_{\mathrm{c}}$, given by:

$$d_{\mathrm{c}} = C_c \alpha_0 \frac{\Delta E_B}{E_B} \tag{2.11}$$

where $C_{\mathrm{s}}$ is the chromatic aberration coefficient, $\alpha_0$ is the beam convergence angle, $\Delta E_B$ is the energy spread of the beam and $E_B$ is the beam energy. The solution to this problem is to reduce $\Delta E_B$ through the electron gun or the power supply. In this case, choosing an SEM with a Schottky emitter has done that. As power supplies are extremely stable the electron gun is the dominating factor [27]. As $\Delta E_B$ is fixed, it ensures that chromatic aberration has a larger effect on the spot size as $E_B$ is reduced.

The final source of deviance is astigmatism, shown in fig. 2.7(b). Astigmatism stems from defects in the lenses, dirt on the apertures or misalignment in the lens system. These imperfections present a non-uniform magnetic field to a travelling electron, deviating it from the optical axis. This results in a beam that is distorted in the x or y plane, essentially a non-circular probe is created. Each system will experience a unique astigmatism that is potentially ever-changing. Thankfully astigmatism within the whole system is easily accounted for using stigmators. Stigmators are octupole electromagnets, typically housed within the objective lens, that apply a weak variable magnetic field to the beam path compensating for the astigmatism. The stigmators are entirely controlled by the SEM user.

### Probe Diameter

The resolving power of an electron microscope is dependent on both the probe size and the current at the probe. The lens system as well as the source will accumulatively effect both of these values but it is possible to estimate them. In an ideal aberration free world, this can be done simply using the brightness of the beam, $\beta$, as that is constant throughout the column. This results in an aberration-free probe diameter, $d_{\mathrm{G}}$, given by [9]:

$$d_{\mathrm{G}} = \sqrt{\frac{4 i_{\mathrm{p}}}{\beta \pi^2 \alpha_{\mathrm{p}}^2}} \tag{2.12}$$

where $i_{\mathrm{p}}$ is the probe current and $\alpha_{\mathrm{p}}^2$ is the probe convergence angle.

It is clear from the discussion in section 2.1.2 that this is not the case. To obtain a more realistic approximation of the actual probe diameter, $d_{\mathrm{p}}$, the terms for each of the aberrations can be added to $d_{\mathrm{G}}$ in quadrature [28].This new approximation is given by:

$$d_{\mathrm{p}} = \sqrt{d_{\mathrm{G}}^2 + d_{\mathrm{c}}^2 + d_{\mathrm{d}}^2 + d_{\mathrm{s}}^2} \tag{2.13}$$

where each of the terms are defined in eq. (2.9) through to eq. (2.12).

This simplistic addition does not hold true for low energy beams <1 keV as the low velocity of the electrons means they interfere with each other, via

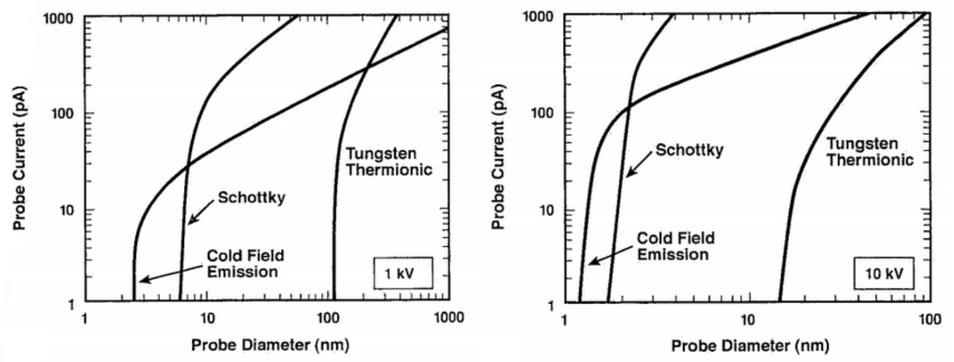

Figure 2.8: The relationship between $d_\mathrm{p}$ and $i_\mathrm{p}$ for different sources at both 1 and 10 keV, [8].

an interaction known as the Boersch effect [29]. The Coulomb interactions between the electrons widen $\Delta E_B$ increasing the effects of chromatic aberration further. This effect increases with $\mathrm{J}_C$ and decreases with $E_B$. This necessitates another approach that is more rigorous than simply adding the factors in quadrature to estimate the probe diameter and shape. Shao and Crewe [30] proposed an analytical wave-optical treatment that proves more than sufficient. A representation of the probe diameter with current at both 1 and 10 keV is shown in fig. 2.8. Here the Schottky emitter has been paired with a snorkel objective lens identical to the setup in the JEOL JSM-7800F *Prime*.

### 2.1.3 Detecting Electrons

So far electrons have been produced, focused on to the sample and then rastered across the surface. Chapter 3 covers in great detail the interactions that then occur and the resultant detection products. For the sake of SEM imaging only two products are of concern, backscattered electrons (BSEs) and secondary electrons (SEs). Section 3.1.3 covers the differences in detail, but in general SEs are electrons that escape the sample with <50 eV and BSEs are any with >50 eV. BSEs are expected to have undergone a handful of interactions within the sample, meaning they provide good contrast and depth information. SEs will have undergone many more interactions or have been produced with low energy in the top 5-20 nm of the sample. This generates a lot of surface information, but these electrons do not contain information on the chemical composition as they have interacted many times. Given this knowledge it is important to understand how a detector can leverage these differences to selectively image the electrons or to utilise both types at once.

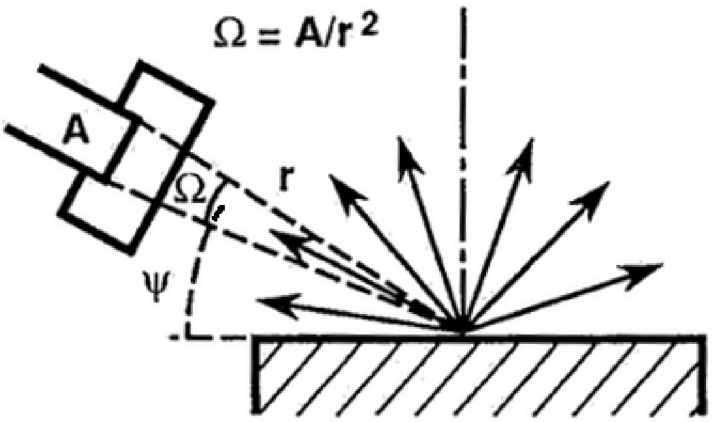

Figure 2.9: General characteristics of detectors, [8].

When discussing electron detectors there are several factors which must be considered. First, the detectors position in relation to the sample. This is typically described by the take-off angle, $\Psi$. This is the angle between the point of beam incidence and the centre of the detector, measured from the sample surface as shown in fig. 2.9. It is also important to note the detectors size, or collection area. This is measured by a solid angle, $\Omega$, also shown in fig. 2.9. $\Omega$, measured in sr, is the ratio of the detectors active area to the distance to the point of beam incidence squared. $\Omega = A/r^2$.

Next the detectors efficiency must be considered. This is a measure of how much of the radiation that enters the detector is converted into signal. This is likely to vary within a detector, depending on the energy of the incident radiation. It is worth noting the bandwidth of the detector and amplification system as well. As the SEM builds an image by rastering the beam across the surface, spatial details are measured as changes in the signal over time. This means that continuous regions will have a low frequency and regions with more features will be recognised with a higher frequency. This is particularly important if there is a lot of fine structure to investigate as detectors usually cut off high frequencies, ultimately causing a loss in resolution. Finally it is also important to know if biasing can be applied and in what direction. Most modern detectors allow for some bias voltage to be applied across it, either retarding or accelerating electrons towards it. If a retarding bias is applied this usually favours the collection of the high energy, approximately 0.8 $E_B$, BSEs, where as an accelerating bias would favour the lower energy, $\leq$50 eV SEs.

### Lower Electron Detector

The Everhart-Thornley detector, named after its developers [31], is found in almost every modern SEM. It is known as the lower electron detector (LED) in the JEOL JSM-7800F *Prime* manual. The LED typically boasts a large solid angle alongside very efficient detection for both BSEs and SEs. It is also robust, has low noise and is cheap to maintain.

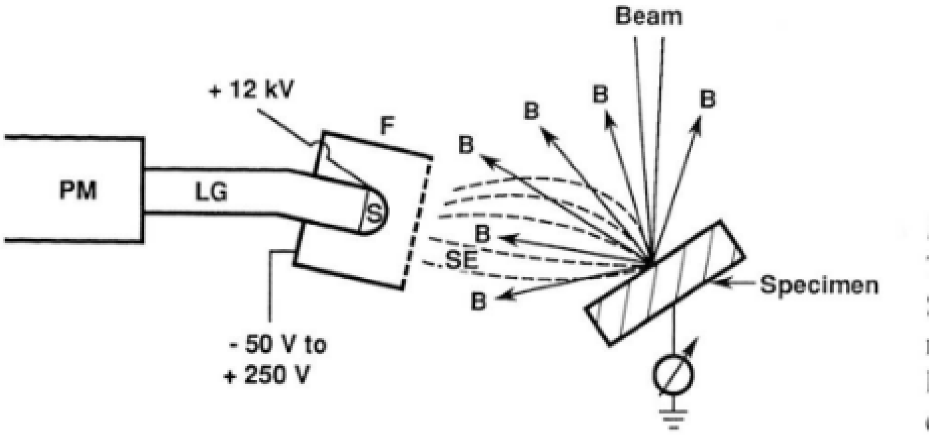

Figure 2.10: The Everhart-Thornley or lower electron detector. F represents the Faraday cage, S represents the Scintillator, LG the light guide and PM the photomultiplier, [8].

The design shown in fig. 2.10 is typical of the LED. An electron with sufficient energy, approximately 10 keV, strikes the scintillator. This releases photons which are guided to the photomultiplier through the light guide. There is usually a quartz window separating the light guide from the photocathode of the photomultiplier, which also acts as a barrier to the vacuum. Upon interacting with the photocathode, electrons are created and cascade down the photomultiplier. This provides very high gain between $10^3$ and $10^8$ and little noise whilst having a fast response time allowing an SEM to scan at a sufficiently high rate.

Electrons that do not have sufficient energy, *i.e.* <10 keV, to get a photonic response from the scintillator can not be detected. To overcome this problem a small metal grid is placed just above the scintillator that accelerates all electrons by approximately 10 kV. This ensures all electrons that strike the scintillator can produce the photons needed for detection. The grids small size and the fact that it is within the Faraday cage ensure it has a minimal effect on the distribution of electrons entering the LED. The Faraday cage shields the large bias voltage across the scintillator and can also apply its own bias voltage, both positive and negative. Applying a positive bias allows the detector to collect low energy SE more effectively, whilst the negative bias allows the detector to reject them outright.

When a negative bias is applied only direct BSEs are collected. These are the BSEs which exit the sample at the same angle as the angle of collection. Given the off-axis position of the LED and the angular dependence of BSEs described in section 3.1.1, this result in a low proportion, $< 20\%$, of BSEs being collected. It is worth noting that it is still a collection of signals solely attributed to BSEs.

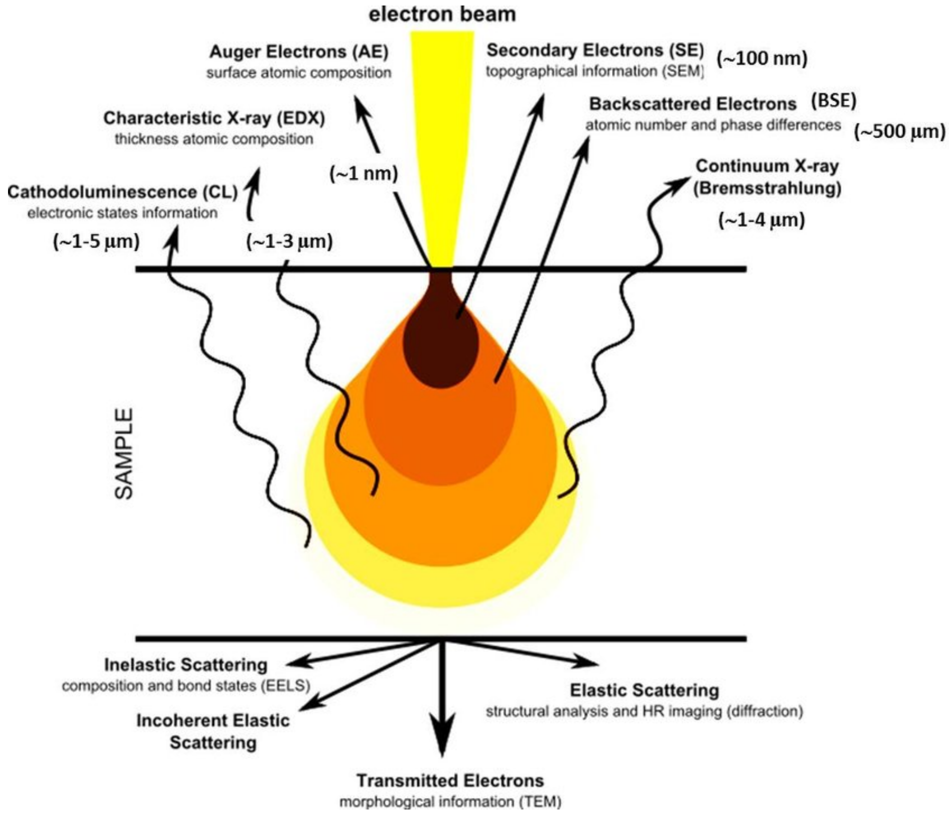

Figure 2.11: The potential detection products and the pathways of their formation, [32].

When a positive bias is applied, both SEs and BSEs are collected from a variety of different sources. The BSE contribution is unavoidable, but small, as anything that could retard these high energy electrons would also have a strong effect on the yield of low energy electrons. The BSEs collected are from both direct and indirect sources as shown in the schematic fig. 2.11. The bulk of the signal detected for the positive biased LED are low energy electrons. These would usually all be considered SEs but it has been shown that a significant proportion of this signal is made up of BSE produced SE, as much as 60% [33]. In the schematic fig. 2.12 these are marked as $SE_3$ and represent SEs that are produced by a BSEs interaction with the chambers wall. In this schematic $SE_1$ and $SE_2$ represent the SEs produced within the sample, both by the direct beam and the exiting BSEs respectively. The measurement of this has led to the understanding that whilst the LED in this configuration does collect primarily low energy SEs, many are proportional to the BSE production allowing contrast to be seen.

### Upper Electron Detector

The upper electron detector (UED) or 'through-the-lens' detector is a detector made possible by the strong field of a snorkel objective lens. This field, that extends to the sample surface, traps and guides electrons, particularly $SE_1$ and $SE_2$ electrons, back through the lens to a slightly off-axis detector. This mechanism excludes $SE_3$ electrons entirely. As for BSEs, off-axis electrons are usually too energetic to be trapped, but given the emission distribution this does not reduce the signal significantly as on-axis BSEs still be collected when there is an applied field,. This field will divert the electrons sufficiently, so that they strike the scintillator.

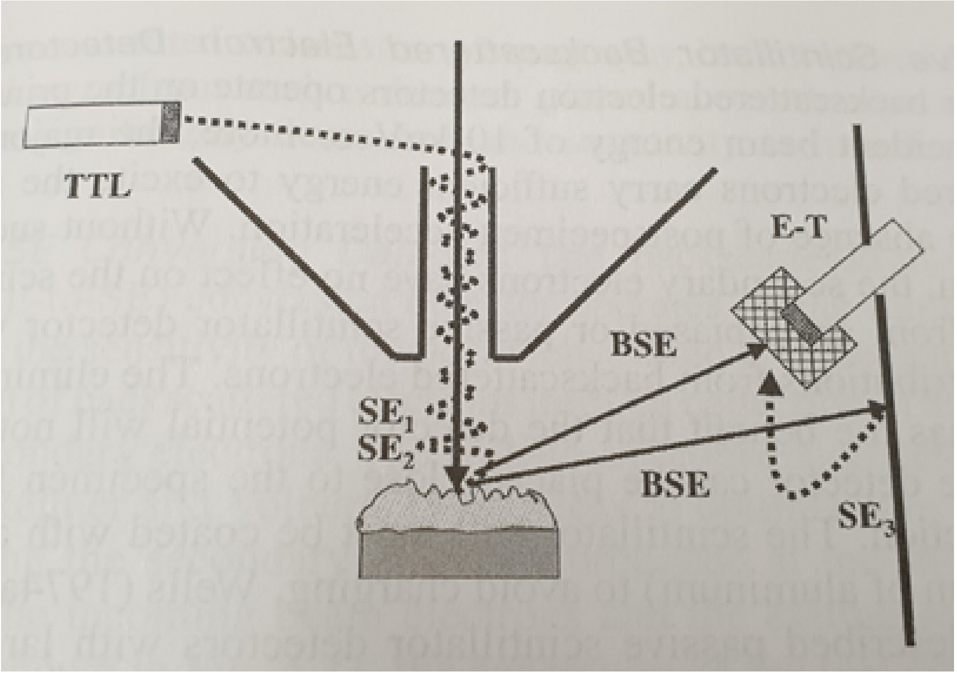

Figure 2.12: An upper electron or 'through-the-lens' detector. Here the detector is marked by TTL.

Apart from the reliance on the inclusion of a snorkel lens to gather electrons the UED, shown in fig. 2.12, works in an almost identical manner to the LED. It relies on a scintillator to convert the electrons to photons, a light guide to lead them to a photocathode and out of the vacuum, and finally a photomultiplier for gain. The UED can also apply both positive and negative bias. The positive bias acts to increase collection efficiency whilst the negative bias acts to reject the low energy SEs. Once again the scintillator is just behind a metal grid with a large bias, approximately 10 keV, to ensure all electrons are energetic enough to create photons.

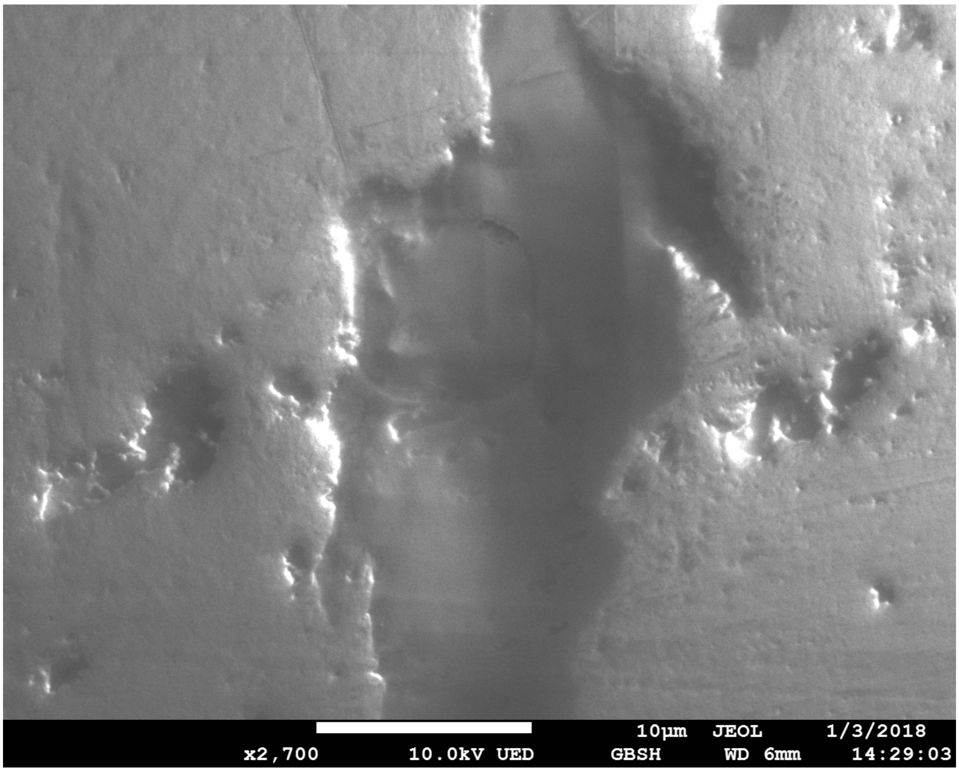

Figure 2.13: An SEM image taken using the JEOL JSM-7800F *Prime*. This is an image of an MTJ device with a 280 nm thick Au capping layer. The sample is described later in section 5.3 This was taken after attempting the removal of said capping layer.

Irrespective of the type of detector, image contrast and the corresponding information is displayed by the relative electron intensity at each pixel or position on the sample. This is then displayed as an image with a relative intensity scale such as that shown in fig. 2.13. A change in electron intensity can be caused by many things, all of which are detailed in section 3.1, but the image produced and knowledge of the sample under investigation can yield a significant amount of information from a seemingly simple contrast mechanism.

Whilst the detectors discussed generate contrast and images in the same way, an important distinction is their apparent point of illumination. Using the analogy of light microscopy an image should have an observation point and an illumination point. The observation is the apparent position of an observer, such as the eye, and the illumination point is the apparent position from which the light source originates. Interestingly within an SEM the observation point is always in line with the incident electron beam, the observer is looking down on the sample. Typically the detector appears to be the point of illumination.

The LED, with its off-axis configuration, appears to be illuminating the sample at an angle. This creates an oriented shadowing effect, based on the varying BSE distributions across an uneven surface. This effect acts to highlight topological contrast, but must also be considered when considering the contrast differences in any electron micrographs produced. The position of the LED also eliminates any information from deep wells or holes within the sample.

Unlike the LED, the UED detects electrons along the beam path, creating the illusion that the observer and illumination are at the same point. This affects the appearance of the topological contrast as there is no prefered direction, but contrast can still be seen. This unique view allows an image to be formed within holes in a sample as the electrons released from it can be captured by the magnetic field and detected. This is an extremely useful feature when imaging devices as it allows the regions between them to be investigated and stops shadows from neighbouring devices obscuring the details.

### 2.1.4 Specimen holders and preparation

The only limit on the size of a sample that can go in an SEM is the chamber itself. However, there are limits for observational area. The stage motors are the cause of this, typically only having a movement range of approximately 10 mm in the x and y direction. This allows a wide range of samples to be investigated from production wafers to single devices.

When investigating solid samples it is important that they are clean. Whilst the surface doesn't have to be polished or smooth to provide good results, the cleanliness can affect the contrast of images significantly, particularly at low beam energies (<5 keV). This is because significant amounts of carbonaceous substances can be easily deposited and 'cracked' onto the surface, layers as much as 5 nm thick [34]. This is an indeterminable layer that will adversely affect any measurements taken.

It is also important to ensure the sample is conductive. If it is non-conductive or poorly conductive, negative or positive charge will build up on the surface under the bombardment of electrons. This distorts images significantly and non-uniformly. A user is able to reduce charging within a sample by lowering the beam current or tilting the specimen. If neither of these options are suitable, samples can also be coated in conductive polymers. These act to dissipate the charge across the surface.

To mount the samples most SEMs require a user to fix the sample to a metal cylinder or stub. This is then placed within the sample holder. The method of fixation can be varied, but a few methods stand out. Use of an adhesive carbon tape, or some similarly conductive tape, to mount the sample is common. This is quick and easy and provides sufficient conduction to allow charge dissipation through the substrate. Using carbon tape may introduce another source of carbon, as it can react strongly with the beam and also carry contaminants easily, so it may affect the levels of carbonaceous material built up. If this is a concern, or a more conductive bond is required, silver dagging paint is another common bonding agent. This is applied to the stub, usually with a brush, and the sample is pressed onto it. Once dried this provides a highly conductive bond and has the benefit of introducing very little carbonaceous compounds.

In general the only differences between sample holders is the size of stub they can hold as the stage is responsible for all movement, such as rotation and tilt. However some sample holders allow a bias to be applied at the surface of the sample. This bias acts to both decelerate the incident beam and accelerate the escaped electrons. Originally this was designed to allow high resolution images to be formed at low beam energies. The probe diameter increases as the electron beam propagates through the column and lenses, due to the aberrations. Decelerating the beam between the objective lens and the sample to the required impact voltage, where the impact voltage is the beam voltage plus the negative bias voltage, should provide a much smaller probe diameter at low voltages (<2 kV).

A further use of an applied bias voltage is the ability to control the impact voltage whilst maintaining the same beam voltage and therefore the same electron optics. When this ability is combined with a knowledge of electron-solid interactions discussed in section 3.1, the basics of a comparative technique presented by Hirohata [6] can be pieced together. This work and functionality is the basis for the technique developed during this work.

## 2.2 Transmission Electron Microscopy

The TEM is a powerful tool capable of investigating interfaces with atomic resolution. Primarily the TEM utilises transmission electrons (TEs) instead of BSEs or SEs, as described in section 3.1.3. The only fundamental differences between the control of an electron beam in an SEM and a TEM are the different beam energies they have, where the TEM is at least at >100 keV. However, how this beam is utilised is different. In an SEM the beam is rastered across the sample and the products are detected. In a TEM the beam is focussed on a single point, and the TE are then focussed onto the detector after the sample. During this project the TEM used was the JEOL JEM-2010.

### 2.2.1 Comparison to an SEM

At >100 keV an electron is travelling at over half the speed of light. This means that relativistic effects come into play requiring an adjustment of the wavelength eq. (2.2). The corrected wavelength is given by [9]:

$$\lambda = \frac{h}{\left[2m_0eV\left(1+\frac{eV}{2m_0c^2}\right)\right]^{\frac{1}{2}}} \tag{2.14}$$

This shows that as $V$ increases the relativistic effects do as well. This equation is not a special case for relativistic speeds in fact at non-relativistic speeds the equation is identical to eq. (2.2).

As TEs have travelled through the sample and given the information about propagation discussed in chapter 3, samples must be thin enough to allow this to happen. When electrons travel through a sufficiently thin sample ($<$ 100 nm) it is analogous to a light wave travelling through a diffraction grating. This means the imaging resolution is not based on the probe diameter but the final product of this diffraction. This is known as the Airy disk. The radius of

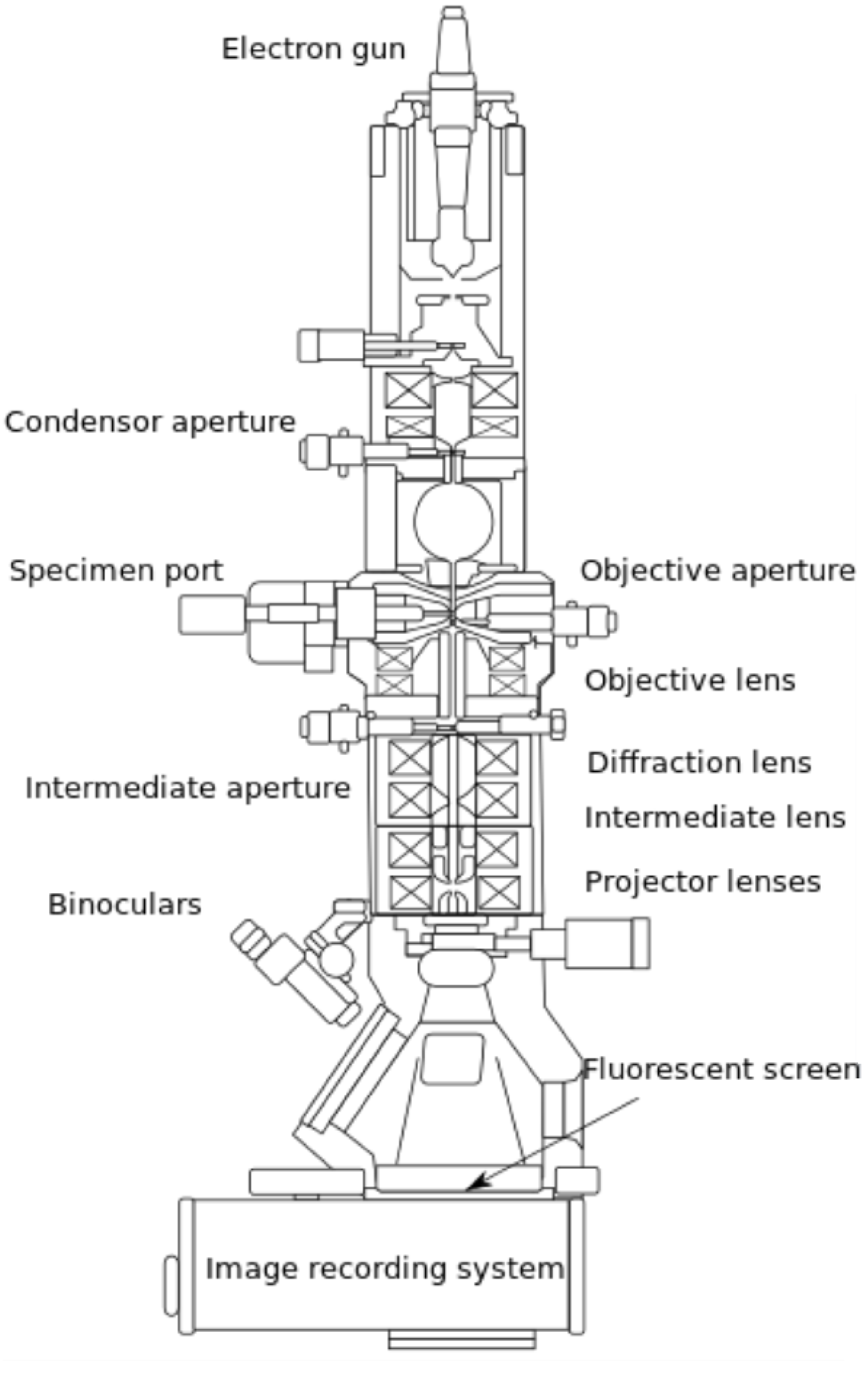

Figure 2.14: A typical transmission electron microscope.

that disk, $r_{\text{th}}$, is given by:

$$r_{\text{th}} = 0.61\frac{\lambda}{\beta} \tag{2.15}$$

This is typically used as the theoretical resolution of the system. As previously done with the SEM the theoretical resolution can be added in quadrature to the other aberration factors.

Typically TEM operators only factor in spherical aberration to estimate the spot size or resolution. The minimum radius, $r_{\mathrm{min}}$, is given by:

$$r_{\mathrm{min}} = 0.91\big(C_{\mathrm{s}}\lambda^3\big)^{\frac{1}{4}} \tag{2.16}$$

This equation gives the most practical estimate of the resolution of the TEM and is typically <0.3 nm at 100 keV. This is typically used as the energy spread is usually ±0.01% of the beam energy making chromatic aberration negligible. Operators also neglect to include astigmatism in their calculations as the use of stigmators both above and below the sample allow for sufficient correction.

Both TEMs and SEMs use similar apertures and lenses to focus a probe onto the sample. Where an SEM will raster this probe across the sample, the TEM relies on detectors beneath the sample to measure the diffraction patterns produced by the TEs and their passage through the sample. After the sample an electron lens is used to focus the patterns onto the detector surface to assist this. In combination with the very high beam energy the TEM setup shown in fig. 2.14 can produce a near-atomic resolution of interfaces an example of which is shown in fig. 2.15 if they have undergone the appropriate sample preparation.

## 2.2.2 Sample Preparation

There are two common methods to produce cross-sectional TEM samples. These are mechanical polishing and ion milling. Whilst both seem very different they both have the same target, an electron transparent sample which is <80 nm thick. Both methods have been used in this project, allowing a comparison to be made between cross-sectional TEM and SEM.

### Mechanical Polishing

Mechanical or hand polishing is the act of grinding a sample down until it is sufficiently thin to be electron transparent. In brief, a wafer is cut into two strips which are approximately 4 mm long and of equal width, the thinner the better. These are bonded together with their films touching. Support struts of silicon can also be bonded to the substrates. These are typically much wider than the sample and are present to ensure an even polish is achieved. This protects the sample and also means there is twice as much interface to

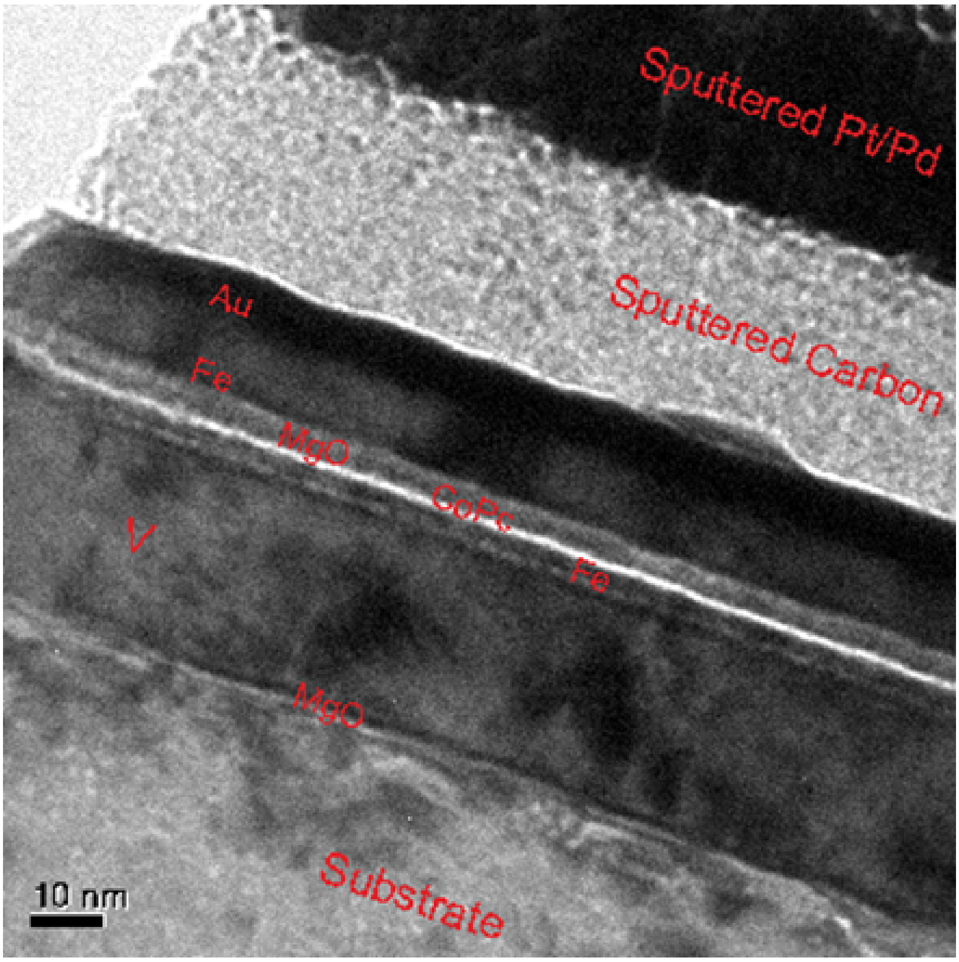

Figure 2.15: A cross-sectional TEM image of an organic tunnel barrier. This sample is discussed later in chapter 6.

look at per sample. The sample is polished on its backside using a series of diamond lapping pads with decreasing particle sizes ranging from 30 $\mu$m to 100 nm. This is then mounted to the chosen TEM grid. The unpolished side can then be thinned and polished in a similar, but more aggressive fashion, down to approximately 100 nm. The final step is to use a precision ion polishing system (PIPS) to bombard the sample with argon ions at a small angle, approximately 2°, from the surface. These ions are accelerated by a voltage of 1 kV. This should produce a sample that is electron transparent in the region of interest, the interface.

### Ion Milling

Ion milling relies on a technique known as focussed ion beam, FIB, to produce an electron transparent sample. FIB uses a focussed beam of gallium ions, at sufficiently high beam current of around 1 $\mu$A, to mill the sample. As this is easily controllable on very small scales this technique is typically used to create 3D patterns. A full explanation of cross-sectional TEM preparation can be found in Giannuzzi and Stevie [35], but a brief description will follow. Using FIB to create cross-sectional TEM samples happens in two steps.

The first step is sample lift out. This is the process of cutting an approximately 50 $\mu$m by 100 nm strip out of the wafer or device. This is done by creating a well around the desired part of the sample and undercutting it by adjusting the incident beam angle. During this process exposure to the ion beam would destroy the stack, so a large sacrificial deposit of platinum is usually placed over the area of interest. Once the sample has been cut cleanly it can be bonded to a transfer arm, removed and mounted on an appropriate grid.

The second step is sample thinning. This is the process of thinning the sample to a thickness that makes it electron transparent. This is typically done by milling the edges of the lifted out sample at a small angle, $\pm 2°$. This is done in steps, removing a decreasing amount as the sample gets thinner to reduce the chance of over-milling. A recommended practice is to also reduce the length of the sample milled at each step. This ensures that if over-milling does occur sufficient sample is still present to continue preparation. PIPS can also be used to thin the sample further if required, but this is not usually necessary.

Both methods are effective although they do each have some limitations. Mechanical polishing is a simple and widely applicable technique, but it has little selectivity. This means there is not much control of the exact region which will be electron transparent. This is not a problem for uniform wafers, but makes it unsuitable for device investigations. Mechanical polishing also requires repeated chemical cleaning during the process, making it poorly suited for the preparation of unstable or highly reactive samples, such as organic based films. On the other hand ion milling provides very strong selectivity and doesn't require rigorous cleaning as all preparation is done in vacuum. This makes it a very useful technique for exotic films or most devices. There is significant evidence that FIB preparation both damages and produces artefacts within the samples produced due to the gallium beam milling [36].

## 2.3 Energy Dispersive X-ray Spectroscopy

EDX is a technique which detects and analyses the energy spectrum of X-rays produced during beam interactions, described later in section 3.1.3. In brief X-rays can be produced via two methods the de-excitation of an ionised atom or during the deceleration of a beam electron. These are known as characteristic and Bremsstrahlung X-rays respectively.

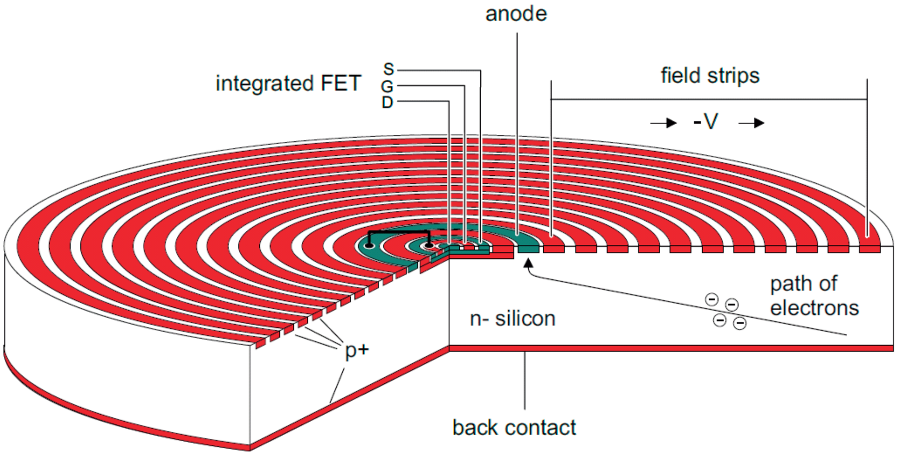

Figure 2.16: A typical silicon drift detector design, [37].

As characteristic X-rays are element specific, an EDX uses the energy of peaks in a spectrum, like the one shown in fig. 2.17, to identify the elements that are present. X-rays are collected utilising the band gap within a Peltier cooled high purity silicon drift detector [38]. When an incident X-ray passes through a very thin organic window and interacts with the detector a series of electron-hole pairs are formed. These are then directed by an applied field towards an integrated field effect transistor, which converts this collection of charges into a single voltage. The voltage is then amplified and processed by the computer system. A typical design is shown in fig. 2.16. This setup can detect >750,000 counts per second.

Each recorded voltage is proportional to the energy of the incident X-ray and each voltage is the converted collection of charges produced by the photon. The maximum number of charges, $n$, a photon will produce is given by:

$$n = \frac{E}{\epsilon} \tag{2.17}$$

where $E$ is the energy of the photon and $\epsilon$ is the peak absorption which is 3.86 eV for silicon. This results in a very low value of charge of the order of $10^{-16}$ C. As this is so small the noise of the system, particularly the converter, has a significant impact. The amplification and pulse-shaping system has been designed to reduce the influence of this noise, increasing the energy resolution. It is worth noting that the system converts charge directly into a digital signal.

EDX detectors are highly sensitive to all elements that produce X-rays in the region of 0.2-12 keV. The reason it is not sensitive to lower energies is the beryllium or polymer window. This window readily interacts with these very low energy X-rays, greatly reducing their detection rate. Whilst X-rays would typically have a very tight energy spread, approximately 2 eV, the resolution of an EDX is approximately 130 eV. This broadens peaks beyond their natural width. A further issue facing EDX measurements is the surface quality. If the surface is not smooth then the direction of scattering for X-rays will be unknown and, if the surface is rough enough, unpredictable. This can have detrimental effects on the analysis of gathered spectra.

### 2.3.1 Line Spectra

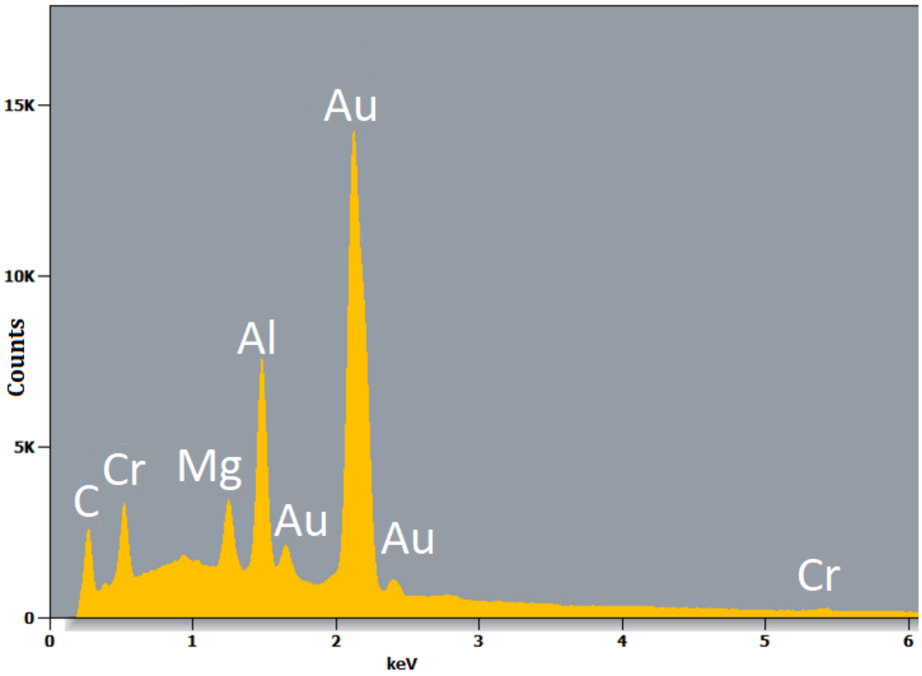

Figure 2.17: An example EDX spectrum.

Once processed, the data are typically displayed as a line spectrum such as that shown in fig. 2.17. These spectra display the total number of counts at each energy. Spectra like the one shown in fig. 2.17 can be used to find both qualitative and quantitative information. The qualitative information found from each spectrum is the elements detected [39]. It identifies the characteristic

X-rays responsible for each peak by first fitting it to find the peak position, then cross-referencing that with tables of the possible X-ray energies. This is a simple method for the identification of the elements within spectra. It is also possible to quickly classify the abundance of these elements based on their approximate count.

A lot of quantitative information can also be gathered from EDX spectra. Summing the total number of counts attributed to each element can provide significant information. Due to the continuous nature of the Bremsstrahlung X-rays and the broadening of peaks, multiple peak fittings and background subtractions are used to measure the total number of counts attributed to each element. Based on an understanding of the production of X-rays, discussed in section 3.1.3, within a sample and the counts measured, estimates can be made of the concentration of elements.

Conventional quantitative analysis has been guided by both the simulation of electron beam interactions and experimental analysis to a lesser extent. In general, analysis software requires knowledge of the beam energy, the beam current, the area of investigation and the detectors size and position. The software can then define an area of interaction, which is used to model the distribution of elements. Based on the total number of counts associated with each peak, and the ratios between peaks created by a single element, the percentage of this area is defined. Some correction factors are used, namely the ZAF factors [40]. This stands for atomic number Z, the absorption correction $\mathrm{A_C}$ and the fluorescence correction $\mathrm{F_C}$. These factors indicate the depth of generation, the absorption of X-rays during propagation and the fluorescence this may cause respectively. With these factors a number of quantities can be estimated such as atomic percentage and weight percentage.

These estimates are typically based on the assumption that the material is entirely homogeneous. Whilst this is not usually the case the results are still indicative of the chemical structure. If more detail is required from a multi-layer structure, such as a thin film on a substrate, there are simple strategies involving the comparison of spectra taken at multiple energies such as 5 and 10 keV [41]. This is particularly effective with prior knowledge of the sample and can be used to not only find the composition but also the thickness of the layers. The more complex the stack the more spectra required. Another option is to compare the measured spectra to Monte Carlo simulations, although this may be more taxing if specialist software is not utilised.

### 2.3.2 2D Mapping

Recording line spectra, which is essentially all of the counts from a given field of view, is a relatively simple affair. Due to the nature of the movement of the electron beam within an SEM it is possible to record spectra at each point of incidence. If a full compositional analysis is performed on each of the collected spectra then the results are stratified by element whilst retaining the positional information so that a map can be formed [42]. This information can be plotted as a series of dots at their respective locations where the dots are scaled in intensity based on the number of counts. As the data can be gathered then compared the scale can be determined.

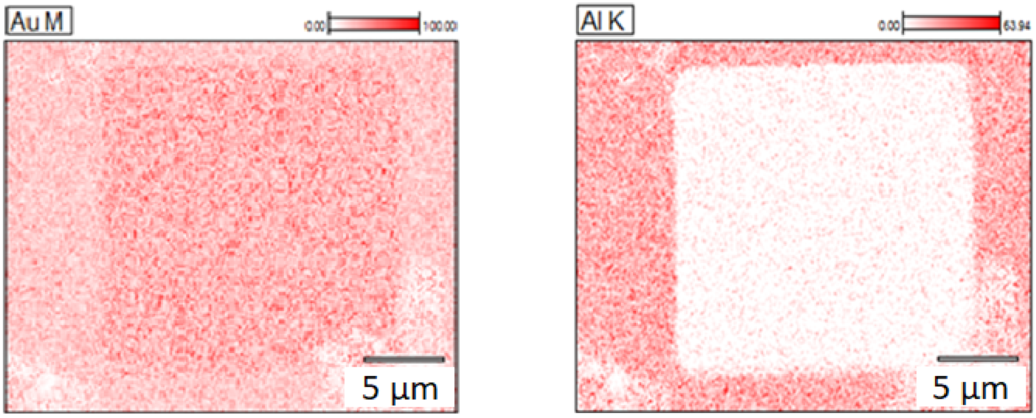

a b

Figure 2.18: Elemental maps taken using EDX mapping at 10 kV. This is a map for a. Au and b. Al. These samples are discussed in section 5.1.

Once all elements have been identified and scaled a series of maps can be produced, like those in fig. 2.18. These can be overlayed or analysed separately. Whilst this analysis is quantitative in nature, due to the speed each spectrum is taken at this type of mapping is much more suited to qualitative comparisons. One of the clear benefits of EDX mapping is the ability to readily resolve elements with similar Z which is usually difficult to do with BSEs.

Whilst mapping does take significantly longer than a line spectrum a clear benefit of mapping is the ability to study patterned films and other 2D and 3D structures, such as in fig. 2.18. Interestingly mapping skirts some of the problems faced by simple spectra. For instance, whilst it does presume the sample is homogeneous, mapping is a comparative process so the relative counts should be similar. When it is geometrically different this does not hold true as the changing geometry can affect the actual counts significantly, without being factored in for the expected counts. Due to the positional dependence of the information gathered, it is important that if any image drift occurs it is accounted for. To do this tracking software has been developed which, whilst reducing the resolution of the image, ensures that drift is tracked in real time.

Another issue that may be faced whilst using the mapping feature of an EDX is the auto-scaling. This feature can obscure areas with very low counts or even exclude them, particularly if there are areas with very high counts. The only way to circumvent this is to manually analyse the data, which is incredibly time consuming depending on the resolution of the stored data. A further limitation of mapping is the spatial resolution of the EDX. This resolution not only varies by detector, but it is also dependent on Z. At high Z it is approximately 1 $\mu$m$^2$ and at low Z it can be approximately 5 $\mu$m$^2$. This greatly limits the possible magnification, especially when compared with the SEM's capabilities.

# Chapter 3

# Electron Interactions with Solids

As discussed in the previous chapter an SEM rasters a beam of electrons across the surface of a sample and the scattered electrons at each point are detected, analysed and formed into an image. As this study aims to utilise this information in an unconventional manner, it is important to have a thorough understanding of how the electron interacts with the sample and how the detected images are produced. The current physics relating to the interactions of electrons within solids will be outlined in detail, specifically that which relates to the volume of interaction and the nature of the products produced. This information will also be used to assist the explanation of the mathematics used in the simulations of the systems. Much of what follows is common theory therefore unless otherwise stated the information has been taken from the standard textbooks. The interested reader can find a more rounded discussion for SEM in Scanning Electron Microscopy and X-ray Microanalysis [8] and for TEM they can refer to Transmission Electron Microscopy [9].

Electron flight simulations have been used as they provide an opportunity to test multiple ideas or quantify configurations quickly, providing usable and physically applicable statistics. When a model that closely reflects a physical system is used simulations are also able to probe it in a way that is difficult to replicate in experimental studies. Monte Carlo methods have been chosen in this study as they allow an investigation of phenomena with statistically relevant data using powerful single particle models. In this way simulations have not only been used to provide further evidence for its viability, but also to configure and calibrate the depth information received. In this study the program of choice was the Monte Carlo simulation of electron trajectory in solids (CASINO) [43] and its operation will be discussed in section 3.2, although other programs with similar methodologies were also utilised to confirm the findings. CASINO, has been specifically designed to simulate the operation of an SEM, particularly at low beam energies (<5 keV).

## 3.1 Electron Beam Interactions

Once a parallel beam of electrons, with an energy between 0.1-500 keV has entered a sample, each electron is able to interact with both the nucleus and the electron cloud of the atoms present. These interactions can be split into two categories, elastic and inelastic. During an elastic collision no information is exchanged or energy lost, but the electrons trajectory can be changed significantly. An inelastic collision also allows for a trajectory change, although it is usually very small (<10 mrad), but the electron always loses energy during the interaction.

### 3.1.1 Electron Scattering

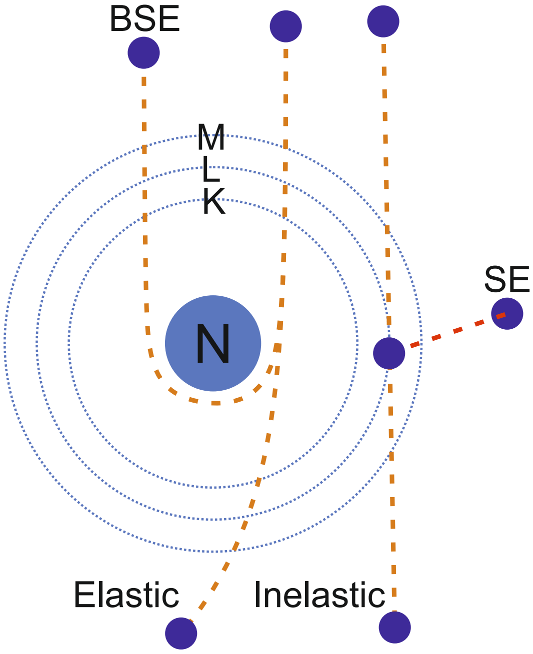

Figure 3.1: An illustration demonstrating some of the possible scattering interactions within an atom.

Elastic scattering between an electron and nucleus is entirely down to the Coulomb interaction between the negatively charged electrons and the positive nucleus, or its negative electron cloud. These interactions can occur multiple times during an electrons path through the sample, deflecting it from the path it originally held. It is also very common that after multiple scattering events the electron leaves the sample to be detected, essentially experiencing a net change in angle of approximately 180°. These electrons are known as BSEs unless they are under 50 eV and are an important source of information in an SEM. It is usually the case that the electron cloud is responsible for low-angle scattering and the interactions that are much closer to the nucleus typically result in high-angle scattering.

### Elastic Scattering

Scattering events occur probabilistically. This is due to both the distance between these events caused by the spacing of the atoms and the fact that in each event there are multiple possible interaction types. The mathematical representation of elastic scattering is the cross section, $\sigma_{el}$, measured in $\text{cm}^2$. Rutherford's expression [44] for $\sigma_{el}$ is given by:

$$\sigma_{el}(>\phi_0) = 1.62 \times 10^{-20} \frac{\mathrm{Z}^2}{\mathrm{E}_e^2} \cot^2\left(\frac{\phi_0}{2}\right) \tag{3.1}$$

This shows the number of elastic scattering events at an angle greater than $\phi_0$ per electron per atom per $\text{cm}^2$, where Z is the atomic number and $\mathrm{E}_e$ is the electron energy. From this expression it can be seen that as $\mathrm{E}_e$ decreases the probability of an elastic scattering event increases. This can be attributed to both the reduction of momentum of an electron, meaning smaller forces can affect change and the decreased likelihood of an inelastic reaction. The cross section also increases just as quickly with increasing Z. In this case the increase in protons within the nucleus leads to a larger electrostatic force.

Rutherford's initial expression, eq. (3.1), was based on his famous alpha particle experiment and as such this form only considers the individual atom with which the electron is interacting. It does not include the surrounding electron clouds. Those clouds of negative charge act as a screen, effectively reducing $\sigma_{el}$. To account for this a screening parameter [45], $\alpha$ can be used:

$$\alpha = 3.4 \times 10^{-3} \frac{\mathrm{Z}^{\frac{2}{3}}}{\mathrm{E}_e} \tag{3.2}$$

This equation describes the threshold angle at which the nucleus dominates the Coulomb interactions that make up the elastic scattering events, therefore allowing the electron-electron interactions to be ignored. In TEM applications particularly when the electron energy is greater than 100 keV, these screening effects can be ignored. In an SEM this is not the case.

Thankfully this screening parameter can be included in the differential form of Rutherford's equation and calculated to form the screened Rutherford cross section [46], also measured in cm$^2$:

$$\sigma_{el} = 5.21 \times 10^{-21} \frac{\mathrm{Z}^2}{\mathrm{E}_e^2} \frac{4\pi}{\alpha(1+\alpha)} \left[ \frac{\mathrm{E}_e + 511}{\mathrm{E}_e + 1022} \right]^2 \tag{3.3}$$

This equation is a widely applicable model although it does have its limitations. For TEM calculations the model struggles when the beam energy >300 keV or when Z >30. This is in part due to the large scattering angles. Similarly Rutherford's equation proves to be invalid for some SEM regimes. In the Rutherford equation scattering is based on the first Born approximation. The driving field in each scattering event is presumed to be the incident field not the total field. This does not hold true for interactions where the energy is <10 keV resulting in an over-prediction of the cross section.

The initial inaccuracies of eq. (3.3) are largely due to the fact that the equations are based on Rutherford's alpha particle experiments. Mott worked to redevelop the proposed model for use with electrons [47]. In either of the cases above the Mott cross section formula can provide a significantly more accurate model, but comes with its own downsides. Firstly the Mott theory has no analytical solution, so several empirical formula have been developed. These formula are all invariably corrections to the Rutherford theory and as such do not reveal any new physics. However they provide an elastic scattering cross section closer to experimental data. The specific formula used in our model will be covered in the simulation section.

An approximation of the frequency of events occurring is needed to predict how an electron travels through a solid. This frequency is characterised by the mean free path and is denoted $\lambda_{el}$, measured in cm. This represents the average distance an electron travels between elastic scattering events and is given by:

$$\lambda_{el} = \frac{\mathrm{A}}{\sigma_{el} N_0 \rho} \tag{3.4}$$

where A is the atomic weight, $N_0$ is Avogadro's number and $\rho$ is the volumetric density, A/cm$^3$. The mean free path for a 100 keV electron travelling in carbon would then be approximately 200 nm. This example makes it clear that during

TEM usage only a single interaction is expected as the sample thickness is $\lesssim$100 nm. In an SEM multiple elastic scattering events are expected as the sample is significantly thicker.

### Inelastic Scattering

Inelastic scattering where the electron loses energy, has numerous mechanisms including ionisation, excitation and plasmon generation. These interactions all result in a reduction in the electron energy and the production of a by-product, such as an X-ray. Once again these interactions can be described with a cross section, but Bethe [48] proposed an alternative approximation. The average energy loss through all inelastic interactions, $dE$, with distance travelled, $ds$, is given by:

$$\frac{dE}{ds} = -2\pi e^4 N_0 \frac{\mathrm{Z}\rho}{\mathrm{AE}_e} \ln\left(\frac{1.166\mathrm{E}_e}{\mathrm{J}}\right) \tag{3.5}$$

measured in keV/cm, where $e$ is the charge of an electron and J is the average energy loss per event $[(9.76Z + 58.5Z^{-0.19}) \times 10^{-3}]$ [49]. It has become standard to use this approximation instead of considering all the different scattering cross sections. This shift is largely due to the fact that the differential form of the Bethe stopping power equation demonstrates that the trajectory of electrons that interact inelastically typically change by <10 mrads. This means that elastic events dominate all major shifts in electron trajectory. For a certain material and a defined terminating energy for an electron eq. (3.5) can also be used to estimate the so called Bethe range, the maximum distance an electron can travel within a solid. This terminating energy is typically chosen to be equivalent to that of conduction electrons. Beam electrons that reach this energy can be referred to as spent electrons.

The Bethe equation provides accurate information but falls short when trying to describe the inelastic interactions of electrons where $\mathrm{E}_e$ <10 keV. This is because certain inelastic scattering events are no longer possible once an electron energy is below a certain threshold. Joy and Luo [50] proposed a semi-empirical model based on eq. (3.5) to account for this change in J, given by:

$$\frac{dE}{ds} = -7.85 \times 10^4 \frac{\mathrm{Z}\rho}{\mathrm{AE}_e} \ln\left(\frac{1.166(\mathrm{E}_e + \mathrm{kJ})}{\mathrm{J}}\right) \tag{3.6}$$

once again measured in keV/cm. In this expression k is an element specific variable that is fitted empirically with the form $\mathrm{k} = 0.7 + 0.07 \log_{10} \mathrm{Z}$, i.e.

is dependent on atomic number, and all other symbols are consistent with eq. (3.5). In this expression all of the natural constants have been evaluated into a single constant. At high energies this model gives the same results as the Bethe expression as $E_e >> J$. With correctly calibrated values of k the equation fits experimental data down to approximately 0.1 keV. This is useful as beyond this point electrons are generally either not going to escape, or escape and are classified as SEs which are then used for imaging.

### 3.1.2 Interaction Volume

Given the range defined by the Bethe equation for an electron measured along its trajectory and the fact that it can scatter across any angle elastically, the path of an electron can cover a large lateral distance as well as moving perpendicular to the sample surface. In the case of TEM this lateral movement has a small effect on the resolution when compared with the microscope's spot size. This is because the electron will typically only undergo one or two elastic scattering events due to the thickness of the sample ($\lesssim$100 nm). This reduces the chances of a large lateral shift. This is not the case in an SEM. Due to both a significantly thicker sample and the lower beam energies it is expected that the electrons will go through many scattering events. This continues until the electron is ejected from the sample as a BSE or it loses its energy through inelastic collisions. This creates a large volume beneath the incident spot, sometimes over 1000 times larger than the spot, which can provide information for a detector. This is known as the interaction volume.

This interaction volume plays a large role in the actual spatial resolution of the SEM. It plays a large part in what is detected, generating the images taken with an SEM. For that reason it is important to understand how the interaction volume is influenced by the sample and the incident beam. Assuming a smooth surface the three dominant effects are the beam energy, the sample composition and the angle of incidence of the beam. The sample thickness can also play a role when it is <1 $\mu$m, but this is not common in SEM use as the sample substrate is usually much thicker. For the case of a pure sample the composition term would depend on Z. For alloys or compounds a combination of Z values would be required.

The incident beam energy has a strong effect on the interaction volume. This is shown in fig. 3.3 using CASINO to calculate the electron-solid inter-

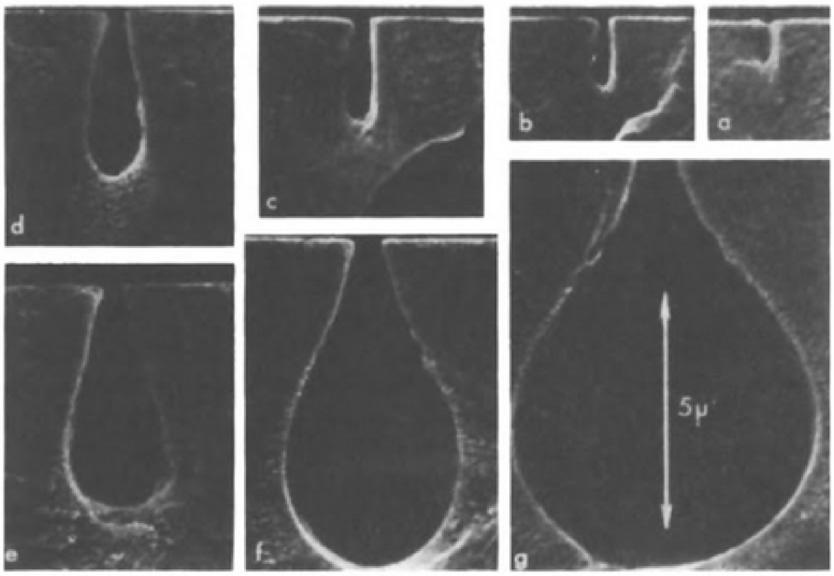

Figure 3.2: An etching experiment performed in polymethylmethacrylate to demonstrate the interaction volume of an electron beam. The electron dose has been kept the same for all the experiments, but the etching time has been increased to represent the changes in interaction volume as electrons penetrate further into a sample, [51].

actions at different incident energies. These simulations were the result of 2000 electron paths, a low number chosen to generate a clear example. Equation (3.6) can be used to find the rate at which an electron loses energy. As the rate and energy have an inverse relationship, if $E_e$ is large then the electron will travel much further before being spent. In eq. (3.1) it has already been discussed that $\sigma_{el}$ varies by $1/E_e^2$. This means that as $E_e$ increases elastic interactions are initially less likely to happen. When combined with the fact that it will also take longer for the electron to lose energy this results in a much greater penetration of the sample and more lateral movement as well.

In a similar manner eq. (3.1) can be analysed with regards to the atomic number, Z. This shows that $\sigma_{el}$ varies with $Z^2$, the opposite correlation to $E_e$. As can be seen in fig. 3.4, the interaction volume decreases as Z increases. Once again this figure was produced in CASINO using 2000 simulated electrons. This occurs because an increase in Z results in a larger Coulomb force. This leads to an increase in the number of scattering events. Not only are these scattering events more frequent, they are also more likely to create a higher angle deflection. This deviates the electrons from their original path more quickly, ejecting them from the sample as BSEs more readily.

The effects of the angle of incidence, $\theta$, are a little less obvious to deduce

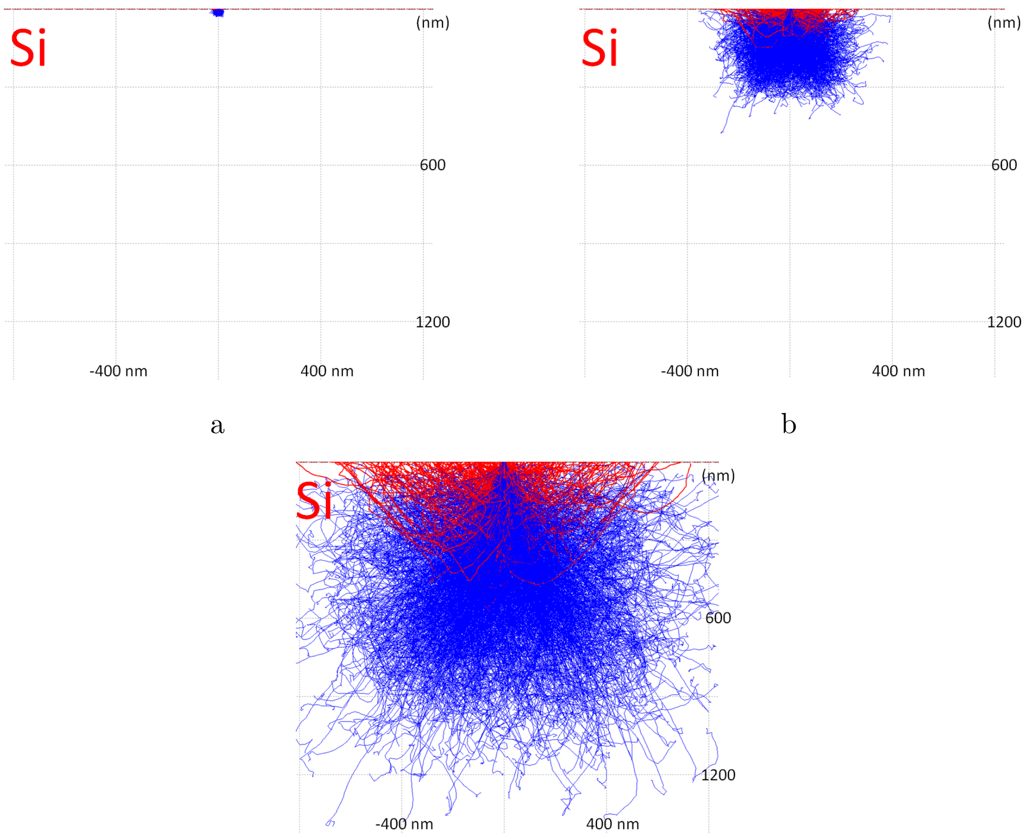

a

b

c

Figure 3.3: A demonstration of the effect of changing beam energy, $E_e$, on the maximum penetration depth of BSEs (in red) and spent electrons (in blue), simulated in CASINO. For each case keV is a. 1 keV, max depth approximately 40 nm; b. 5 keV, max depth approximately 400 nm; c. 10 keV, max depth approximately 1200 nm

from the scattering equations. As $\theta$ increases the penetration depth is reduced and the interaction volume becomes less symmetric. The electron paths of 2000 electrons have been simulated in CASINO, shown in fig. 3.5 to aid the explanation of this occurrence. The most probable change in angle after an elestic collision is approximately 4°. Given an incident beam perpendicular to the surface, shown in fig. 3.5a, electrons tend to penetrate more deeply into the sample after their initial scattering event. Probabilistically, some electrons will experience much larger angles of scattering and be ejected from the sample, but they are in the minority.

As $\theta$ increases scattering will tend to happen either laterally or penetratively, as shown in fig. 3.5b. Even at this small angle an asymmetry is created, where electrons are scattering more favourably to the right of the sample. This small angle also reduces the penetration depth by approximately 15%. It is

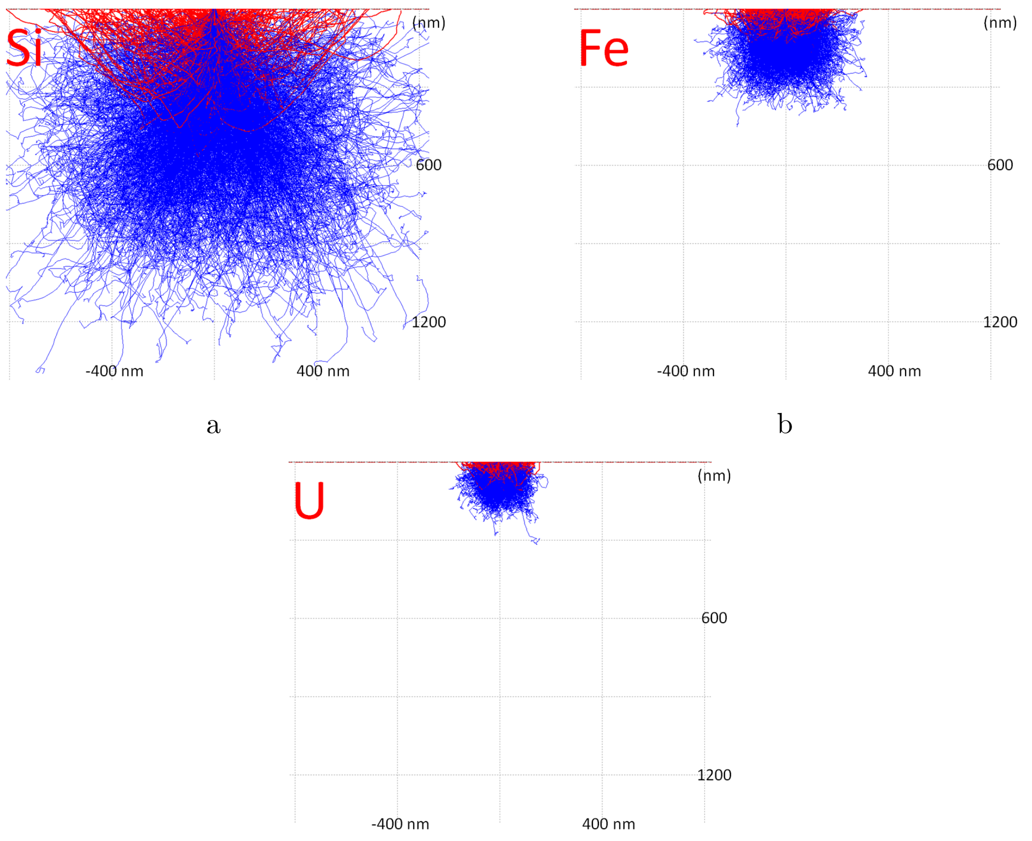

a

b

c

Figure 3.4: A demonstration of the effect of changing atomic number, Z, on the maximum penetration depth of BSEs (in red) and spent electrons (in blue), simulated in CASINO at 10 keV. For each case Z is a. 14 - Silicon, b. 26 - Iron and c. 92 - Uranium.

also worth noting that there is an increase of approximately 10% in the number of electrons escaping the surface to the right of the incident beam and a corresponding reduction to the left. This is due to the initial scattering events pushing around half of the electrons closer to the surface than in the beam normal case. Once $\theta$ is sufficiently large, such as the case in fig. 3.5c and fig. 3.5d, a significant distortion of the previously symmetric interaction volume is observed. A reduction of >50% of the penetration depth is also observed. This is due to an exaggeration of the favouring of the scattering direction as described. Kanaya and Okayama [52] proposed that the maximum penetration depth changes approximately with tilt by a factor of $\cos\theta$.

The interaction volume is the cause of the reduction in expected resolution in an SEM. It creates a subsurface region, larger than the spot size, which generates electrons that influence any imaging. However,it also gives access to significant subsurface information. When performing any study it is impor-

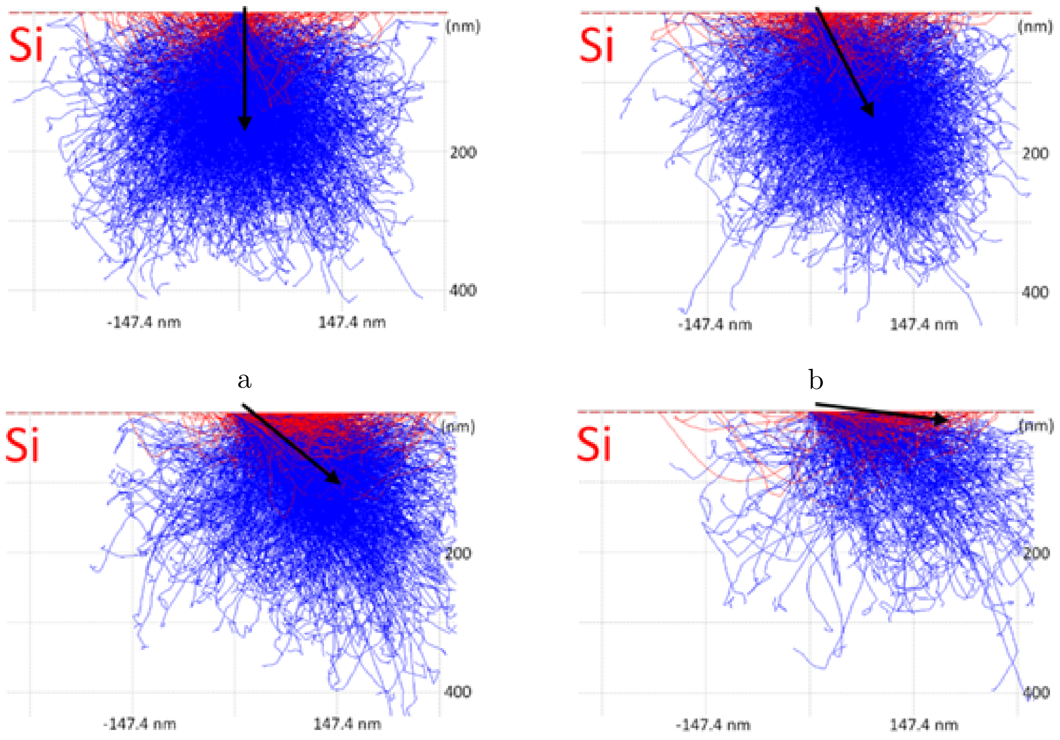

a b

c d

Figure 3.5: A demonstration of the effect of changing angle of incidence, $\theta$, on the maximum penetration depth of BSEs (in red) and spent electrons (in blue), simulated in CASINO at 5 keV. For each case $\theta$ is a. 0°, b. 30°, c. 60° and d. 89°.

tant to consider the effects of $E_e$, Z and $\theta$ as they will heavily influence the detected image. This is even more important in heterogeneous samples, such as multilayer structures, as interaction products from subsurface layers will be detected and reduce the clarity of information from the surface.

### 3.1.3 Interaction Products

Elastic scattering is responsible for the production of BSEs and TEs. These are the main detection products in SEM and TEM respectively. Inelastic scattering events, whilst reducing an electron's energy, result in many more detectable products. These products can be split into three categories; primary detection products, X-rays and other detectable products. Figure 3.6 shows the possible interaction products from these two electron microscopy techniques. This section will discuss these, focussing on their origin, their classification and the information they may provide.

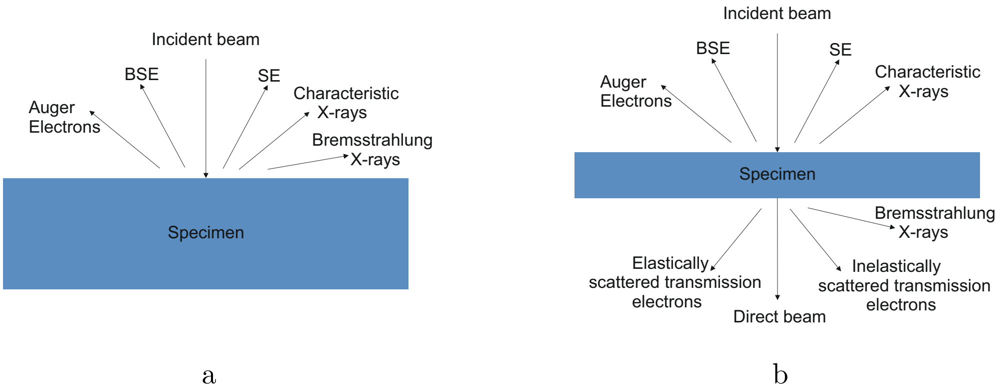

Figure 3.6: The interaction products produced by an incident beam and its interactions with a sample in a. an SEM and b. a TEM. Reproduced from [9].

### Primary Detection Products

Within an SEM the primary detection products are SEs and BSEs. BSEs are beam electrons that have experienced a change in direction of travel of approximately 180° and have retained sufficient energy to escape the sample again. It is very common for BSEs to retain a significant proportion of their original energy, represented in region I of the schematic shown in fig. 3.7. This region represents the bulk of BSEs of which typically undergo a few interactions and have not penetrated that deeply into the sample. Region II of fig. 3.7 represents the BSEs that have undergone more interactions and likely have penetrated more deeply into the sample, hence they have a broad spectrum of energies. Experimental data shows that this schematic varies very little with changing Z. As Z becomes higher the peak in region I accounts for a larger proportion of BSEs and it shifts towards the right. Regions II and III show very little change. Changing beam energy also has a slight effect on the schematic in fig. 3.7. As the incident beam energy decreases region III, representing SE yield, increases.

The final region, III, in fig. 3.7 shows the peak attributed to the SEs. SEs are products of inelastic scattering events. They are outer shell electrons which have been liberated from their atoms by ionisation. These electrons then travel throughout the sample in much the same way as a beam electron, interacting and creating more detectable products. Inevitably some of these electrons escape the surface and are detected as SEs. It is highly likely that SEs originate from near the surface due to the low energy they are imparted with during ionisation. When used to image they provide abundant information on the surface resulting in an SEMs characteristic ability to resolve surface

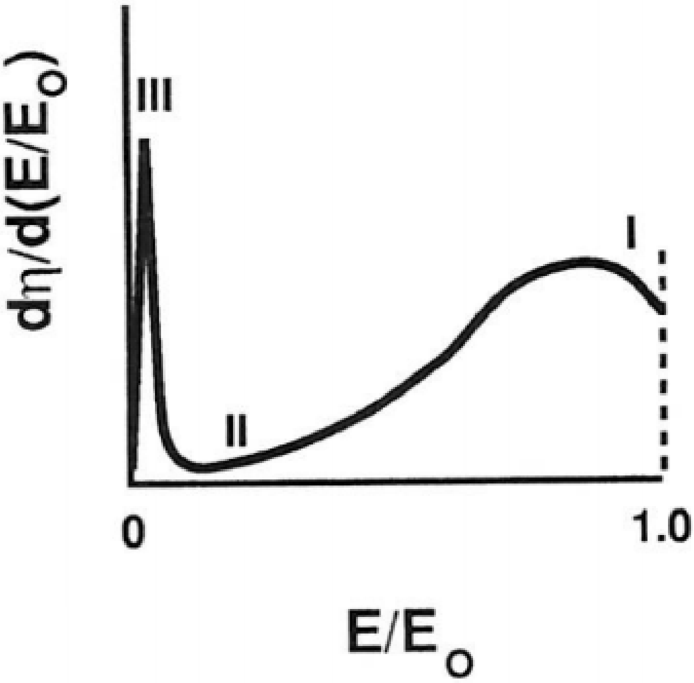

Figure 3.7: The energy distribution of electrons that have been ejected from the target, [8]. Here $E_0$ is the electron beam energy and E is the energy of the electron ejected from the target.

detail with high clarity. It is worth noting that region III is not entirely made up of just these SEs, there are also some BSEs that happen to fall below the arbitrary energy limit of 50 eV for SEs. However, these only make up a small percentage of electrons at that energy level, meaning they have little impact on any analysis done on SEs.

Before the factors affecting these primary products are discussed, it is worth investigating the depths at which the SEM products are produced. It is easy to be convinced that the total interaction volume of an incident beam within an SEM does not contribute to collected signals, but it is important to know the proportion that is. Electrons are generated via ionisation throughout the sample by the incident beam and subsequent scattering products. Due to the low kinetic energy and the constant deceleration from inelastic scattering, very few escape the sample and are detected as SEs [53]. This means that no matter the beam energy SE signals are made entirely of electrons produced in the top 50 nm of a material. This value is typical for insulators and is much smaller in conductors (5-10 nm). Due to the fact that SEs are typically more abundant than BSEs it makes sense that the SEM has developed a reputation for being a surface sensitive technique.

Despite this reputation and based on the previous discussion about the production of BSEs, it should be apparent that most are not produced at the surface. This means that they intrinsically carry some depth information. Using Monte Carlo programs like CASINO, the depth that these BSEs reach can be investigated. This study [54] has been done previously and found that when using a carbon sample 95% of all BSEs reached their maximum depth within the first third of the total interaction volume. This reduces to the first fifth in gold and other elements with large Z. From these examples it is clear that BSEs carry a significant amount of depth information.

If the factors affecting backscattering are to be discussed it needs to be first quantified. This can be done simply by using the backscattering coefficient, $\eta$, given by [8]:

$$\eta = \frac{n_{BSE}}{n_B} \tag{3.7}$$

where $n_{BSE}$ is the number of BSEs and $n_B$ represents the number of incident beam electrons. There is a similar equation for the secondary electron coefficient, $\delta$, is given by:

$$\delta = \frac{n_{SE}}{n_B} \tag{3.8}$$

where $n_{SE}$ is the total number of SEs. These coefficients provide a simple way of evaluating the expected changes in the primary detection products with different variables.

The effects of atomic number on the energy distribution of the primary products has already been discussed in section 3.1.2, but the effects on both $\eta$ and $\delta$ have not. Both simulations and careful experiment have been used in the past to establish the dependence of $\eta$ on Z. Shown in fig. 3.8a, it is seen that as Z increases $\eta$ also increases, although at a decreasing rate. This relationship is encouraging as it precludes the establishment of an element specific contrast mechanism or a Z contrast. The relationship shown in fig. 3.8a has been fitted with the expression $\eta = -0.0254 + 0.016\mathrm{Z} - 1.86 \times 10^{-4}\mathrm{Z}^2 + 8.3 \times 10^{-7}\mathrm{Z}^3$ which allows $\eta$ to be estimated during simulations and for Z contrast calculations. Whilst there may be multiple solutions to this fit, it is the generally used form. Due to the way SEs are produced it is much harder to measure experimentally $\delta$ in a repeatable manner. In fact experiments can vary by a factor of 3 for values of $\delta$ [55]. This can be accounted for by the differences that surface quality and cleanliness induce [56]. Whilst this affects simulations of these effects, there is a clear trend among the data. It is seen that $\delta$ does not generally change with Z. This means that all Z contrast observed should originate from the BSEs although that doesn't exclude the presence of Z contrast in SE images, especially when there are large differences in Z. However variations in surface quality and cleanliness can have large effects on images made up predominantly from SEs. Hence care must be taken when interpreting these images.

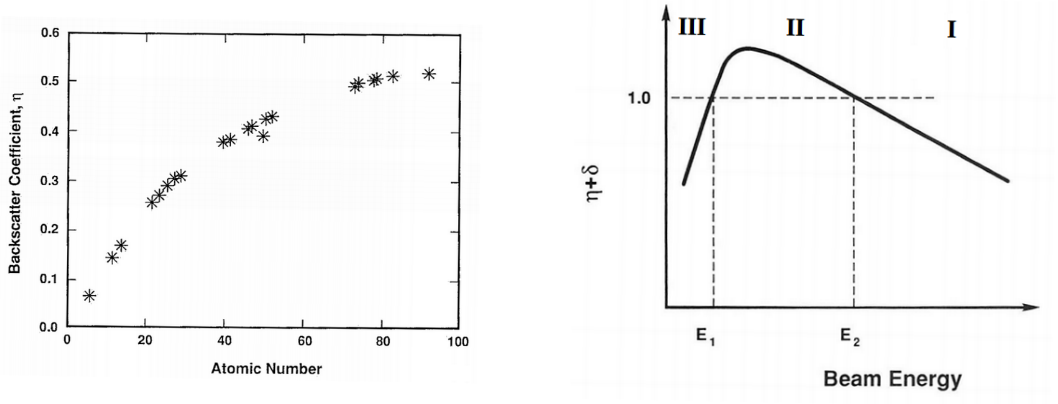

a

b

Figure 3.8: Diagrams demonstrating the effects of a. how $\eta$ and $\delta$ varies with Z, data taken from [57] and [58], and b. $\eta+\delta$ varies with $E_e$, [8].

The incident beam energy has a large effect on the interaction volume as discussed previously in section 3.1.2. When the dependence of beam energy on BSEs was investigated it was found that it had little effect on $\eta$ [57]. In fact for a large range of Z, $\eta$ was measured to be well within 10% when $E_e$ was varied between 5 and 50 keV [59]. Measurements have found that this is not the case with SEs because in general $\delta$ increases as the beam energy decreases [60]. This trend doesn't hold for very low energies, where it inverts. These two relationships result in an interesting behaviour with regards to the total electron emission, $\eta+\delta$, and changing beam energy, shown in fig. 3.8b.

If we study the schematic, shown in fig. 3.8b, in terms of decreasing incident beam energy we can see three distinct regions. Region I is dominated by $\eta$, hence the very slow increase from >20 keV to approximately 10 keV caused by a gradual change in $\delta$. At somewhere between 5 and 10 keV region II starts. Here $\delta$ increases more rapidly whilst $\eta$ remains constant. This rapid increase in $\delta$ can be accounted for when the penetration depth of the beam electrons is considered. SEs have a maximum depth of generation, so as the penetration depth approaches this maximum, a greater percentage of SEs escape the sample. This results in more SEs contributing to the total emission. It is worth noting that at some energy, which varies between 0.5 and 4 keV depending on the material, the total coefficient is greater than one. If that is the case there are more electrons escaping than are in the initial beam. Region III shows a sharp decline in the total number of electrons. This is due to the decrease of $\delta$ as the penetration depth reduces below the maximum depth of generation. This leads to a reduction in the total volume in which SEs can be generated. This leads to the total electron coefficient returning to close to $\eta$.

A worthwhile topic to look at is the effect of the angle of collection on the primary products. It is quite important to understand the effects of the collection angle of detectors used, described earlier in section 2.1.3, to interpret the images they produce. When considering the angular distribution of BSEs it is usual to define the angular coefficient of backscattering, $\eta(\phi_0)$, relative to the coefficient at the normal, $\eta_n$. Given a detector with a very narrow angle of collection placed at some angle, $\phi_0$, from the normal, $\eta(\phi_0)$ varies according to:

$$\eta(\phi_0) = \eta_n \cos\phi_0 \tag{3.9}$$

This relationship is symmetric around the normal axis. It also shows that most BSEs are reflected back along the incident beam and very few escape the surface with a large $\phi_0$. Despite the very different production mechanics of the products, $\delta$ has a very similar relationship. This is due to the limited range that secondary electrons can be produced allowing for more to be released along the normal.

Within a TEM the primary detection product is the TE, shown in fig. 3.6b. TEs are beam electrons which have fully penetrated the sample. For best imaging results users typically require TEs which have interacted elastically with only one or two atoms, meaning they have usually only deviated by a small angle (<5°). These are used to form either the diffraction pattern or direct transmission image, also discussed earlier in section 2.2, or combined to produce a phase contrast image. Any electrons that have scattered >10° are not typically used in imaging as they are incoherent. It is also expected that TEs have only undergone a handful of inelastic interactions as well. Due to this the energy of the TEs is usually >70% of the incident beam energy. SEs and similar low energy TEs are also produced but they are not considered primary products. In fact in the case of low energy TEs they are considered a hindrance as they interfere with the image forming electrons, lowering the overall resolution, or in the worst case mimicking the form of a defect.

### X-rays

There are two main types of X-rays produced in electron microscopes, characteristic and Bremsstrahlung. These two categories of X-rays are produced by very different mechanisms throughout the entirety of the interaction volume. This is largely due to the fact that once an X-ray has been produced, it interacts very little with the sample, allowing it to escape and be detected. This also means that the X-rays are generally released evenly across $4\pi$ sr, but they are produced in abundance, so detection is not an issue. No matter the means of production all X-rays share the following relationship:

$$\lambda = \frac{1.24}{\mathrm{E}} \text{ nm E in keV} \tag{3.10}$$

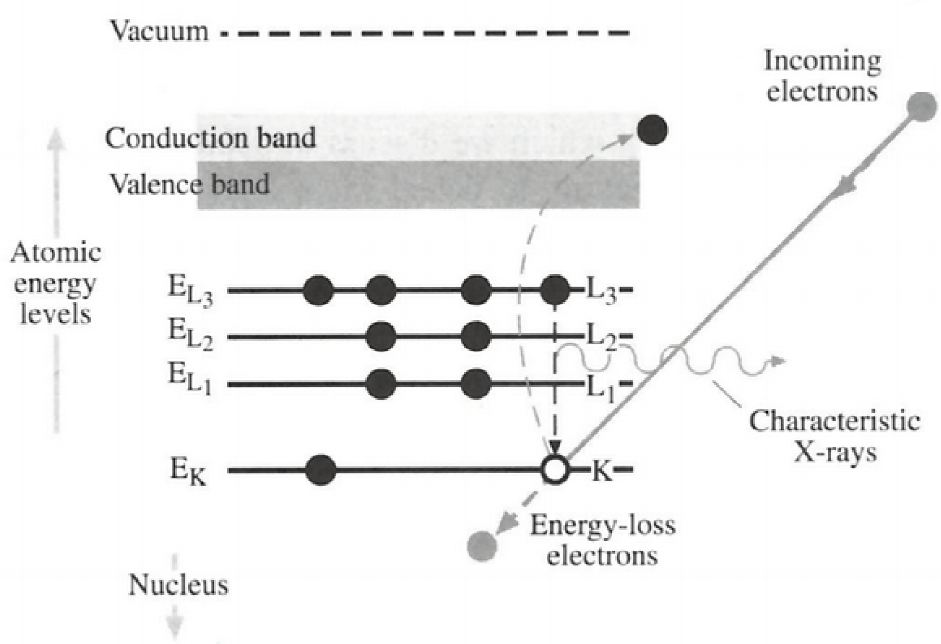

Figure 3.9: Ionisation of inner shell electrons and the production of X-rays via the de-excitation of outer electrons, [9].

Characteristic X-rays are produced during the de-excitation of an ionised atom into its ground state. This releases a photon of an energy equivalent to the transition that has taken place, with a wavelength found using eq. (3.10). Of course not every transition will produce a photon of sufficiently high energy to be an X-ray. In practice this means that all characteristic X-rays are produced when an incident electron successfully ionises an inner shell electron. These X-rays are considered characteristic as each de-excitation path has a discrete and unique energy difference, both within an atom and between elements. This allows peaks in the X-ray energy spectrum to be labelled with the element responsible for its production.

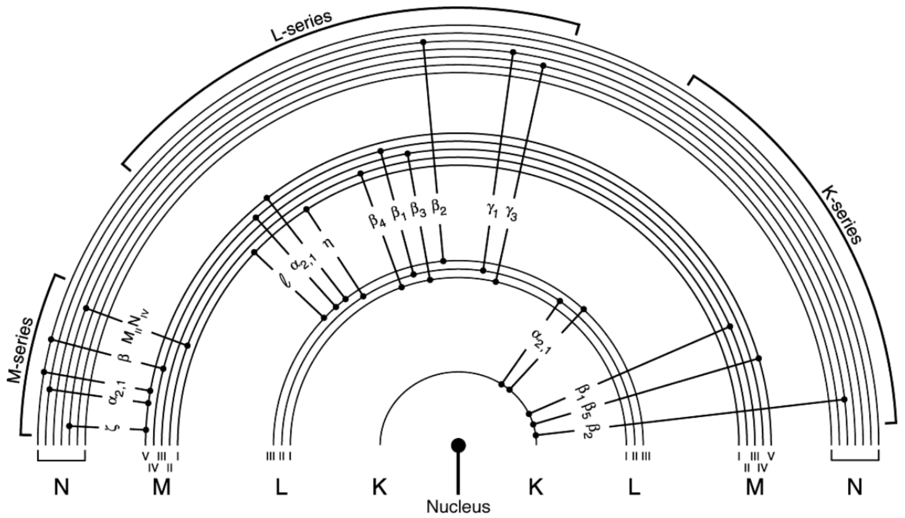

Figure 3.10: The allowed electron transitions responsible for the *M*, *L* and *K* series of X-rays. This has been adapted from Woldseth [61].

The simplified diagram, fig. 3.9, does well to represent the formation of a characteristic X-ray. Atoms have a large number of possible energy levels shown in fig. 3.10, even within the normal operating range of an SEM. This diagram can be used alongside tables of atomic energy levels [62] to identify the expected energy of a characteristic X-ray. The rules for allowed transitions between electron shells have been considered within this diagram. Whilst there are a lot of possible energy levels for atoms it is expected that multiple electrons will not be excited at the same time. This limits the atom to the transitions that are possible for its ground state structure. This means that elements where Z is <11, only $K\alpha$ X-rays can be expected to be observed. As Z increases so do the number of electrons, filling more shells and increasing the complexity of the spectrum. This results in more varied transitions.

As Z increases so does the energy required to remove the innermost electrons. When operating within the bounds of normal SEM operation, i.e. $E_e$ <30 keV, the beam energy also limits the possible transitions. In practice when Z $\leq$20 only the *K* series X-rays are observed. When 20< Z <50 both the *K* and *L* series can be observed. When Z $\geq$50 the *L* and *M* series can be observed, due to the higher energy required to remove a *K* shell electron. As the energy levels within an atom are so well defined, characteristic X-rays have a very narrow energy width, a few eV. Any broadening observed in spectra is down to the energy resolution of the detector and the contribution of the Bremsstrahlung X-rays. Broadening may also be caused by a failure to resolve lines that are close in energy.

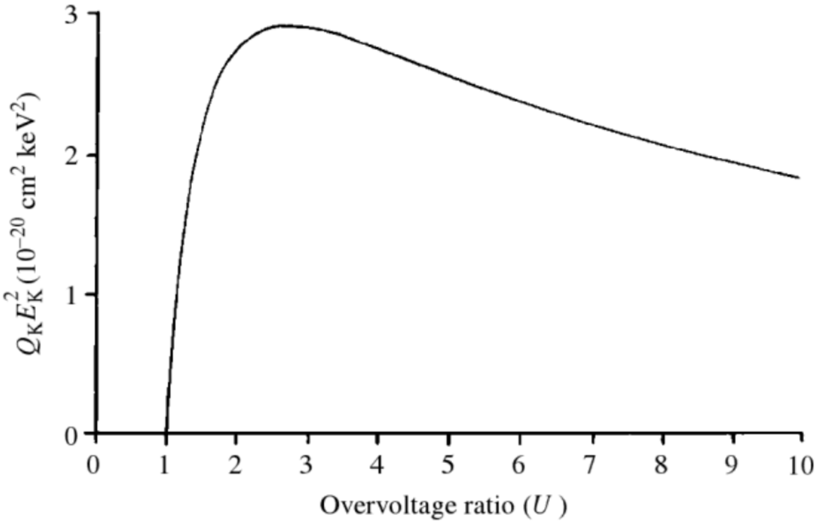

Figure 3.11: A graph showing how the rate of X-ray production changes with overvoltage for a non-specific element [64].

To describe the probability of an inner shell ionisation occurring, once again we need to lean on Bethe's work [48]. The total cross section, $\sigma_{xc}$, is given by:

$$\sigma_{xc} = \frac{\pi e^4 b_s n_s}{U \mathrm{E}_C^2} \ln(c_s U) \tag{3.11}$$

where $\mathrm{E}_c$ is the critical ionisation energy, $n_s$ is the number of electrons within a specific shell or subshell, $b_s$ and $c_s$ are constants that vary with each shell and $U$ is the overvoltage given by $U = \frac{\mathrm{E}}{\mathrm{E}_c}$. The overvoltage is a predictor for the efficiency of X-ray production. The optimum ratio for efficient X-ray generation is 2.7, but anything over 2 is deemed acceptable. This is shown in fig. 3.11. There have been many other expressions produced since Bethe's efforts, but they are all based on eq. (3.11). An interested reader could consult Powell's extensive review [63]. The information obtained from eq. (3.11) is that the incident electron is barely deviated (<10 mrad) as is expected by an inelastic collision The characteristic X-rays are also emitted uniformly in all directions across $4\pi$ sr as previously stated.

Bremsstrahlung, or deceleration, X-rays are produced when the incident electron is decelerated by the effective field of the nucleus when it is within interaction range. As the present Coulomb field reduces the velocity of an electron the lost energy, $\Delta$E, is converted into a photon of frequency $v$. The relationship between these two values is given by:

$$\Delta \mathrm{E} = hv \tag{3.12}$$

where $h$ is Planck's constant. Due to the nature of these interactions the X-rays can be produced at any frequency within the bounds of an upper limit dictated by the incident beam energy. The corresponding wavelength, linked via eq. (3.10), is known as the Duane-Hunt limit. The significance of this limit is not related to the X-ray itself, but in its ability to provide an accurate measurement of the incident beam energy as it interacts with the sample.

This continuous spread of Bremsstrahlung X-rays, in general, is simply noise on the spectrum. However this continuum does carry useful information. The intensity of the background across the whole continuum varies with the average Z within the interaction volume. This means that areas with differing structures or compositions can be identified as such, although impurities and other inclusions can lead to misinterpreted data if not considered properly.

Characteristic X-rays require the excitation of an electron from an inner shell which means that the interacting electrons require an energy $E_e > E_c$. This limits the proportion of the interaction volume which can contribute. On the other hand Bremsstrahlung X-rays can be produced by electrons of any energy meaning that the entirety of the interaction volume can contribute towards this signal. As characteristic X-rays can only be produced by electrons with an energy higher than that required for ionisation, to quantify the volume in which characteristic X-rays are produced a simple modification to the range defined in eq. (3.6) can be made. Instead of using the terminating energy as a lower limit, the ionisation limit can be used to create a range within which characteristic X-rays are produced.

Auger electrons will be the only product to fall in the 'other detectable products' category that are significant. This is in part due to the fact that it is a direct competitor to the production of X-rays. It is the alternative method that atoms have to release the energy gained by returning to their ground state after the ionisation of an inner shell electron. As shown in fig. 3.12 after the ionisation occurs an electron drops to the ground state. The energy gained is transferred to the Auger electron and it escapes the orbit of the atom. Once emitted these electrons behave in an expected fashion although the energy is not equal to the difference between the energy levels involved in the transition as is the case for an X-ray. The production of an Auger electron requires an outer shell electron to overcome its binding energy meaning its energy is the difference between that and $E_c$. This means that Auger electrons have their

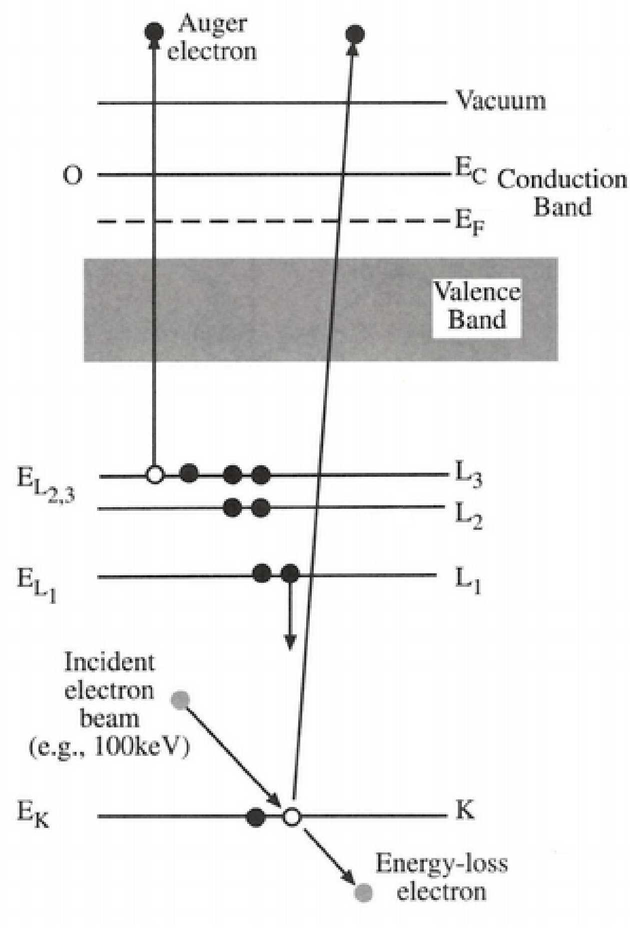

Figure 3.12: Ionisation of inner shell electrons and the production of Auger electrons via the de-excitation of outer electrons, [9].

own characteristic energies that are close but not identical to characteristic X-rays. Auger electrons are strongly absorbed by the material within the sample meaning that, just like with SEs, those that do escape typically originate from near the surface. Unlike SEs these electrons carry significant chemical information with them, due to their characteristic energies. This allows them to be used to investigate surface oxidation and topography with a technique known as Auger electron spectroscopy [65].

The direct competition between the production of characteristic X-rays or Auger electrons after an inner shell ionisation event is described by the fluorescence yield, denoted $\omega$. For the $K$ series, or any of the other series, the value of $\omega$ is given by the total number of related photons produced over the total number of shell ionisations. A quick analysis of $\omega$ for the $K$ shell reveals that at low Z the production of Auger electrons dominate and as Z increases $\omega$ tends towards unity. This implies that X-ray production dominates. Similar trends are observed for the $L$ and $M$ shells.

## 3.2 Monte Carlo Simulations of Electron Beams

With the probabilistic nature of electron interactions within samples, Monte Carlo simulation techniques prove to be a very powerful technique that can provide information on both the interaction products expected to be detected and the physical parameters of the electron's scattering within the sample.

The methodology behind the implementation of Monte Carlo simulation techniques may vary, but there are several common themes that separate it from other numerical methods. Monte Carlo simulations rely on repeated random sampling to obtain the statistical properties of a physical system. This approach is typically used when there are a large number of degrees of freedom. The methodology relies on the law of large numbers, taken from probability theory. This states that when a sufficiently large number of data points are averaged the average should approximately be the expected value.

One of the key cornerstones of Monte Carlo simulations is the use of random numbers, whether they are true or pseudo-random. This may be to define inputs or in the case of CASINO to evaluate the interactions an electron experiences during its propagation though a sample. When solving a problem without an analytical solution this means the average should be the answer. In all systems Monte Carlo simulations also produce a probability distribution for outcomes. This is because for each variable they also interact with a probability distribution, ensuring rare events remain rare and more likely scenarios happen across the distribution of results more frequently.

Monte Carlo simulations have been used to study the capabilities of electron microscopes for a long time. As discussed in section 3.1.1 most of the mathematics used in more traditional programs fell down when used to simulate beam energies <10 keV. Around 30 years ago field emission sources such as Schottky emitters, see section 2.1.1, were introduced into electron microscopes. This allowed for the production of a beam with a very high current density and a very small spot size, all at low energies. CASINO was developed to fill the void in simulation software for low energy beam interactions that this created.

As well as using semi-empirical mathematics and experimentally derived values for low energy interactions CASINO also allows for both 2D and 3D sample modelling and analysis. These options resulted in a deviation of the software, forming a lighter package for 2D simulations and a more resource intense option for 3D simulations. The features of each package and anything relevant to the interpretation of its outputs is presented below.

### 3.2.1 CASINO in 2D

CASINO version 2.4.8.1 is the software used during this work for all 2D simulations. Details on how it was used will be covered here. Technical information is also available in Drouin *et al.* [66]. It is worth noting that the program has many features, but the discussion will be limited to those that were used. Where the mathematics ued differs from that discussed earlier there will be a comment.

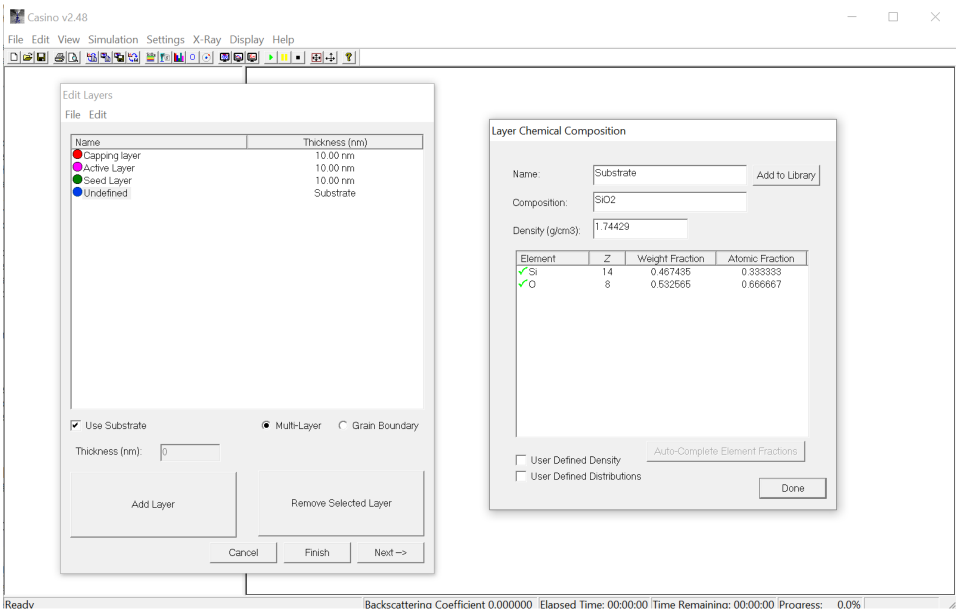

| Name | Thickness (nm) |
|---|---|
| ● Capping layer | 10.00 nm |
| ● Active Layer | 10.00 nm |
| ● Seed Layer | 10.00 nm |
| ● Undefined | Substrate |

☑ Use Substrate ● Multi-Layer ○ Grain Boundary

Thickness (nm): 0

Name: Substrate

Composition: SiO2

Density (g/cm3): 1.74429

| Element | Z | Weight Fraction | Atomic Fraction |
|---|---|---|---|
| ✓ Si | 14 | 0.467435 | 0.333333 |
| ✓ O | 8 | 0.532565 | 0.666667 |

☐ User Defined Density
☐ User Defined Distributions

Ready | Backscattering Coefficient 0.000000 | Elapsed Time: 00:00:00 | Time Remaining: 00:00:00 | Progress: 0.0%

Figure 3.13: CASINO's interface for sample entry.

When starting a simulation the first step is to enter the sample details, shown in fig. 3.13. Simply add the number of layers required and double click on a layer to edit its properties. At this stage it is imperative to ensure that the layer stoichiometry is correct. This allows the software to look up and calculate the correct density easily. Stoichiometry can be edited either by writing it in the composition as shown in fig. 3.13 or it can be manually adjusted by weight or atomic fraction in the element list. Once the compositions are correct the thickness of each layer can be adjusted similarly. CASINO will generate a layer which has the thickness and densities given, but will be infinite in the $x$ and $y$ direction.

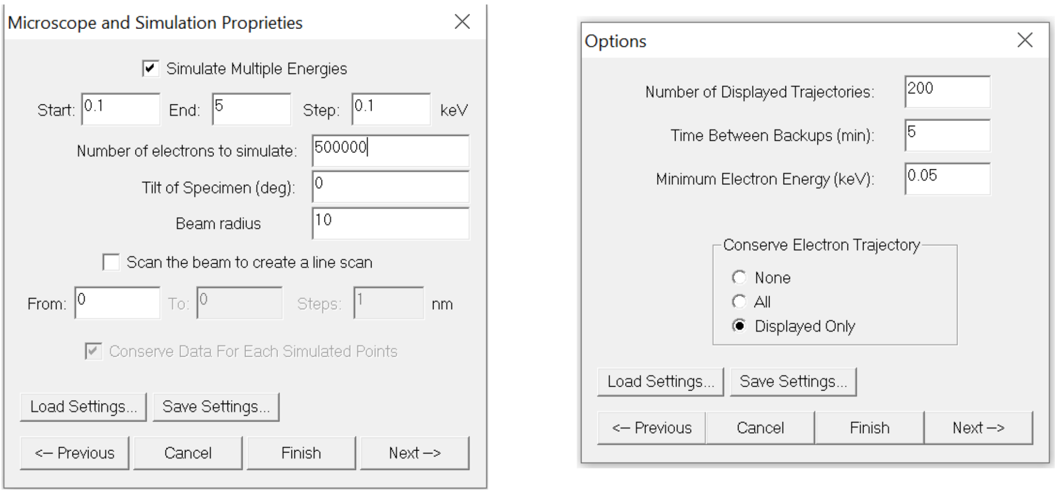

Microscope and Simulation Proprieties

☑ Simulate Multiple Energies

Start: 0.1 End: 5 Step: 0.1 keV

Number of electrons to simulate: 500000

Tilt of Specimen (deg): 0

Beam radius 10

☐ Scan the beam to create a line scan

From: 0 To: 0 Steps: 1 nm

☑ Conserve Data For Each Simulated Points

Options

Number of Displayed Trajectories: 200

Time Between Backups (min): 5

Minimum Electron Energy (keV): 0.05

Conserve Electron Trajectory

○ None

○ All

● Displayed Only

a b

Figure 3.14: CASINO's interface for a. the entry of simulation parameters and b. the visualisation parameters.

The next step allows a user to select the simulation range, the step size and the number of electrons to simulate. Typical values for this work are shown in fig. 3.14a. The beam radius is measured in nm. When multiple energies are simulated they are ran and processed sequentially. No estimate for the total time of a batch run is ever made. Once these details have been entered when a user clicks next a screen which allow a user to customise the simulations distributions is shown. Here a user is able to set the maximum range an electron can reach, based on the simulated pathway, the Kanaya Okayama limit discussed earlier or a fixed value. Given the use of a modified Bethe equation, eq. (3.5), in all cases the fixed selection is the only one that may provide significantly different results.

Figure 3.14b is the next option screen. The options here can have an impact on general speed. It is possible to increase the cut-off energy for spent electrons, *i.e.* electrons which are no longer tracked. This can greatly reduce time taken, particularly in high energy simulations. In addition the user may select the number of trajectories displayed. These are always the trajectories for the first electrons simulated, and explains why a large sample size simulation can appear quite different. Random pathways can differ a lot. However the larger the sample size, the more the results converge on the expected values. This is the reason this work uses 500000 electrons during simulations. In section 4.3 the reproducibility of these simulations is discussed.

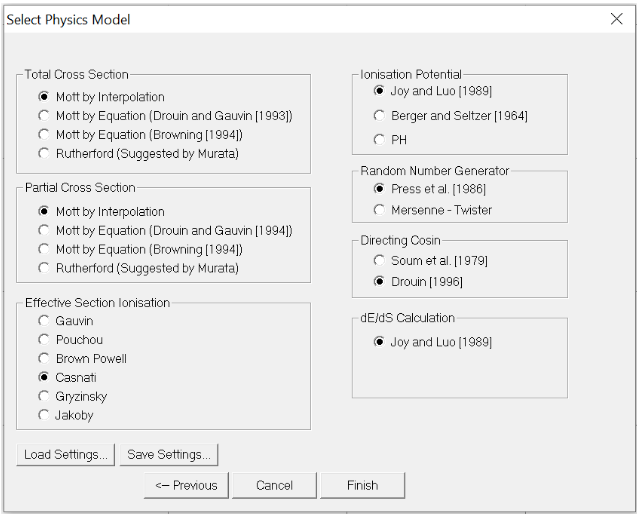

Total Cross Section
- ● Mott by Interpolation
- ○ Mott by Equation (Drouin and Gauvin [1993])
- ○ Mott by Equation (Browning [1994])
- ○ Rutherford (Suggested by Murata)

Partial Cross Section
- ● Mott by Interpolation
- ○ Mott by Equation (Drouin and Gauvin [1994])
- ○ Mott by Equation (Browning [1994])
- ○ Rutherford (Suggested by Murata)

Effective Section Ionisation
- ○ Gauvin
- ○ Pouchou
- ○ Brown Powell
- ● Casnati
- ○ Gryzinsky
- ○ Jakoby

Ionisation Potential
- ● Joy and Luo [1989]
- ○ Berger and Seltzer [1964]
- ○ PH

Random Number Generator
- ● Press et al. [1986]
- ○ Mersenne - Twister

Directing Cosin
- ○ Soum et al. [1979]
- ● Drouin [1996]

dE/dS Calculation
- ● Joy and Luo [1989]

Figure 3.15: CASINO's interface for selecting the Physics model.

The final step of any simulation is selecting the physical models to be used for the simulation of an electron trajectory. This interface, shown in fig. 3.15, is intended for expert users and has extensive options. The options that are selected in fig. 3.15 are both the default options and those used in this work. This is because these options are the most recent developments and have been shown to more accurately represent the physical system.

The alternative selections can be found in using the author and year given within the software, but the chosen options calculate the electron pathway as follows. These equations are taken from Drouin *et al.* [66]. First the landing position is calculated. This is given by:

$$X_0 = \frac{d\sqrt{\log(R)}}{2 \times 1.65} \times \cos(2\pi R)$$
$$Y_0 = \frac{d\sqrt{\log(R)}}{2 \times 1.65} \times \cos(2\pi R) \tag{3.13}$$

where $X_0$ and $Y_0$ are the landing position coordinates, $d$ is the user entered beam diameter and $R$ is a random number between 0 and 1. $R$ is a different number each time it is called even within an equation. The penetration angle is given by the user.

With the starting position of the electron calculated the distance between two collisions, $L$ measured in nm, must be found. This is given by this equation:

$$L = -\lambda_{el} \log(R) \tag{3.14}$$

where $\lambda_{el}$ is calculated using:

$$\frac{1}{\lambda_{el}} = \rho N_0 \sum_{i=1}^{n} \frac{C_i \sigma_{el}^i}{A_i} \tag{3.15}$$

where $C$ is the weight fraction. The value of $\sigma_{el}$, the elastic cross-section can be found in different ways, but the default option is to use the look up values which can be found in Drouin *et al.* [67]. These have been pre-calculated for every element, and the regions composition dictates which values are chosen.

With the distance between collisions found the next step is to find out how much energy is lost due to inelastic scattering. As previously discussed a modified Bethe equation is used. This requires an assumption that the inelastic collisions will not adjust the trajectory of the electron and that the electron will lose energy at a constant rate across its travel. With these assumptions in mind, the $\mathrm{E}_e$ measured in keV, is found using:

$$\mathrm{E}_e^{i+1} = \mathrm{E}_e^i + \frac{d\mathrm{E}}{dS} L \tag{3.16}$$

where:

$$\frac{d\mathrm{E}}{dS} = \frac{-7.85 \times 10^{-3} \rho}{\mathrm{E}_e^i} \times \sum_{j=1}^{n} \frac{C_j Z_j}{F_j} \ln\left(1.116\left(\frac{\mathrm{E}_e^i}{J_j} + k_j\right)\right) \tag{3.17}$$

where $J$ is the mean ionisation potential and $K$ is a variable which is solely dependant on Z. More information on this variable is given in Gauvin and L'Espérance [68]. $\frac{d\mathrm{E}}{dS}$ has the units keV/nm.

With the energy of the electron known the last step is to calculate the collision angle, to allow the electron to continue on its path. There are many options for this as well, but the default uses similarly tabulated values to identify the elastic collision angle. These are known as partial elastic cross-section values and can also be found in Drouin *et.al* [67]. It is worth noting that these are element specific. In a mixed element environment the element responsible for the collision will be chosen to find the angle. This whole process will be repeated until the electron reaches the minimum electron energy, or escapes the surface of the sample and is classified as a BSE. When an electron enters a new region, *i.e.* a new layer, $L$ is recalculated.

With all the models selected it is necessary to generate data. For this work the focus was the BSE data, shown in fig. 3.16, but it is possible to see the many options available. This project focussed on the maximum depth that

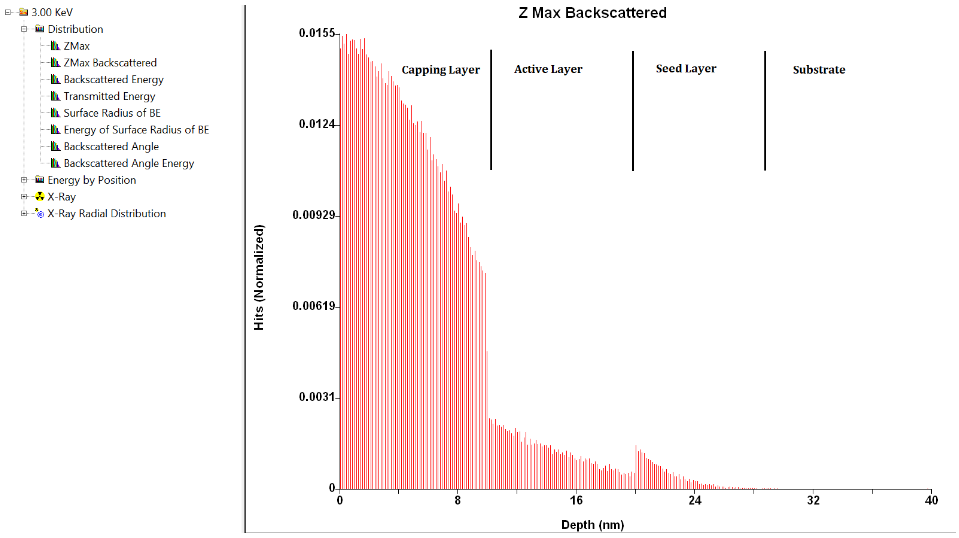

Figure 3.16: BSE data as produced by CASINO. This is for the sample structure entered in fig. 3.13, and marked above the graph, simulated at 3 keV. Hits(Normalised) is the number of simulated electrons that escaped and became BSEs and that reached the maximum depth over the total number of simulated electrons.

the BSEs reached. This was measured in Hits(Normalised). Hits(Normalised) is the number of simulated electrons that reached the maximum depth over the total number of simulated electrons. This data can be exported as either an image or, more usefully, a .txt. This allows further analysis to take place. In the case of this work this is typically counting the number of BSEs which reach their maximum depth within each layer. This is used to produce the simulation graphs seen throughout. In fig. 3.16 it is quite clear there are steps in BSE generation. This is caused by the substantial changes in Z between the layers.

### 3.2.2 CASINO in 3D

For 3D simulations CASINO version 3.2.0.4 was used. Full details on this software can be found in Demers *et al.* [69]. It is important to note that there is no difference in the methodology to calculate the electron pathway, it uses an identical method to the 2D version. The only difference in this program is the ability to model 3D structures. Due to this there isn't a need for an in-depth look at the program. Simply the knowledge that 3D structures can be created is enough. An example of such a structure is shown in fig. 3.17. Outside of the model it is assumed to be vacuum, as it is trying to replicate an SEM.

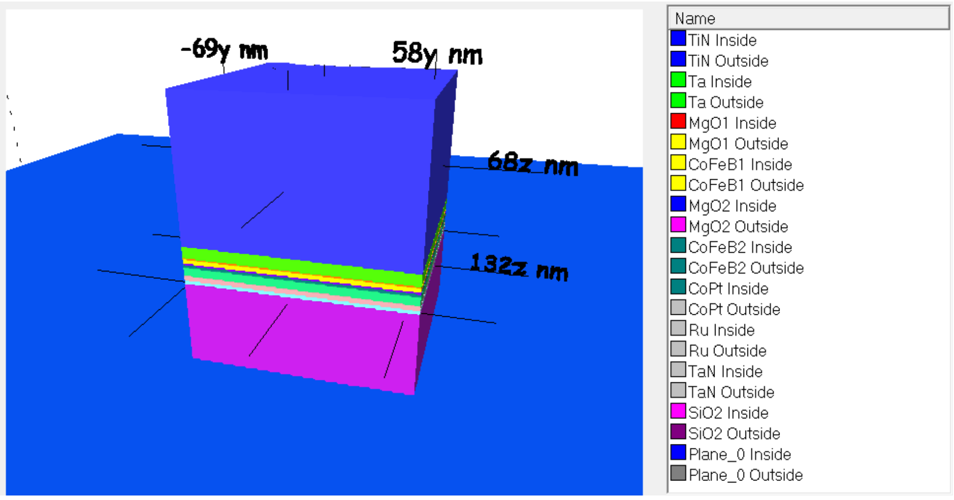

Figure 3.17: A 3D sample model crated in CASINO.

The data produced can be used in a similar way to the data produced in the 2D version. However the program itself takes significantly longer to run so it was only used when geometric effects were a major concern in this work.

# Chapter 4

# Technique Development

With the indicative work [6] discussed in chapter 1 as a starting point several fundamental steps need to be taken to establish the functionality of this technique. A robust tool for simulation needs to be utilised, outlined in section 3.2. Alongside that it is imperative to develop an analysis methodology and software to be able to measure repeatable changes in contrast. This development should allow for quicker analysis as well. Finally it is important to test and fine tune both the simulation software and the comparative software.

## 4.1 Tool for Image Analysis

As the technique in development requires the direct comparison of two very similar images, taken using an SEM at different beam energies. These are stored in a bitmap format so several steps were outlined to accomplish this. These steps were: crop image; readjust the contrast; align and transform the image; then perform the comparative action. To accomplish this a semi-automated program was coded using MATLAB. The code used can be found in appendix B. A fully automated version was initially developed but this produced too many errors in comparisons between feature-sparse images.

### 4.1.1 Cropping and Contrast

When an image is captured in most SEMs it can be saved in an image format. This very often has a standardised resolution and includes important information such as a scale bar and the acceleration voltage. Whilst this information is very important when attempting to overlay two images, particularly by automated means all it does is hinder efforts. For this reason the first step in analysing the images is to crop this information box. This is a simple action as the information boxes are identical in each image. The images are cropped outside of a box which is 1280 x 960 pixels, removing the details box.

During the operation of an SEM a user has significant control over the brightness and contrast shown in a captured image. It was thought that the levels of brightness and contrast are unlikely to be the same in each image taken. As a comparison of the contrast in each image is the goal of this analysis it was deemed necessary to standardise the levels in each image for a more realistic comparison. An example of an electron image before any adjustment is shown in fig. 4.1a. After the rescaling the image looks similar to fig. 4.1b. Not only does the act of rescaling ensure all images have equal contrast, it can also reveal some difficult to resolve features, such as in fig. 4.1b.

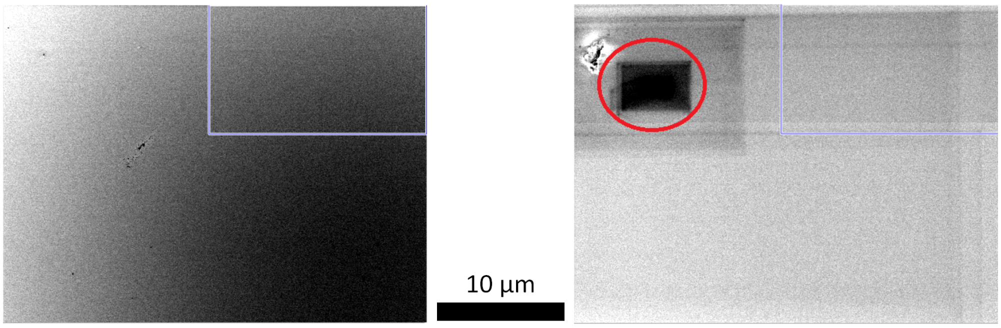

a

b

Figure 4.1: SEM images after their contrast has been rescaled. The sample in this image is described in section 4.2. The light grey rectangle in the top corner of each image is a magnifying square, used later when selecting control points. There is no scale bar attached as it has been cropped as part of the alignment process.

During the operation to adjust or rescale the contrast and intensity the image is shifted such that the top 1% and bottom 1% of all pixels are saturated, showing white or black respectively. Looking at the rescaling in fig. 4.1a, the surface defects are prominent and it appears likely that the sample was slightly tilted due to the gradated change observed. Figure 4.1b represents a more typical rescaling which highlighted the carbon compounds that have been fixed to the surface, the bright object seen in the top left. The dark rectangles, highlighted with the red circle, are created when carbon is deposited on the surface in the field of view. As the field of view is expanded it shows up as a dark region as less BSEs are produced there compared with clean surface. The smaller the field of view the higher the dose of electrons received, resulting in more carbon fixation.

As images are taken in batches or groups each image undergoing comparison will be subject to approximately the same environment, the only difference being the beam energy and the detail that reveals. This means that any geometric contrast should be consistent across the series, meaning it will disappear when the images are overlaid. This procedure ensures that the rescaling of contrast remains a sensible option. The only environmental changes expected during the imaging of an image series is the fixation of carbon compounds, shown in fig. 4.1b, and the build up of charge. Charge can have an unpredictable effect on the image so steps must be taken to reduce its effects, such as those laid out in section 2.1.4.

### 4.1.2 Image Alignment

Now there is a fixed contrast scale across the images a comparison can be made. It is highly likely that images taken at different beam energies will have a different frame of reference due to the small changes in beam alignment and field of view. This prevents a comparison from being made straight away. To account for this, two different methodologies were developed. A method for manual alignment and automatic batch alignment were developed within the MATLAB environment. Details of the code used for manual alignment can be found in appendix B.

#### Manual Alignment

The manual alignment, shown in fig. 4.2, relies on a set of user selected control points to rotate and transform one of the images, usually the lower acceleration voltage, to align with the other reference image. The user will select a number of points, usually between 4 and 8, at the same position on both images. To increase accuracy an automatic check of the surrounding pixels is made at each set of points. This aims to account for user input accuracy and will allow each point to be moved a small distance, approximately 10 pixels, to a more similar position.

Once these control points have been selected they are used, by the code, to align the second image with the reference image. This alignment uses and combines several different transformation types to achieve success. The image can be moved laterally to ensure alignment, taking care of simple location error. The image can also be rotated to account for any shift caused by the electron optics. In addition, the image can be geometrically transformed to account for magnification errors or, more likely, field of view changes due to the differing acceleration voltage used. Finally asymmetric transformations can be employed to try t take care of distortions that occur in certain regions of the image when focusing and alignment have not been done optimally.

These aligned images can then be used to perform comparisons. In general this method proved to be highly effective, limited only by the users ability to discern suitable control points. As each set of images needs user input it is a very time consuming endeavour. Given a similarly experienced user the alignments are also very reproducible, with a comparison shown in fig. 4.2. It is worth noting that there are no distortion corrections within this code. However if the electron image uses the SEM's distortion correction all images that are being compared should do so.

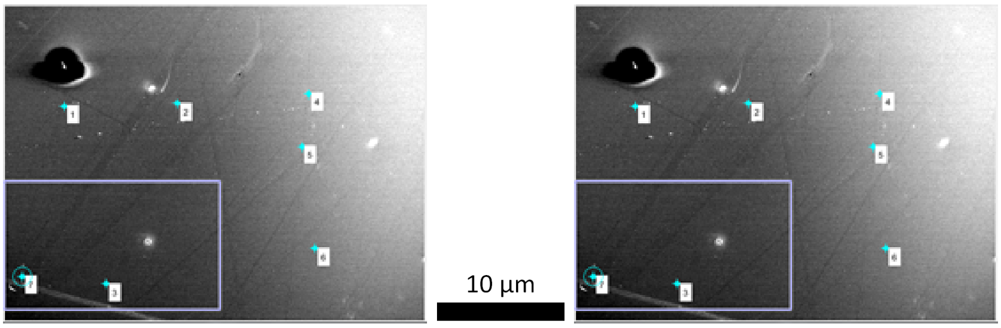

a b

Figure 4.2: The selection of control points on the two images taken with differing keV to ensure alignment fr the subtraction. These white boxes just label the control points from 1 to 7. The grey box allows the screen to be magnified, making control point selection more precise. The sample that was imaged here is described later in chapter 6. There is no scale bar as this has been cropped out as part of the alignment process.

### Automatic Alignment

In an effort to reduce the time taken to process large batches of images an automatic program has been developed. The only information required is the series of images that are being compared. The code will then attempt to align the image by aligning sets of pixels that are similar, *i.e.* aligning features. Some results are shown in fig. 4.3. Whilst this method reduced the time taken significantly it did have several drawbacks.

When comparing images with one or two features or many indistinct features the successful alignment rate was <50%. This limits its application to samples which provide a distinct set of features, such as devices. The reproducibility of alignment is also quite varied depending on the sample. Particularly in the case where there are many indistinct features, the product of the alignment could be quite different. Once again this limited the use of the automatic process to investigations with device like samples.

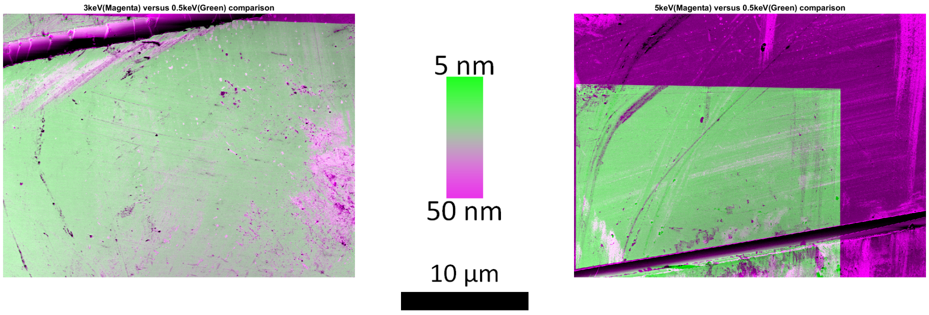

a

b

Figure 4.3: The results of two separate automatic alignments. In one case good alignment was achieved and in the other it was not. The sample imaged here is S1, which is discussed in section 4.2. Its structure is Si(sub)/Ta(0.5)/CoFeB(1.2)/MgO(1.5)/Ta(2)(thickness in nm).

In general the automatic alignment was used during preliminary investigations to identify regions or samples of interest. During more targeted investigations the manual comparison method was chosen for its reliability and reproducibility. This provided the best balance of speed and confidence.

### 4.1.3 Image Comparison

Irrespective of the alignment method the images need to be compared to produce any useful results. Two different comparisons have been developed. The first is a simple subtraction where the intensity value of each pixel within the image is subtracted from the corresponding pixel in the reference image. The second comparison method developed is a pixel by pixel comparison. In this comparison instead of using a straightforward subtraction the program retains information about which image is more intense and the relative difference in intensity between the two images.

### Image Subtraction

As the images for comparison have already been aligned and mapped over each it is a simple step to subtract one matrix of pixel intensities from another. The subtraction results can be seen in fig. 4.4. With no further post processing the images appear dark and details can be obscured. This is because the process of subtraction naturally results in a lower average intensity across the pixels. For this reason it was decided that after subtraction has occurred the resultant image should have its contrast readjusted in the same manner as described in section 4.1.1. This readjustment is shown in fig. 4.5.

The resultant image from this subtraction is easy to interpret, any features that arise from differences between the two chosen acceleration voltages and the respective penetration depths. Using the original images a visual check can indicate the origin of these features, whether it is from the surface or some sub-surface area. Some examples of the types of features that can be seen are shown in fig. 4.4.

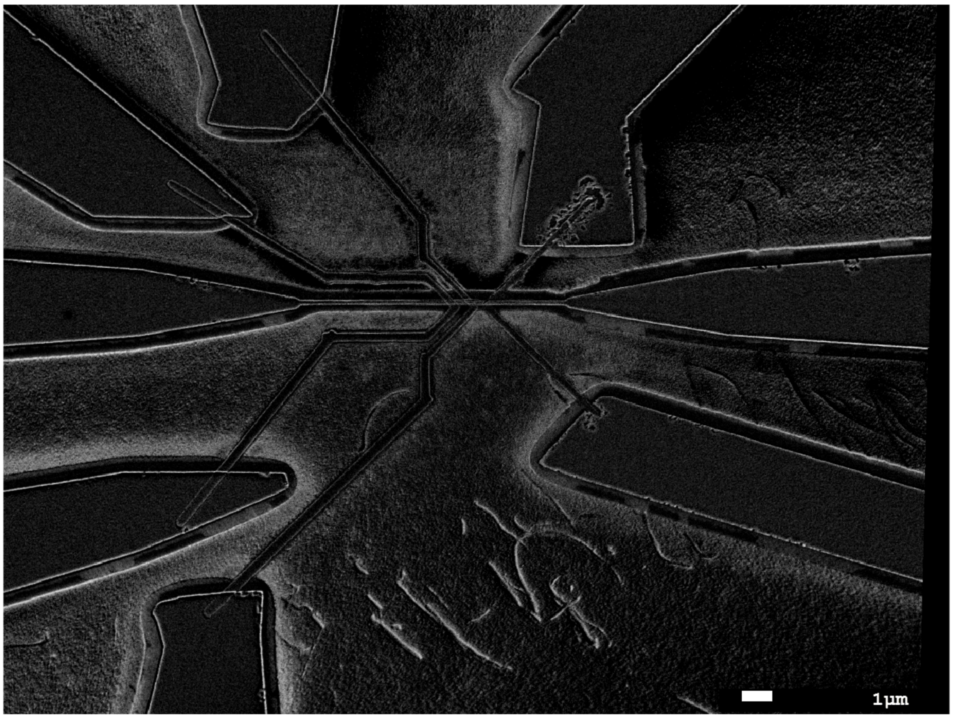

Figure 4.4: The subtracted images. These were aligned using the manual method. This sample is an array of 100 nm wide Cu, Pt and Permalloy wires deposited on $SiO_2$. The deposited wires should also be 100 nm thick. The voltages used were 2 and 3 keV.

However, in many cases, the origins of these features can be much harder to discern. This is particularly true when the original images are similar, with

Figure 4.5: Subtraction images after their contrast has been rescaled. This sample is an array of 100 nm wide Cu, Pt and Permalloy wires deposited on $SiO_2$. The deposited wires should also be 100 nm thick. The voltages used were 2 and 3 keV.

only subtle differences in features. One such example is shown in fig. 4.5. This can be further complicated by geometric discrepancies, such as a tilt of the sample. In these cases subtraction is not enough.

### Pixel Comparison

This comparison uses the same set of aligned images as the subtraction. In fact for ease, both are performed in parallel for all comparisons. Once again the aligned pixels are mapped over each other. Instead of subtracting the intensity values they are compared. An example of this comparison is shown in fig. 4.6.

The first step of the comparison is to identify to which image the pixel with the highest intensity belongs, the image with the higher penetration depth or the image with the lower penetration depth. If the image with a lower penetration depth has a higher intensity the pixel is coloured magenta. The exact shade is based on the relative difference between images, with a lighter shade representing a smaller difference. If the reverse is the case and the image with the lower penetration depth has the higher intensity then the pixel will be

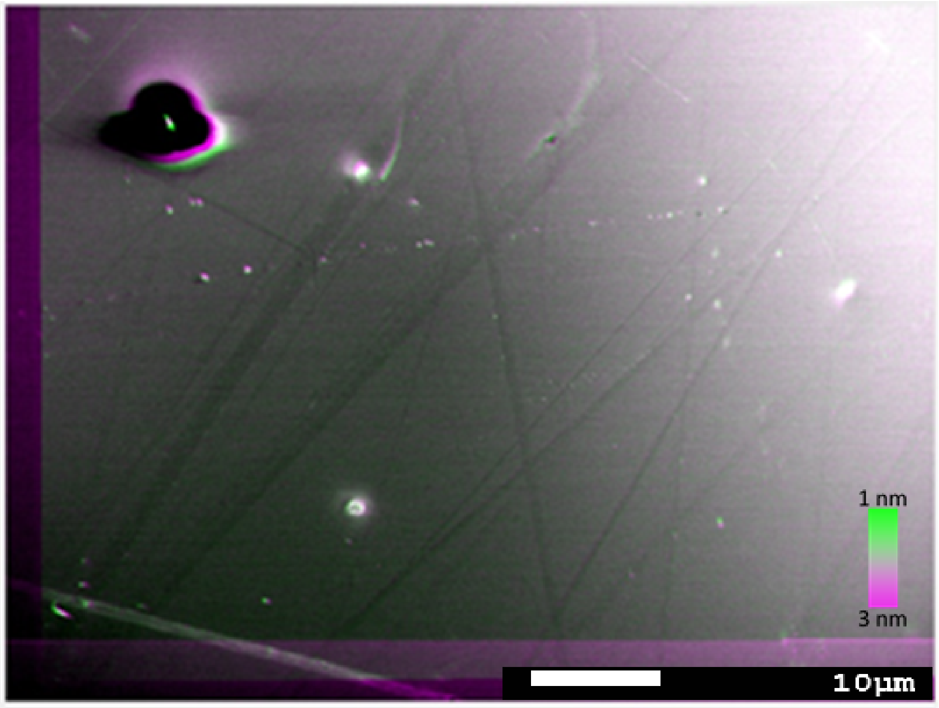

Figure 4.6: A resultant pixel comparison. This was processed using the manual selection. The scaling shade of green and magenta can be used to give an approximate depth scale, which is in the bottom right. The acceleration voltages used were 2 and 2.2 keV. The sample that was imaged here is described later in chapter 6.

coloured green with a similar scaling of the shade. This acts to both highlight hard to distinguish features but also allows simple identification of the origin of those features.

A third state can be found during this comparison. This is a situation where the pixels have a very similar intensity, approximately 5% difference. In these cases the pixel will retain its intensity. This retains potentially important information about the structure or features of the sample under investigation in an opposite fashion to the subtraction method.

Whilst this method retains more information than the subtraction method it is not more difficult to analyse the results. The colour coding allows a user to quickly identify in which image a feature is seen more strongly, and when used alongside detailed penetration depth simulations, an approximate depth scale can be inferred. An example of this is shown in fig. 4.7. Just for clarity any features that retain their original colouring and intensity cannot be bound by this scale and no approximation for their depths can be made.

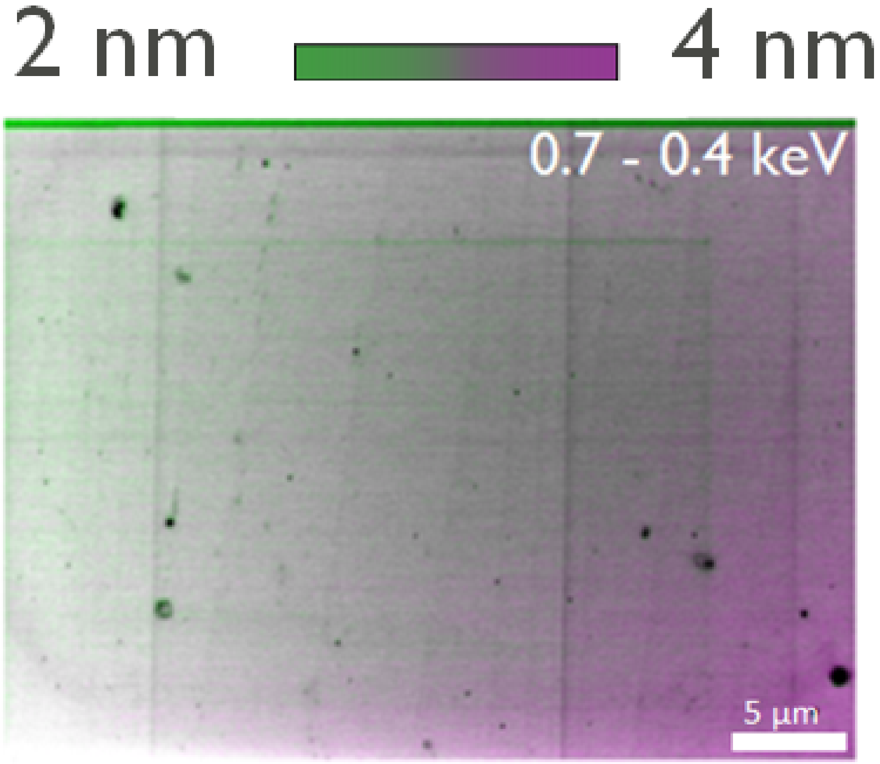

Figure 4.7: A composite subtraction image with approximate scale bar. The sample, S1, that was imaged here is described later in section 4.2.

### 4.1.4 Image Analysis Overview

The above sections outline the details of the image analysis methodology developed to use alongside this technique. This has also been summarised in fig. 4.8. The technique in question utilises a controlled penetration depth to probe sub-surface features. As the only information on the depth penetrated is probability data from Monte Carlo simulations using CASINO, it is better to image across a series of beam energies, and equivalent penetration depths, to allow for a more thorough comparison. This is particularly important when unpredicted geometric effects need to be accounted for.

As the analysis is just as experimental as the method, care has been taken to ensure the results are both repeatable and relevant. Particular care was taken to ensure sufficient simulations were performed to approximate the penetration depth for each beam energy with each sample. For more details on the simulation methodology see section 3.2. When dubious or interesting results appeared they were retested and then investigated using other more well recognised techniques. These interesting results became the basis of the work

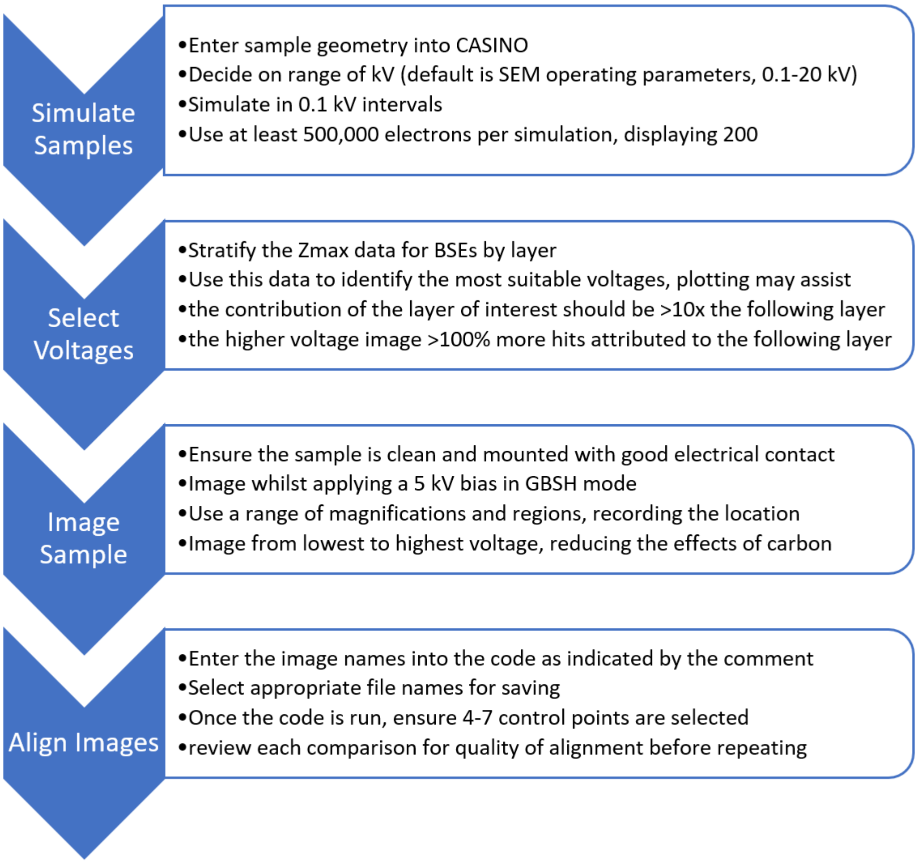

- Enter sample geometry into CASINO
- Decide on range of kV (default is SEM operating parameters, 0.1-20 kV)
- Simulate in 0.1 kV intervals
- Use at least 500,000 electrons per simulation, displaying 200

- Stratify the Zmax data for BSEs by layer
- Use this data to identify the most suitable voltages, plotting may assist
- the contribution of the layer of interest should be >10x the following layer
- the higher voltage image >100% more hits attributed to the following layer

- Ensure the sample is clean and mounted with good electrical contact
- Image whilst applying a 5 kV bias in GBSH mode
- Use a range of magnifications and regions, recording the location
- Image from lowest to highest voltage, reducing the effects of carbon

- Enter the image names into the code as indicated by the comment
- Select appropriate file names for saving
- Once the code is run, ensure 4-7 control points are selected
- review each comparison for quality of alignment before repeating

Figure 4.8: The work flow for a generic investigation using the non-destructive interfacial imaging technique. This summarises the approach used in all investigations in this work.

documented.

Using this image analysis allows a number of different types of interfacial defects to be highlighted. A void in an interface, caused by mechanisms such as lattice mismatching or separation of layers, will be highlighted as a dark region. This is because there is a lower local density, reducing the total number of BSEs produced there. Similarly intermixing can be highlighted through the same mechanism, although this can be either lighter or darker, depending on if the mixing element has a higher or lower Z. It is worth noting that if intermixing is uniform across a region it won't be shown using this technique as the density will be consistent. Steps, both positive and negative, will be identified by an abrupt change in contrast, similar to in fig. 4.7. In general changes in Z or density are what are likely to be identified using the technique.

## 4.2 Thin Film Investigations

Following on from the previous work described in [6], thin film multilayer samples were chosen to demonstrate and test the capabilities of this proposed technique during its development. These types of samples are able to provide clear atomic number contrast between layers and, with careful control of deposition, can be produced with a known thickness reliably.

Four different six inch wafers, each with a duplicate, were prepared by an external collaborator at Tohoku University for this study. The films were deposited onto silicon using sputter deposition and were annealed at 300°C in a 0.4 T field for 1 hour. The structure of the four samples are shown in table 4.1. These structures were optimised to have a large perpendicular anisotropy [70]. The duplicate was prepared to be patterned into domain wall motion devices to undergo a simultaneous study.

| **Sample** | **Thickness of individual layers (nm)** | | | |
|---|---|---|---|---|
| | Ta | CoFeB | MgO | Ta |
| 1 | 0.5 | 1.2 | 1.5 | 2 |
| 2 | 2 | 1.2 | 1.5 | 2 |
| 3 | 0.5 | 1.2 | 1.5 | 1 |
| 4 | 5 | 1.2 | 1.5 | 1 |

Table 4.1: The structure of the four wafers produced for study. The seed layer is on the left and the capping layer is on the right.

Each wafer was cleaved into two separate samples, a sample from the centre of the wafer and a sample from the outer edge. This allows for an investigation into the radial dependence of the sputtering process as well as a comparison of the films produced. Before any imaging occurred the samples were sequentially washed in acetone and isopropanol to ensure surface cleanliness. Samples were mounted onto aluminium stubs using conductive carbon tabs.

### 4.2.1 Investigation Methodology

Four distinct magnetic multilayer thin film samples designed to produce a large perpendicular anisotropy were the starting point for this study. The aims were to identify and measure any defects in the interfaces of these samples, particularly the MgO/CoFeB interface and compare the frequency of interface defects between the samples.

The first step was to simulate the samples, as outlined in section 3.2 using CASINO. Each sample structure, as denoted in table 4.1, was simulated at beam energies between 0.1 and 5 keV, increasing in 0.1 keV intervals. Each of the simulations were ran using $5 \times 10^5$ incident electrons. Using the data from the normalised graph of maximum BSE penetration depth CASINO outputs, an estimation of the percentage of BSEs produced in each layer can be made. This was done for each of the samples at every simulated beam energy. This information was then used to produce the graphs shown in fig. 4.9.

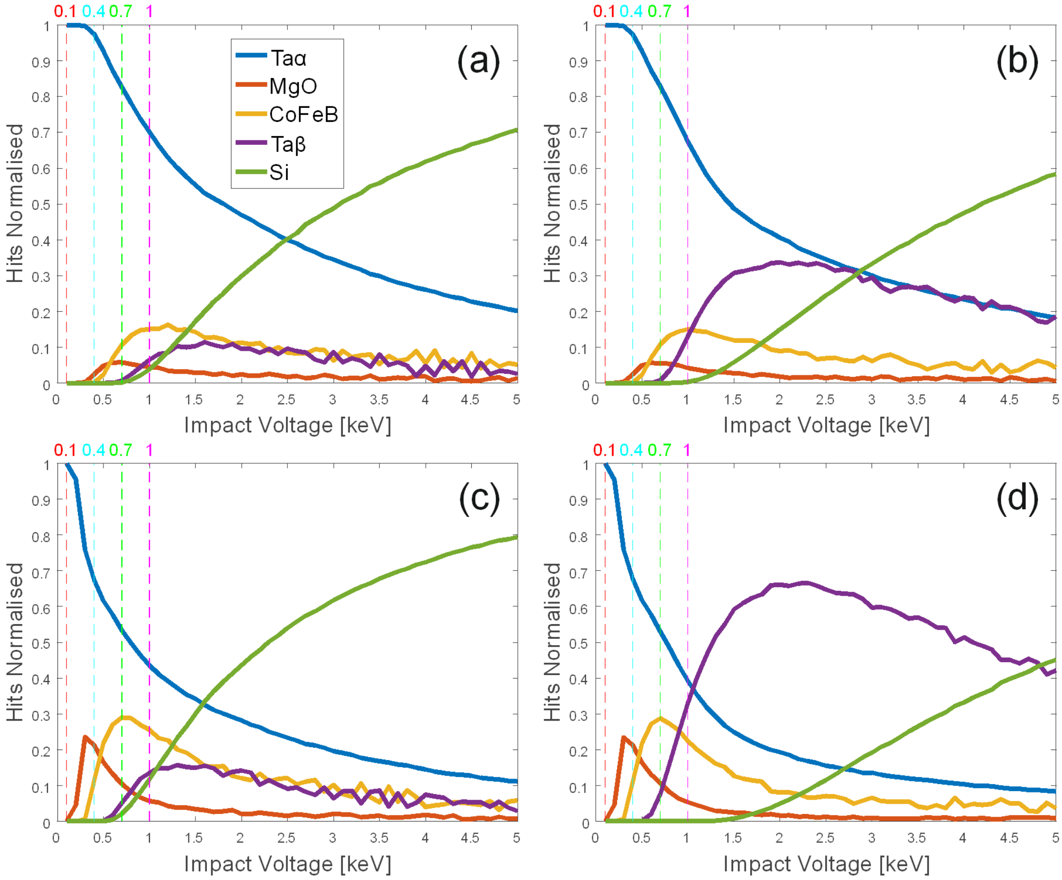

Figure 4.9: Simulations performed for samples a.1, b.2, c.3 and d.4. These were simulated between 0.1 and 5 keV in 0.1 keV intervals. $\alpha$ is used to denote the capping layer and $\beta$ is used to denote the seed layer.

Figure 4.9 was used to isolate the acceleration voltage that would be selected for imaging each layer. To define the criteria for a voltage to be selected, the proportion of Hits originating in the desired layer should be maximised, whilst ensuring that the contribution is more than 10 times that of the following layer (as you travel deeper into the sample) and that the layer after that does not contribute at all. Essentially trying to find a beam energy that produces BSEs in only that layer and the ones above it. An additional criteria is that the higher voltage, or deeper layer, image should have more than 100% more hits attributed to this deeper layer. This ensures there is a significant gain in signal to ease comparison.

Whilst simulating these beam energies found were approximated to the nearest 0.1 keV largely due to the operating recommendations of the microscope being used, but also as it would allow a much more accurate estimation to be made of the percentage contributions of each layer to the BSE image produced. Due to this and for ease of comparison, the energies 0.1, 0.4, 0.7 and 1 keV were chosen for all four samples to isolate each of the layers. Whilst these are not perfect they are a good compromise to ensure that the main interface of interest, the MgO/CoFeB interface, can be investigated.

As described in section 2.1.4 the JEOL JSM-7800F *Prime* can apply a bias voltage to the stage which acts to reduce the incoming electron beam energy by up to 5 keV. The benefits of using this bias have been previously stated. It is important to note that during this particular study the maximum bias voltage was applied. This created a need to separate the initial beam energy and the landing beam energy. This is done by referring to the reduced energy or voltage as the impact energy or voltage. In the case of this study the impact energies were equated to the target energies found during the simulations.

Each of the samples prepared were imaged extensively across a wide area at each of the desired impact energies. These locations were distributed as randomly as possible although cleaved edges were avoided. Both of these steps were taken to try to reduce operator bias and the effects of the sample preparation. Once initial sites were imaged the remaining energies were used in the same position to allow for the future subtraction. As carbon compounds frequently get fixed to the surface during imaging the sequence of accelerating voltages that were used were adjusted from the lowest to highest in the hope that the effects this may have were reduced. Once the data was gathered it was analysed using the tools outlined in section 4.1.

### 4.2.2 Identification of Defects

Following the procedure described previously to collect and analyse the data, a series of composite subtraction images were produced for all samples. The composite subtraction images were processed using the methodology described earlier. The images used were taken at 0.1 and 0.4 kV and are shown in fig. 4.10.

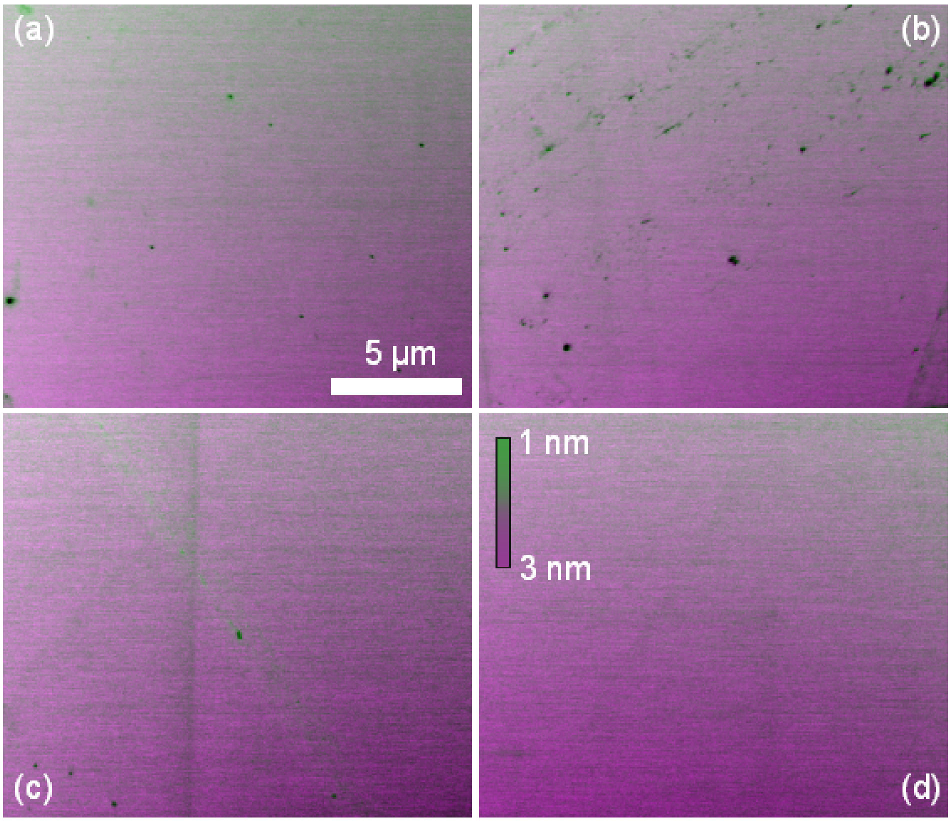

Figure 4.10: Example comparison images for samples a.1, b.2, c.3 and d.4. These focus on the Ta/MgO interface. The structure of these samples can be found in table 4.1. The acceleration voltages used were 0.1 and 0.4 keV.

This figure contains one example image from each sample, but more can be seen in appendix B. These images do not reveal any subsurface (< 3 nm) details, *i.e.* Ta/MgO interfacial features but they do highlight surface defects, which show up as green features. These features were indistinguishable before the analysis. A clear example has been shown for sample 1 in fig. 4.11. This already highlights the benefit of such a technique to effectively analyse the surface of a sample and the sub-surface.

The next composite subtraction images inspected were made using 0.4 and 0.7 kV images. An example for each of the samples are shown in fig. 4.12 with additional examples shown in appendix B. These are expected to show the

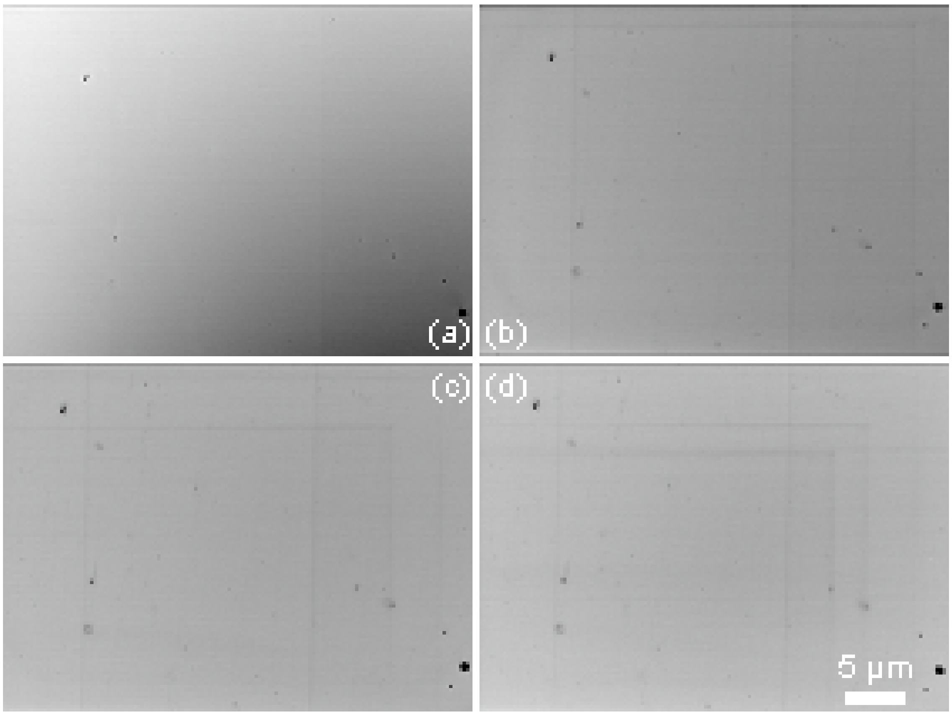

Figure 4.11: The raw, uncropped images of Sample 1 at the impact voltages of (a) 0.1, (b) 0.4, (c) 0.7 and (d) 1 keV.

quality of the CoFeB/Mgo interfaces based on the simulation data. Several vertical lines are observed in fig. 4.12 which were not present in fig. 4.10. These lines are approximately 50 nm wide. These lines are indicative of the presence of an atomic step. They are only visible in the images taken with an impact voltage higher than 0.4 keV. Similar features are seen in all of the samples imaged as can be seen across fig. 4.12. When comparing the inner and outer sections of each sample, these lines appear to be emanating radially. These line features are also affected by the Ta seed layer. Their separation varies with the Ta seed thickness, a thicker layer resulting in closer lines. A separation of 6 $\mu$m and 4 $\mu$m are observed for a Ta seed layer thickness of 0.5 nm and 5 nm respectively.

The ease with which these features were highlighted shows the power of this comparative technique. Given the difference in separation of these lines based on the thickness of the Ta seed layer, it can be inferred that the sample with a thinner seed layer would offer less of these domain wall pinning sites. This would make the sample more suitable for applications involving domain wall motion. A more comprehensive study to optimise these parameters was beyond the scope of this project.

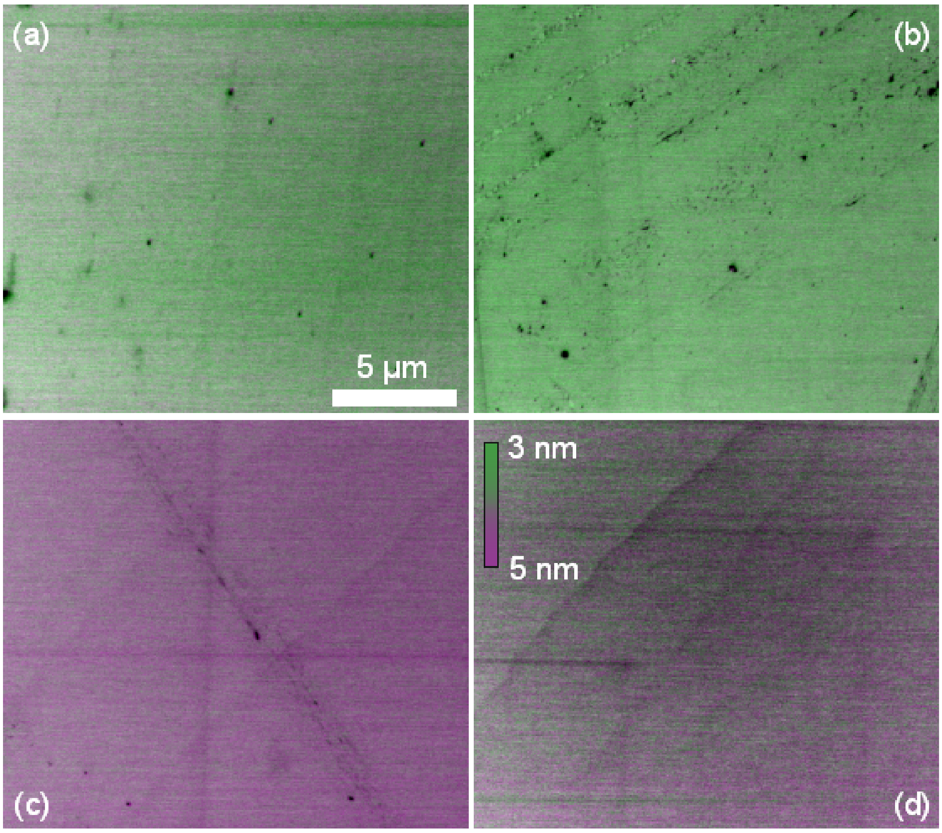

Figure 4.12: Example comparison images for samples a.1, b.2, c.3 and d.4. These focus on the CoFeB/MgO interface. The structure of these samples can be found in table 4.1.

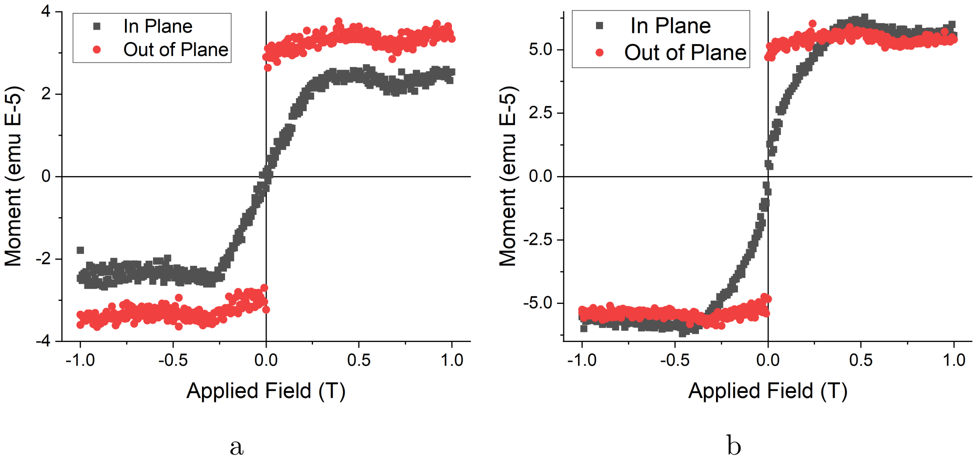

a b

Figure 4.13: Magnetisation curves measured under in-plane and out-of-plane magnetic fields for a. sample 3 and b. sample 4 in a thin film form.

Magnetic measurements, using a vibrating sample magnetometer (VSM), were performed in collaboration with this project to attempt to identify the physical effects of these observed features. The Microsense Model 10 VSM was the model used for these measurements. Whilst it has the capability to cool samples, in this case the measurements were all done at room temperature.

The Model 10 can apply a field of up to 2.2 T, in this case ±1 T was applied. The resultant VSM measurements taken can be seen in fig. 4.13. These results demonstrate an expected change in the value of $m_s$. In sample 3 the out-of-plane $m_s$ is higher than the in-plane value whereas this is not the case for sample 4. In sample 3 there is a stronger perpendicular magnetic anisotropy allowing it to achieve full magnetization reversal in the out-of-plane field but not in the in-plane field. On the other hand, sample 4 has smaller anisotropy, causing the shift under the in-plane field. It should be noted that the $m_s$ becomes the same under high magnetic fields. These measurements can be correlated to the frequency of the imaged line features. The shift in $m_s$ is due to an increase in the total volume of the weakly perpendicularly magnetised regions caused by surface roughness. Sample 4 shows both an increase in the number of features at the interface and shows more weakly magnetised regions caused by a local reduction in CoFeB due to surface roughness, providing a strong link between the observed features and the magnetic measurements.

The findings and correlations outlined confirm that this non-destructive imaging technique can be used to not only effectively identify surface features but also to support investigations into subsurface features. This has been confirmed using stacks with well-defined interfaces. The non-destructive nature of the technique allowed a comparison of the interfacial quality and the subsequent magnetic measurements. Using this data, inferences can be made to explain the the trends seen in the VSM measurements. This has demonstrated that the technique is useful for scientific investigation as well as its intended role in quality assurance.

## 4.3 Reproducibility Study

Due to the experimental nature of the development of this non-destructive imaging technique it is important to ensure the results are consistent and reproducible. There are two factors that need to be considered: the reproducibility of simulation data and the reproducibility of the sample imaging.

To ensure the reproducibility of the data two measurements were undertaken. First the reproducibility of individual simulations was tested by repeating a typical simulation multiple times. The test was done using the structure of sample one with an impact voltage of 1 kV using 500,000 electrons. After repeating it 5 times the distribution of maximum penetration depth for BSEs were compared. Given the number of electrons used for this Monte Carlo simulation there was very little deviation observed. The maximum deviation between points was measured as <1%. To test the reproducibility of the code used to identify the contribution of each layer to the BSE image at a set impact voltage it was also run 5 times. As the only point of variance in this code is the input this produced identical results. Therefore it is important to ensure a large number of electrons is used for all simulations. Beyond that there are no other constraints needed.

To test the reproducibility of the non-destructive imaging technique it was necessary to test the image comparison tools used. The ability to image at high quality in the same location is essential for reproducible results, but that is dependent on a number of factors, including user ability, so it will not be tested for explicitly. However the software that should take that input data can be rigorously tested. As described earlier, two programs were produced, a manual and automatic one. To test them a series of images, taken at both 0.1 and 0.4 keV, were processed. This series would produce 30 images in total. They were then reviewed identifying any mismatches. After the review the images were processed two more times. The results were checked for consistency. In the case of the manual processing the number of control points chosen was also varied. The number of control points chosen was 2, 4 and 8.

As mentioned earlier in section 4.1.2, the automatic method of image processing was not consistent having a successful alignment rate <50%. It also struggled with repeatability as it used an iterative, least squares fitting method, meaning variations in the starting condition led to a lack of convergence. It is worth noting that the series of images used had a low (<5) feature count. This means they were the hardest case for the automatic processing. Without a large (>12) number of features it is much harder for the convergence. However not being successful, even with the difficulty, ensured that this process was not used.

When looking at the manual processing the results varied greatly depending on the number of control points used. When using 2 control points there was a very low successful alignment rate of <10%. Whilst the points selected were aligned the extremities of the images were typical stretched or transformed inappropriately. Increasing the number of control points to 4 reduced these effects, giving a successful alignment rate of approximately 65%. However, in cases where there was not an even spread of features the result was misaligned, stopping the success rate being higher. Once the number of control points had increased to 8 poor alignment became unlikely, with a successful alignment rate of >95%. One benefit in all cases of the manual alignment was that a check is included as part of the process allowing poor matches to be dismissed at the point of processing. For manual processing a minimum of 6 control points were used to balance the processing time and accuracy.

During the testing of the repeatability of the manual processing it became apparent that it was almost impossible to align the images within ±3 pixels of the original position. This was largely because of the difficulty in selecting the same control point positions. However, when selecting a large number of control points the effect on the final fit was minimised, resulting in a difference of alignment <5%. Whilst not exact, this allowed an estimate of the error to be made whilst using manual processing. Due to this the error is alignment is taken as 5%.

These tests demonstrate the reproducibility of the technique being developed at all stages. In cases where they highlighted the inability to exactly replicate the data they provided an estimate of the error. Throughout all remaining studies these errors remain present and are considered during the analysis. In addition the confidence gained by these tests in the reproducibility of the results have also influenced the analysis.

## 4.4 Summary

With the starting point of a successful proof of principle, a non-destructive imaging technique has been formalised, tested and used to investigate typical samples. To formalise the technique a rigorous simulation procedure was developed, discussed earlier in section 3.2. In addition it was necessary to design and code a tool for image analysis. An automatic and manual method was produced in MATLAB, with the manual method proving to be more reliable after extensive testing.

Once these systems had been put in place it was possible to investigate a multilayer sample. In this case the samples were developed for use in domain wall motion studies. The structures are shown in table 4.1. During the investigation into these samples subsurface line features were found. These varied in frequency based on the thickness of the Ta seed layer, where thicker seed layers had more frequent line features. Magnetic measurements performed on the samples after imaging highlighted a correlation between the ability to switch between in- and out-of-plane magnetisation states and the frequency of these features. All these tests demonstrated that the thinner, 0.5 nm Ta seed layer would be better for domain wall applications as it resulted in less potential pinning sites.

This is most likely to be due to the roughness induced by the seed layer. A 0.5 nm Ta layer will have a uniform structure when compared with a 5 nm seed layer. This is because the thinner, 0.5 nm, seed layer is a couple of atoms thick. This both reduces the likelihood of stacking faults occurring and doesn't allow for a large variation in roughness. These benefits will have reduced the number of pinning sites within the layers above. It is worth noting that 0.5 nm may not be the optimum thickness, a more detailed study would be required to find that.

# Chapter 5

# Magnetic Tunnel Junction Based Devices

The technique has been developed to image sub-surface interfaces non-destructively and the data has been interpreted and corroborated, it is now possible to investigate samples with either interesting geometries or partially unknown structures. As one of the clearer applications for this technique is quality assurance in the silicon and device industry it was decided that investigating magnetic tunnel junction (MTJ) devices was the best next step. MTJ devices are of interest as read heads in hard drives and a key building block in the development of MRAM. MRAM is a variant of random-access memory offering similar speeds to the more traditional silicon dynamic random access memory (DRAM), whilst requiring less energy to run as it is non-volatile in nature. MTJs are also more tolerant to extreme environments than silicon chips making them suitable for use as low energy sensors.

The main draw back of MTJs is the complexity in both their stack structure and geometry. For this reason, providing a tool that can both ensure quality and feedback into production processes to increase yield is important to ensure that this technology is pursued further by industry. The following investigations all utilise non-destructive imaging, alongside more conventional techniques, to identify deposition defects and other possible structural features or defects.

## 5.1 Investigation into the CFMS/MgO/CoFe interfaces of an MTJ

A series of MTJ devices [71] with varying form factor, were produced from the same wafer with the multilayer structure shown in fig. 5.1. This multilayer wafer was deposited onto an MgO (001) substrate in an ultra-high vacuum (UHV) sputtering system in Tohoku University (ULVAC MPS series), running at 1 kV at room temperature. The only annealing that occurred was at 400C for 20 minutes immediately after the deposition of $Co_2Fe_{0.4}Mn_{0.6}Si$ (CFMS) to ensure the correct setting of the IrMn. Whilst this requirement makes it incompatible with CMOS production, recent studies have shown that similar texture can be induced in other materials with short relatively low temperature annealing [72].

This wafer was designed to maximise the tunnelling magnetoresistance (TMR) of the device. The structure and layers are as shown in fig. 5.1a. The bottom Cr layer acts as the bottom electrode for the device and the Pd layer above that ensures the correct texture is induced in the stack. The CFMS is the free layer, while the CoFe acts as the reference layer and the MgO is the tunnel barrier. The $IrMn_3$ provides the exchange bias [73] needed to fix the reference layer. The final layers act as a capping layer and the top electrode. The wafers were patterned into MTJs using photolithography. In this case approximately 1.4 $\mu$m of the carbonaceous photoresist AZ5214E was spin coated onto the wafer. The MTJs were patterned into devices with the dimensions shown in fig. 5.1b. These patterns were then milled using an Ar+ ion beam and the resist was removed using N-methylpyrrolidone. The devices were electronically isolated using UHV sputtered alumina. The top electrodes were then deposited by UHV sputtering with a similar pattern.

Once these devices were produced they were individually assessed using a four-terminal magnetoresistance measurement [74]. During these measurements a current of 100 $\mu$A was used. At the same time a field of ±40 mT was applied along the <110> direction of the CFMS layer. The magnetoresistance (MR) and resistance-area product (RA) were recorded. These measurements were done at room temperature. Based on these measurements, the devices could be split into two distinct groups: devices with a large TMR greater than 80% and devices with a small TMR less than 20%. A typical graph for

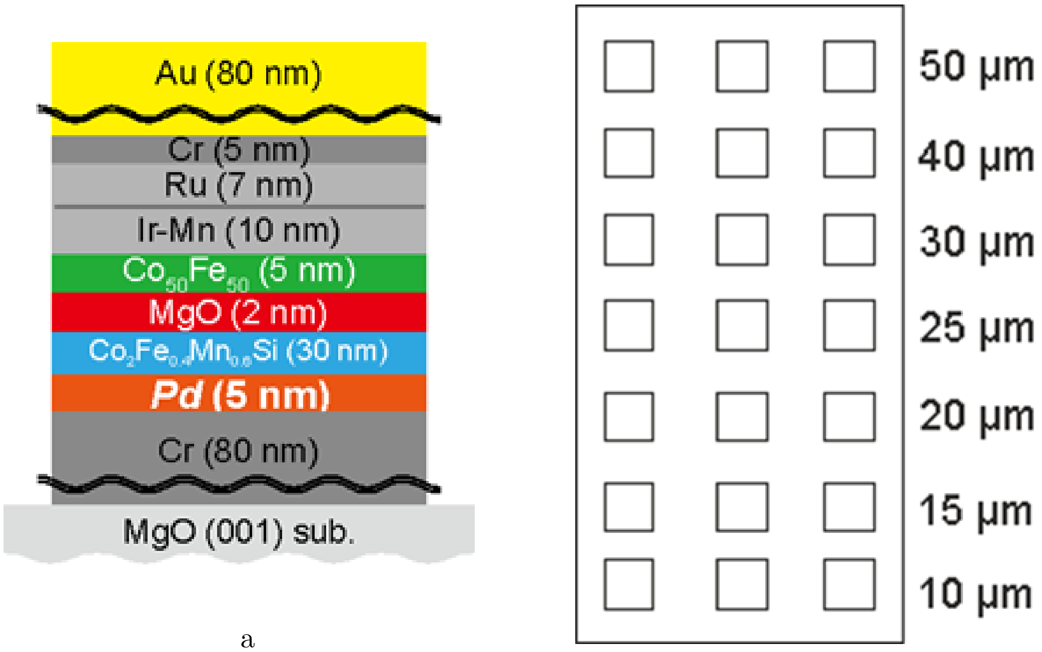

a

b

Figure 5.1: a. the deposited stack structure and b. the etched wafer pattern.

these groups is shown in fig. 5.2. The average RA for the two groups were $(3.5 \pm 0.6) \times 10^4$ and $(6 \pm 4) \times 10^3$ respectively. This is about an order of magnitude difference.

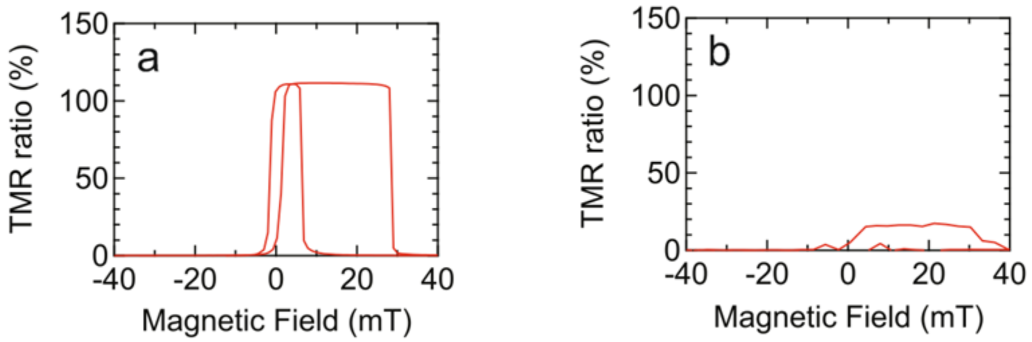

Figure 5.2: Typical TMR graphs for a. a high TMR device and b. a low TMR device.

As the aim was to produce devices with large TMR the devices with a small TMR are considered as failed. In this batch of devices the yield of large TMR devices was 69%. This investigation is aimed at identifying the differences between the devices with large and small TMR with the primary aim of improving the total yield. A quick review of the devices showed that their size had little bearing on the failure rate. In the case of MTJs the quality of the tunnel barrier and its interfaces has the dominant effect on the properties of the device. This is because any defects, such as pinholes, provide lower resistance pathways for the charge carriers, reducing the TMR and reducing the effectiveness of the device. Hence the non-destructive imaging technique was chosen as the primary investigative tool. It can gather information on the interface quality of all of the devices quickly with little sample preparation and leave open the possibility of further investigation.

### 5.1.1 2-D Simulations

Given the clearly defined structure of the wafer, simulations were performed in CASINO, as detailed in section 3.2, to identify the voltage range to use to probe the CFMS/MgO/CoFe interfaces. 2-D simulations were chosen over 3-D simulations as the dimensions, in x and y, of the MTJs are large. Whilst this means that there may be unexpected geometric effects at the edge, the fact that the insulator has as lower Z than the MTJ the effects of geometry should be minimal. The simulations were done in CASINO between 9 kV and 12 kV using the methodology discussed in chapter 3. This was done in 0.1 kV intervals and the data was used to produce fig. 5.3. Au has not been displayed in the graph, however it was included in the normalisation. Au consistently makes up more than 98% of the signal. This is due to the very thick layer of gold used as a capping layer/electrode, seen in fig. 5.1a.

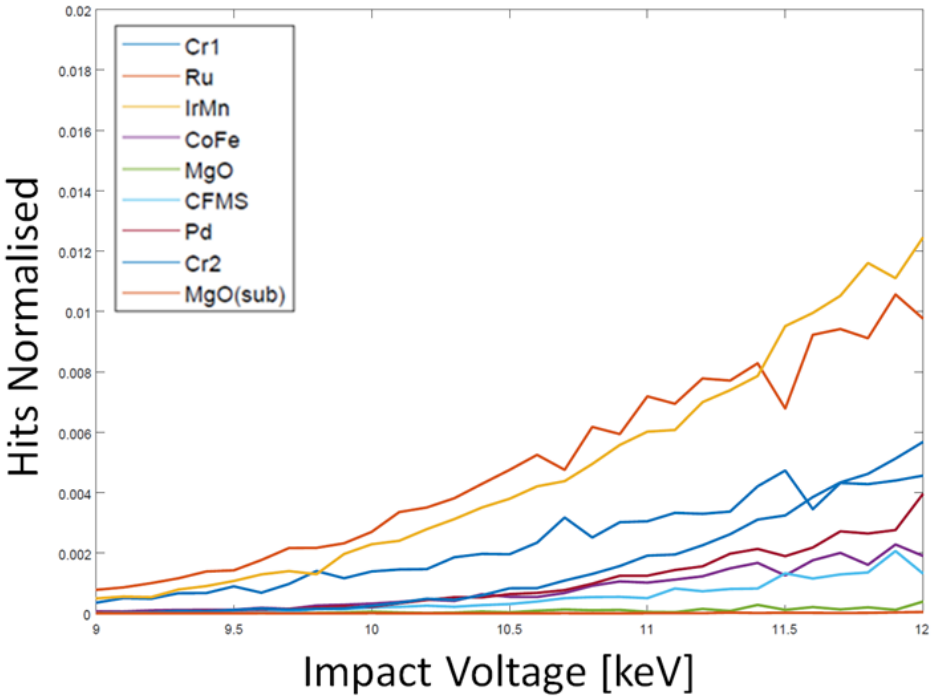

Figure 5.3: A graphical representation of the simulations performed in CASINO. These are normalised results, but Au is not displayed.

The criteria outlined in section 4.2.1 was utilised here. When looking at fig. 5.3, it can be seen that with a 9 kV electron beam almost 0.002% of the electrons penetrate into the bottom CFMS layer. 0.001% and 0.006% were able to penetrate the MgO and CoFe layers, respectively. A 12 kV electron beam was calculated to penetrate the CFMS, MgO and CoFe layers by 0.13%, 0.04% and 0.19%, respectively. These simulations showed a change of over 4000% in the penetration probabilities within the CFMS/MgO/CoFe junctions. To optimise the amount of information gathered at the interfaces of interest, voltages 10, 10.5 and 11 kV were chosen. These were checked in the SEM and provided a good balance between signal level and reduced over-penetration.

### 5.1.2 Investigative Details and Interpretation of Results

As the previous simulations had identified suitable voltages to use, an investigation was carried out systematically on all the devices on the wafer. To prepare the sample it was cleaned using a standard three wash procedure then mounted on to a stub using carbon tape. All devices on the wafer were sequentially imaged at 10 kV, before reimaging them at 10.5 kV then finally 11 kV. This was done to reduce the electron dose to the area of interest as it would only need to be focussed above a device once. This would reduce the amount of carbon fixation. The order low-high was chosen as this allows images which are more surface sensitive to be done at a point where there is less chance of a build up of carbon compounds. In this study the high voltages selected were due to the thick capping layer. Due to the voltages used the effect of the build up of carbon compounds would only have a minimal effect on the images.

Once collected these images were processed using the methods outlined previously in section 4.1. This was also done for all of the devices on the wafer and the resultant images were compared both within and between the large and small TMR devices. Examples of some of the resultant images from each group are shown in fig. 5.4.

The initial region of the stack that was examined was a comparison of the interface quality. In the case of these devices the focus is on the central region. In the case of both the devices exhibiting large and small TMR these regions were free from any noticeable features or contrast changes. This is apparent in all of the images in fig. 5.4. Any features that are identified as surface features

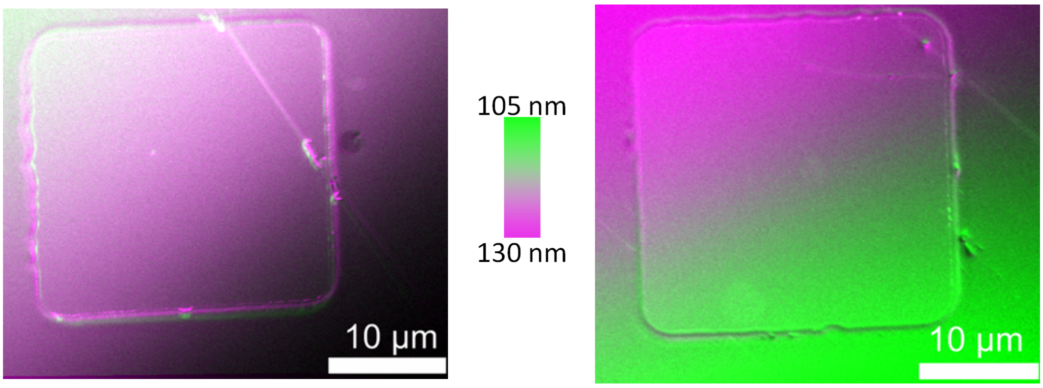

a

b

Figure 5.4: The composite subtraction images for a. a high TMR device and b. a low TMR device. An approximate depth scale has been added. This is for visualisation only.

by a comparison with a low voltage image can be neglected as they are likely to be surface contaminants. The lack of identifiable features led to the conclusion that, on the scale of the devices, the interface quality was good. It indicates that there are no major dislocations and that there was not any intermixing of layers during deposition or that the intermixing was entirely even. If there were such features it would be expected to find obvious contrast changes such as in fig. 4.3.

The next area of interest was the edge regions of the devices. This is an area where it could be reasonable to expect defects as it is the region most exposed to the rigours of lithography techniques. When looking at the images from devices exhibiting large TMR, such as in fig. 5.4a, the vertical edges of the devices seem uniform in thickness and are similar in intensity. It may be possible to make out a slight purple and green leading edge to each sidewall of the device, but that is probably caused by a slight misalignment. This is more clear as the patterns match the effects expected when one of the images has been shifted slightly.

However, when looking at the devices exhibiting small TMR this is not the case. The vertical edges of the devices are distorted. In fig. 5.4b it can be seen that there are slightly different thicknesses and the leading edges appear to change, indicating this is not entirely due to misalignment. Due to the material changes at the edge of the device, changing from the wafer structure to just alumina, it was not possible to isolate the layers or the materials that were responsible for these features. As such it was decided that a chemical investigation would assist in identifying what was causing this difference in edge conditions.

The method of chemical analysis chosen to clarify the differences in these edge conditions was EDX. This technique was chosen for a number of reasons: Firstly it is highly chemical sensitive as outlined in section 3.1.3; Secondly it is also spatially sensitive allowing chemical maps of the sample to be generated; Thirdly it is also a convenient and quick technique only requiring the preparation of a sample for SEM analysis and utilises similar acceleration voltages. Using EDX, a chemical map was taken of each device using an acceleration voltage of 10 kV. This voltage was chosen as it provides sufficient overvoltage for the light elements that are of primary interest. It also tightens the interaction volume significantly when compared with an analysis at 20 kV. The maps themselves were used to compare the distribution of the elements that were present not to quantify them. This method of comparison was chosen largely due to the complexity of the structure and the geometry of the devices. Figure 5.5 shows the EDX maps for a selection of elements taken from a large TMR device. All recorded elements are not shown as in some cases the counts were very low. The elements that are shown are those that are common throughout all the maps taken.

The maps shown in fig. 5.5 show the distribution of C, Ru, Au and Al and a corresponding SEM image to highlight their geographical importance. As can be seen the Al map shows concentrations that are entirely outside of the device. This is expected as Al is not present in the stack. Any small concentrations of Al seen inside the structure are probably misattributed from the Bremsstrahlung X-rays. Looking at Ru the opposite is seen, large concentrations are only found within the structure. Once again this is expected behaviour. Finally the Au and C are evenly distributed across the sample. With C, this is due to the fixation of carbon compounds across the sample which should provide a somewhat uniform coating of a couple of nm across the surface. The Au is a large contact so it would only be expected to vary if it was influenced by other large signals. For comparison, fig. 5.6 shows the EDX maps for a typical small TMR device.

Once again the maps in fig. 5.6 show the distribution of C, Ru, Au and Al, but this time they have been taken for a small TMR device.Looking first at the Al map in isolation, it appears that the Al is evenly distributed with the

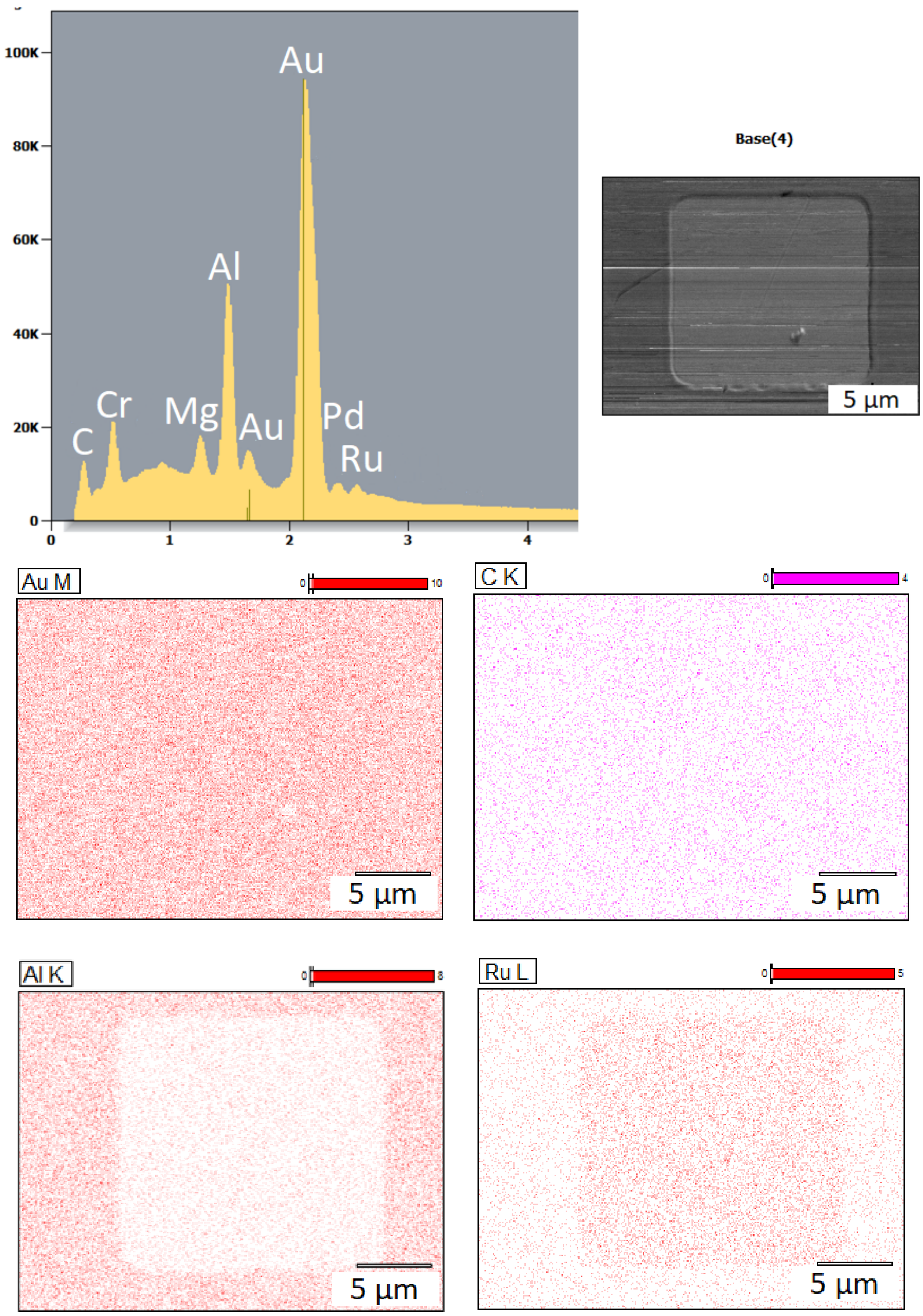

Figure 5.5: Representative energy-dispersive X-ray spectroscopy mapping of high TMR MTJ samples.

exception of a large concentration along the right edge of the pillar, indicated with an arrow. However this is not the case. When looking at the Au map in tandem it is clear that the area of a high concentration of Al is significantly more intense than other areas. This has caused the automatic scaling to distort the map poorly displaying the rest of the distribution. It was not possible to rescale the data as it was locked by the software. This phenomena was evident

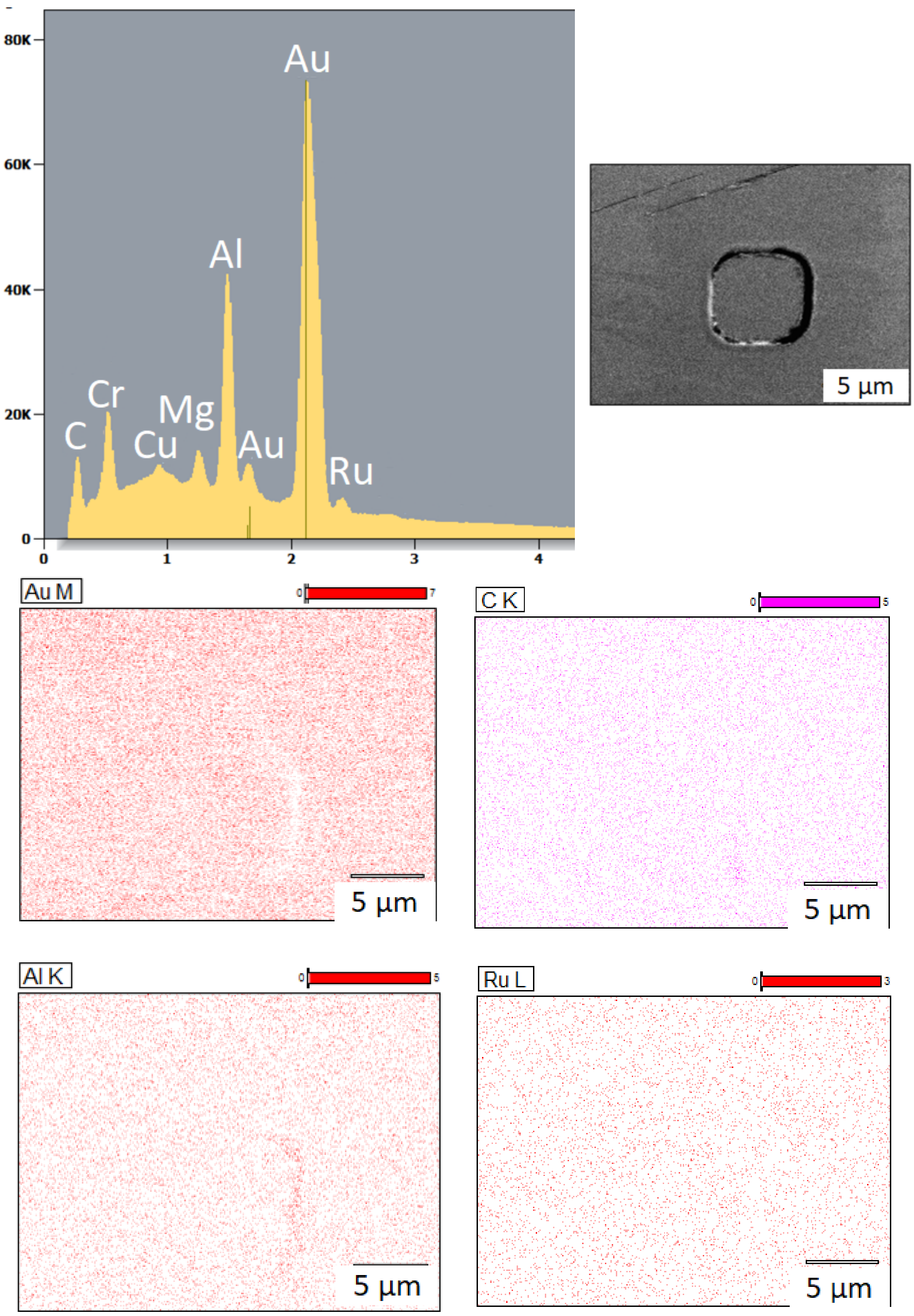

Figure 5.6: Representative energy-dispersive X-ray spectroscopy mapping of low TMR MTJ samples.

as the signal was such that it actually reduced the Au signal in the areas of high Al concentration. Apart from in these areas, the concentration of Au is uniform across the rest of the map.

Looking at the C map, once again it is uniform apart from in an area along the right edge of the device. This shows the opposite trend to the Au, the C signal is larger where the Al signal is present. Given the separation of the peaks it is probable that this is a real effect. With the C map it is essential to check the surface for contaminants first but the SEM image shows that the only feature present is the device itself. Finally looking at the Ru map an even distribution is seen. This is probably due to the poor deconvolution of the Au and Ru peaks by the software, possible attributed to the smaller size of this particular device. However it could also be due to a lower number of counts in the peaks of import.

Given the evidence gathered from the transport properties, the interface imaging and the EDX mapping a hypothesis was drawn up. As the small TMR devices consistently show a large concentration of both Al and C along an edge of the device this may be some sort of aluminium carbide formation during the alumina deposition. Using $Al_4C_3$ as an example of an aluminium carbide the resistivity of it and the tunnel barrier can be compared. $Al_4C_3$ has a reported resistivity of $10^2$ Ωcm, which is many order of magnitudes smaller than that of MgO, which is $10^{12}$ Ωcm. If this carbide were to straddle the tunnel barrier this would provide a much lower resistance pathway essentially shorting the device. This type of shunting could explain the low TMR and RA of the small TMR devices.

These sorts of carbides could be formed by an interaction between the deposited alumina and the photoresist used previously during the Ar+ ion milling step. This photoresist could be left behind after an incomplete removal during the N-methylpyrrolidone post milling. Once again using $Al_4C_3$ as an example, this carbide has been known to form by the reduction of alumina at around 2000 K [75][76]. Given the very high deposition voltage of 1 kV combined with the high incident current it is possible that very local areas may receive an energy equivalent to this heat. As there are a lot of factors which are uncertain, a simple test was put forward. If the deposition energy was reduced then it should be possible to reduce the amount of aluminium carbide formation increasing the yield of the devices.

### 5.1.3 Device Optimisation

Moving forward with this simple experiment the parameters of the deposition of the original batch needed to be identified. As discussed an acceleration voltage of 1 kV was used. A beam current of 50 mA was also maintained. This meant a deposition time of 47 minutes was required to isolate the devices with alumina. To reduce the overall power of the deposition for the suggested experimental run the beam current was reduced to 30 mA. This increased the deposition time to 87 minutes, but should have reduced the likelihood of aluminium carbide formation.

Once the devices had been fabricated transport measurements were performed. These measurements showed the opposite, the reduction in beam current had in fact reduced the yield of devices greatly, down to 12%. These results are shown in table 5.1. However this can be accounted for by the increase in time taken to deposit the alumina. The wafer stage did not have sufficient cooling to allow for such a prolonged run, so it was done in two stages. During this cooling off period between the two stages, a hardening of the photoresist occurred. This hardening increased the difficulty of the lift-off process such that the yield was greatly reduced.

| Device Group | 30 - $1^{st}$ | 30 - $2^{nd}$ | 5 - $1^{st}$ | 5 - $2^{nd}$ |
|---|---|---|---|---|
| Beam Current (mA) | 50 | 30 | 50 | 30 |
| Deposition time (mins) | 47 | 87 | 36 | 65 |
| Yield (%) | 69 | 12 | 21 | 36 |

Table 5.1: Yield of devices with MR $\geq$ 80%. The groups are listed based on their CFMS thickness, either 5 or 30 nm. All were deposited at 1000 V.

Evidently with the set-up used to produce these devices this is not a viable solution. However a similar set of devices were made with the main difference being a much thinner CFMS layer of 5 nm instead of 30 nm. This batch of devices reported a much lower yield of devices (21%) with $\leq$ 80% TMR. These samples were not studied using the suite of techniques previously described but they were produced in an identical manner. This meant that it was possible to test to see if changing the deposition conditions increased the yield as the thinner CFMS layer would allow the sputtering system to fully deposit the alumina without requiring a cooling off period.

Once this batch of devices was produced with a beam current of 30 mA the transport properties were measured. With these changes a yield of 36% was found, an increase of 15% over the previous batch. This is indicative that one of the issues with both sets of devices was the formation of compounds such as aluminium carbide along the edge of the devices, which allowed shunting to occur. Whilst it is clear that this is not the only issue that faces the production of these devices, it was a strong improvement capable of proving the concept of the use of the non-destructive imaging technique as part of a suite of quality assurance (QA) tools.

It was not possible to make modifications to the UHV sputtering system as it belonged to a multi-user facility. If the cooling could be improved it would allow the suggested improvement to be tested with the original device structure. Whilst it would have been possible to perform more imaging and investigate the devices further to continually improve their yield, proving the concept of the non-destructive imaging technique as a QA tool was sufficient for this project.

## 5.2 Production Quality MTJs

An industrial collaborator, IMEC, kindly provided two sets of wafers of MTJ devices for study. One had a structure similar to fig. 5.7a and the other had a structure similar to the one shown in fig. 5.7b. The layer of interest, the bottom MgO layer, is also highlighted in these figures. As can be seen this is a complex structure, designed to both maximise the magnetic properties and stabilise the device whilst maintaining a footprint of 100 nm. All of these MTJs were encapsulated in approximately 20 nm of $Si_3N_4$ to protect the sample from oxidation. None of the devices were wired, but were produced in a production quantity as shown in fig. 5.7c.

These devices were provided to test the output of the non-destructive imaging technique and assess its usefulness as a QA technique and research tool. They were also provided as the two samples were showing different properties, that cannot be reported and the collaborators were interested in what additional information could be provided. Whilst there should not be an issue with following the standard operation outlined earlier these devices are very narrow and tall so they will provide a good test of the resolution that this technique can achieve.

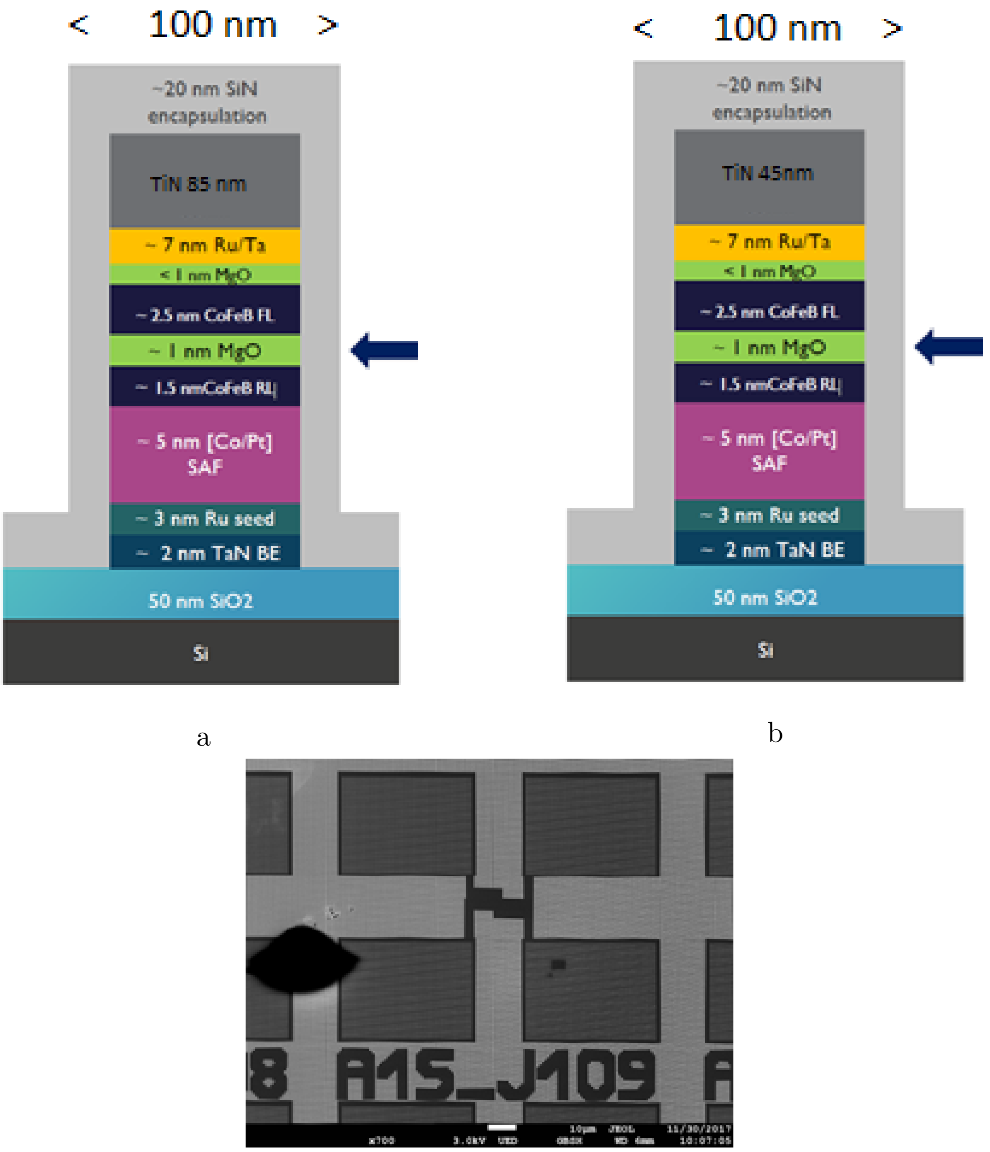

a

b

c

Figure 5.7: Production quality MTJs. Figures a. and b. show the structures for Pillars 1 and 2 respectively. c. shows the overall patterning.

### 5.2.1 Sample Simulations

Simulations of the sample were carried out with CASINO as outlined in section 3.2. The sample details shown in fig. 5.7a and fig. 5.7b were used and the resulting graphs were produced, shown in fig. 5.8. As can be seen images taken with an acceleration voltage of 3 and 3.5 kV were chosen to provide interfacial information on the MgO layer highlighted earlier in fig. 5.7a and fig. 5.7b.

The criteria outlined in section 4.2.1 was utilised here. During these simu-

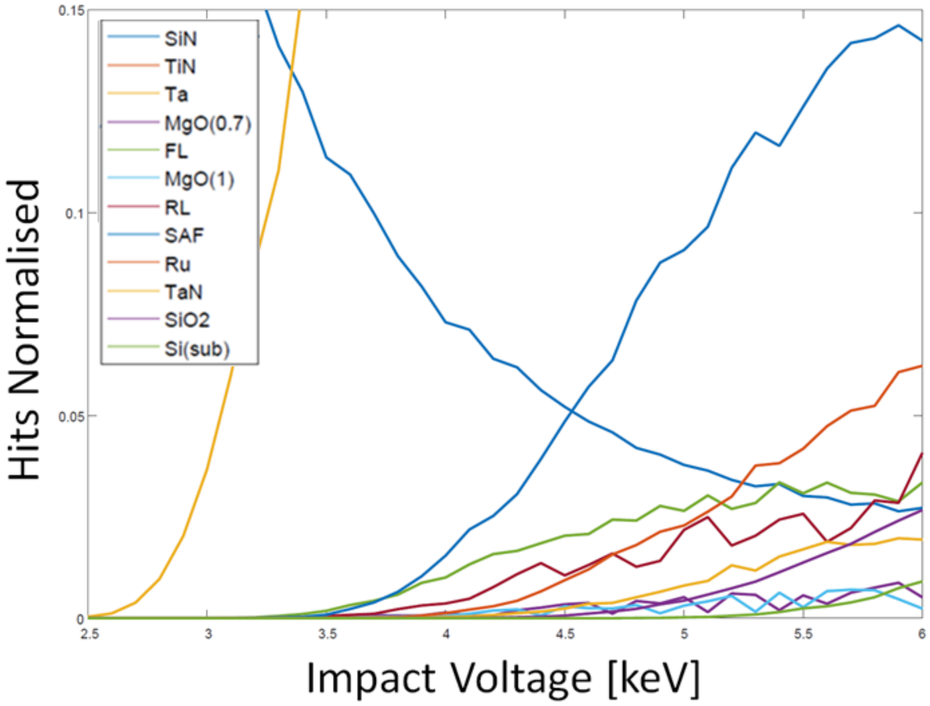

Figure 5.8: A graphical representation of electron simulations for production quality MTJs.

lations and the initial imaging geometric effects were not considered. However given the dimensions of the MTJ at 100 nm, a large number of points are going to have interaction volumes which will extend beyond the actual pillar. Therefore it may be important to consider the effect this may have. To try and gain an understanding of this further simulations were performed using the 3-D version of CASINO. The differences between the two versions have been discussed in section 3.2. The resulting simulations are shown in fig. 5.8.

As can be seen in fig. 5.9 a number of electrons escape the pillar although most would not return to influence the image due to the large deviation they take. However as the edge of the pillar is approached this escape frequency will increase, possibly causing the signal to decrease. Another effect to consider is the probability of strong SE emission from the $Si_3N_4$. This will make the $Si_3N_4$ much brighter, particularly the large deposits around the edge. If the detector is not filtered correctly this will have an effect on the regions immediately around these edges.

Included alongside the simulated electron pathways is an energy scan. This is an instantaneous representation of the distribution of the electron density, where white represents a high density and black represents no density. These

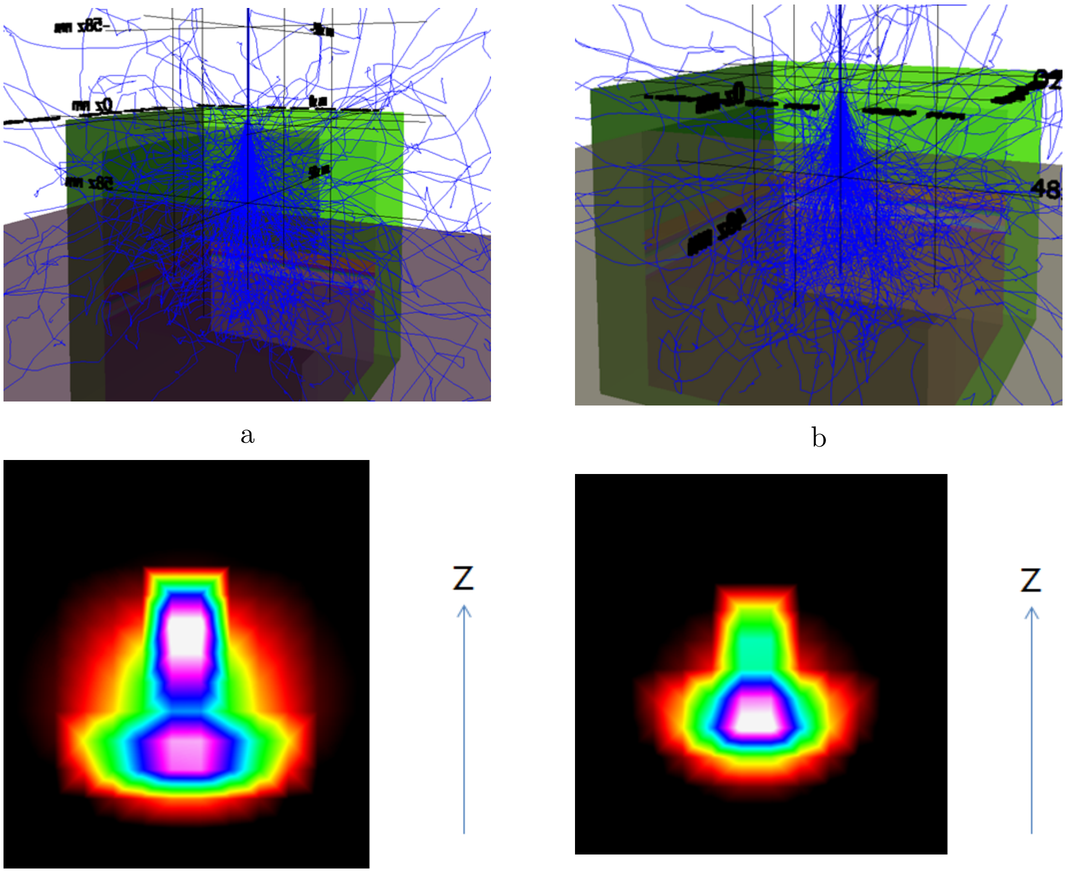

a

b

c

d

Figure 5.9: 3D electron simulations performed using CASINO v3.3 at 3.5 keV for a. Pillar 1, the 85 nm etch and b. Pillar 2, the 45 nm etch. Energy scans were also created for c. Pillar 1, the 85 nm etch and d. Pillar 2, the 45 nm etch.

scans were simulated using an acceleration voltage of 3.5 kV. These show starkly different distributions. In the case of Pillar 2, the 45 nm etch, there is one large concentration of electrons spreading from the bottom layer to the substrate. This probably represents electrons which have reached the substrate and proceeded to interact with the sample until they had spent their energy. These are unlikely to contribute to anything but an X-ray spectrum.

However, in the case of Pillar 1, the 85 nm etch, there are two large concentrations of electrons. The less intense concentration is similar to Pillar 2 an area starting in the bottom layer and extending into the substrate. However the more intense area is quite different. This area is focussed within the stack structure. This means that there are an abundance of electrons interacting in the main structure which will produce secondary products, specifically BSEs, which are going to influence any images gathered. This is probably a result of the confines of the long narrow geometry. Whilst the sidewalls of the structure allows electrons to escape it can also act to reflect electrons back inside allowing further interactions to occur.

### 5.2.2 Imaging and Interpretation

With the voltages indicated by the simulations imaging was carried out on the devices. Due to both the size and the number of devices imaging was carried out at several different magnifications to test the clarity and resolution. Examples of these images are shown in fig. 5.10. These magnifications were used at both of the voltages and for both sets of samples.

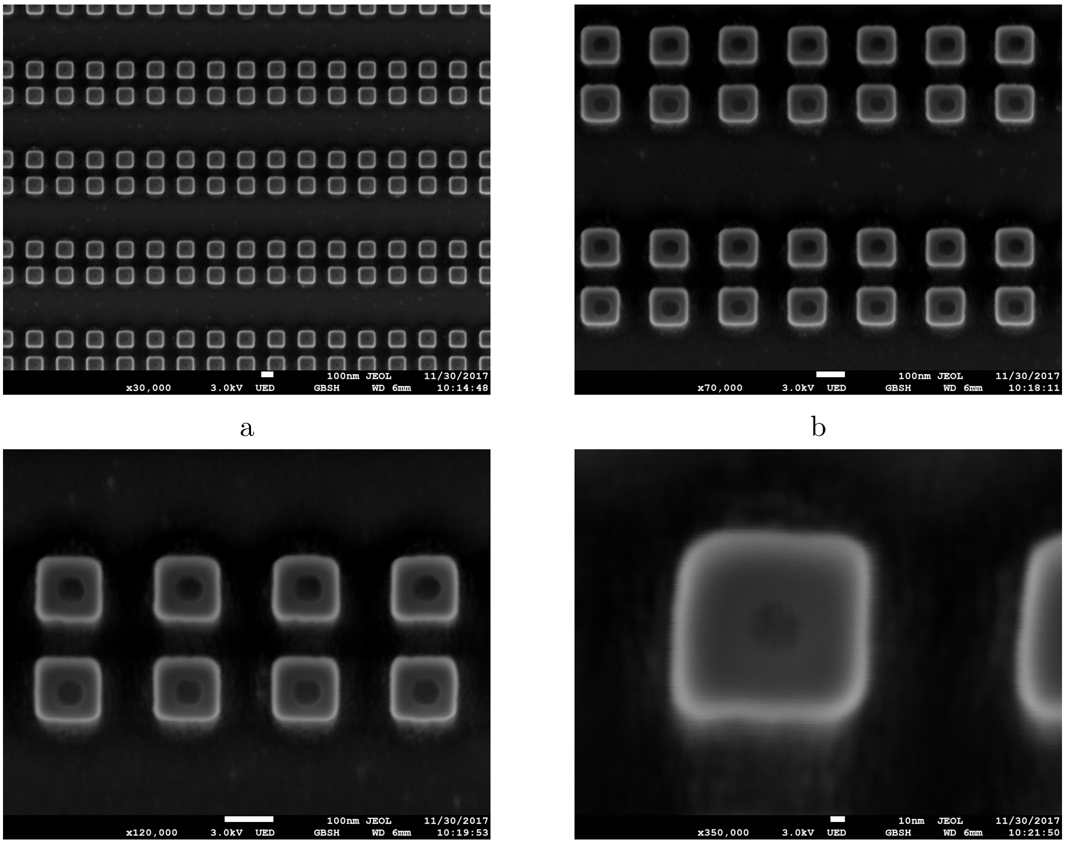

a

b

c

d

Figure 5.10: BSE images taken at 3 kV using the GBSH imaging mode. All devices are 100 X 100 nm. The magnifications used were a. 30000X, b. 70000X, c, 120000X and d. 350000X

During the imaging performed at high magnification difficulties, largely associated with drift, were encountered. This made attaining focus difficult and also distorted the apparent shape of the devices. However the key features visible in the images taken at lower magnification, which experienced less distortion, were still visible. These features were a bright ring surrounding the pillar and a circular feature in the centre of the device. These features were consistent across both sets of devices, although the size of the circular feature changed between Pillar 1 and Pillar 2.

Once imaging was completed the composite subtraction images were created using the standard method. When looking at fig. 5.11a it can be seen just how consistent in shape the devices are. It is possible to see this from the SEM image but using the non-destructive subsurface imaging technique it can be seen that the device is regular both in shape and along its height. Any irregularities in the image, particularly around the edges, would show that the device is non-uniform across the height.

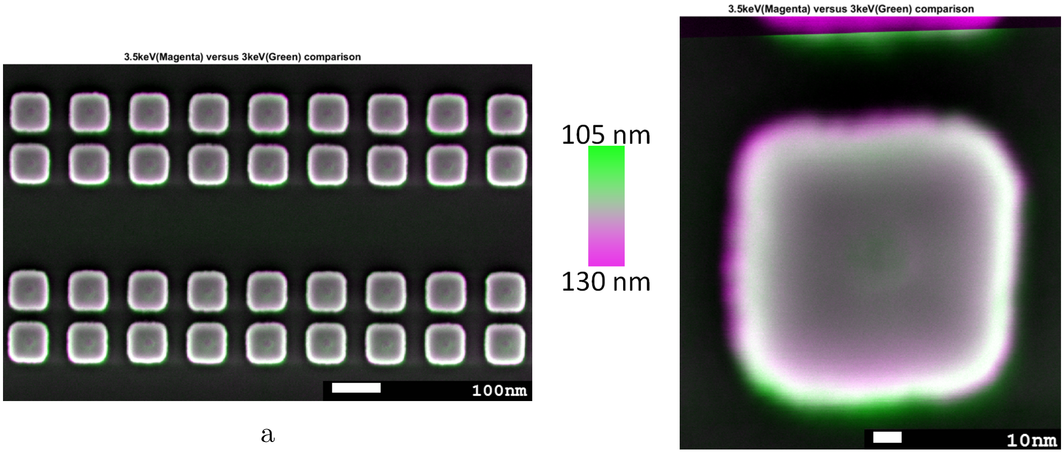

a

b

Figure 5.11: Composite subtraction images demonstrating a. the consistency of the MTJs and b. the $Si_3N_4$ encapsulation of an MTJ.

The bright ring surrounding the devices, seen in all figures, is due to the $Si_3N_4$ encapsulating the material. This appears bright due to the reason explained in section 3.1.1. The insulating material produces significantly more SE than the surrounding material and this affects the brightness. When the device is magnified further, such as in fig. 5.11b, this band is very clearly identifiable and separate from the main stack structure of the pillar. Interestingly any small deviations in the regularity of the devices are seen primarily in the encapsulating material. Images taken at higher magnification show that the stack structure has a regular defined shape.

The second pronounced feature is the circular feature at the core of the pillar. This core can be clearly seen in both etches in both SEM and composite images. An example of these cores are shown for each set of devices in fig. 5.12.

The cores are also quite a regular feature having an average diameter of (53±3) nm for Pillar 1 and (33±4) nm for Pillar 2. This average was measured across all the devices imaged at 120000X magnification. This magnification was chosen to reduce the possible influence of drift based distortions.

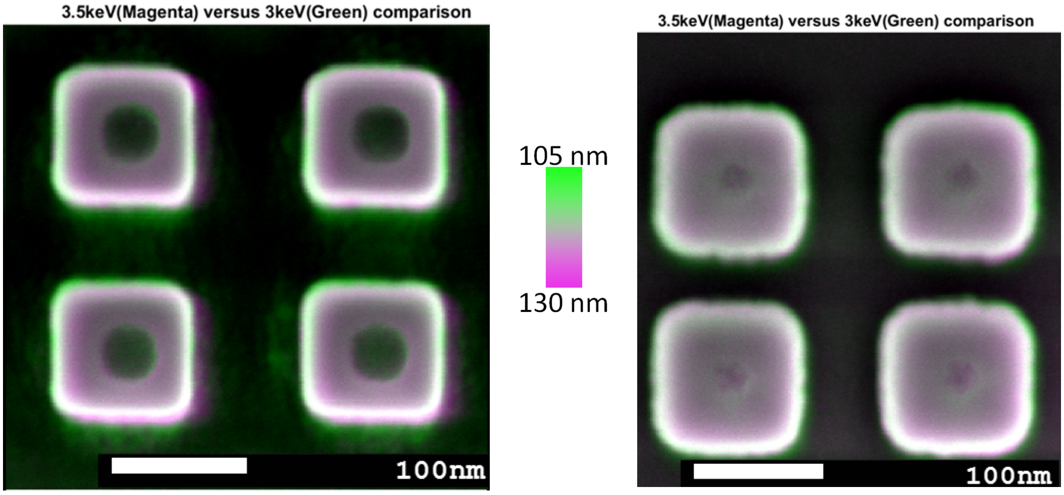

a

b

Figure 5.12: Composite subtraction images highlighing cores found in both sets of devices. The images show a. the core for Pillar 1, the 85 nm etch, with an average diameter of (53±3) nm and b. the core for Pillar 2, the 45 nm etch with an average diameter of (33±4) nm.

Based on both the simulations and the images in both fig. 5.11 and fig. 5.12 the origin of this core can be inferred. Referring back to the energy scan discussion that is a stark difference in the density of interacting electrons in the main stack. This hot spot seen in Pillar 1, could be responsible for the circle, as it is an area which would be producing the largest signal. However in the SEM images this area appears darker than the rest of the surrounding device. It is possible that the interaction products are released preferentially off axis but that is unlikely based on previous discussions on the way electrons interact. The darkness indicates that there is either a large amount of material which has a small BSE scattering cross section, or there is a geometric reason for a preference for off-axis scattering.

When considering the composite subtraction images this adds credence to the concept that this is probably a geometric effect. The image shown in fig. 5.12a highlights the circle in green. This indicates that the core has a stronger signal at a lower voltage. This is probably due to some sort of curvature leading to the tip of the device. A curved pillar is quite common in several different designs of MRAM, but we were unable to confirm whether this is the case here with the industrial collaborator. The image in fig. 5.12b also has a similar clarity of contrast, although it is much smaller. This could indicate that the tip of Pillar 2 is narrower than the tip in Pillar 1.

EDX was performed on the devices to attempt to identify the contributing materials to these features. There were many issues with this analysis. The drift seen whilst gathering spectra proved too large to gather any meaningful data. This was, in a large part, due to the need for much longer beam exposure time. This was required to ensure enough data was gathered, to resolve the materials that make up such a complex stack structure. Additionally the small size of the devices combined with the 10 kV acceleration voltage required to identify the relevant elements, meant that the signal from the silicon wafer they were mounted on dominated the spectra. This was particularly frustrating as the distribution of the $Si_3N_4$ was of particular interest. For these reasons the analysis was discontinued.

In summary the non-destructive imaging technique, alongside the SEM images that are used to realise it, have managed to analyse a large number of production quality devices. This analysis has confirmed the regularity of the structure and the dimensions of both the pillar and the $Si_3N_4$ used to encapsulate it. Due to the presence of the core feature the interfacial quality was not able to be studied. However the technique did manage to highlight the size of the tip of the core and from that the curvature could be identified.

## 5.3 Combining TEM and SEM analysis to investigate MTJs

An investigation into the use of both CFMS and MnGa in MTJs was ongoing at Tohoku University [77]. A big limiting factor in the success of these devices was interface quality and the crystallinity of the MgO tunnel barrier. Several versions of these devices were produced specifically to be investigated using both the non-destructive imaging technique and cross-sectional TEM analysis. These samples are shown in fig. 5.13. This provided a good opportunity to both assist in improving the yield and quality of the devices and to compare the information gathered by these two complementary techniques.

The first sample was produced as a continuous thin film, fig. 5.13a, whilst

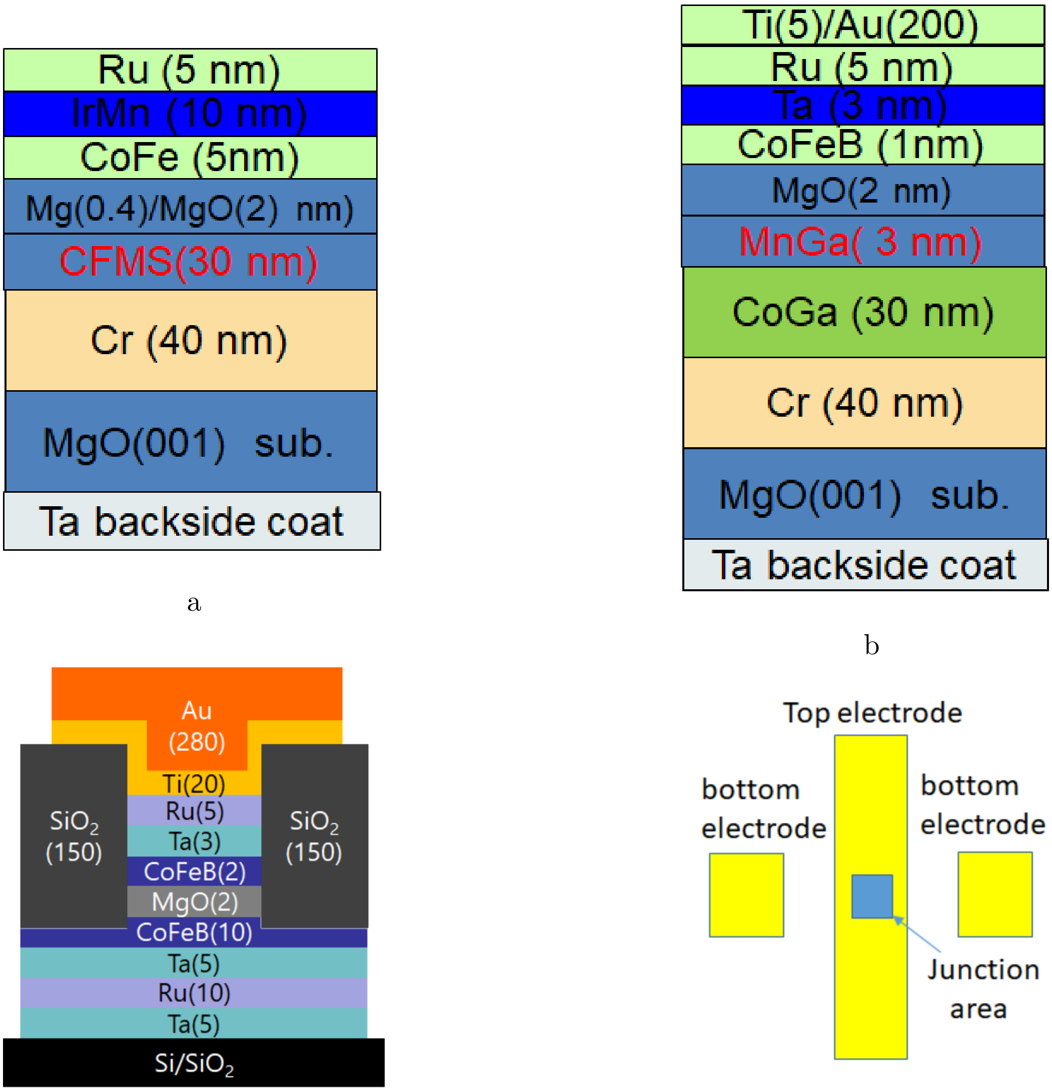

a

b

c

d

Figure 5.13: The wafer structures produced for a. TEM analysis and b. and c. SEM analysis, thickness is in nm. The SEM samples were patterned into devices in an array. They were produced as 10X10, 20X20 and 30X30 $\mu$m size pillars on the same wafer. All junctions had the structure shown in d.

the remaining two, fig. 5.13b and fig. 5.13c, were patterned into junctions using photolithography and Ar-ion milling as shown in fig. 5.13d. They were produced as 10X10, 20X20 and 30X30 $\mu$m size pillars on the same wafer. These samples were isolated using $SiO_2$. The aim of the research by these collaborators is to improve the TMR of these types of devices as they have potential to be room temperature MRAM cells. Some of the primary contributions to the TMR is the lattice miss-match and the interfacial roughness [78], these features were the primary focus of this study.

The continuous thin film was used to prepare lamellae suitable for cross-section TEM. Lamellae were prepared using both mechanical polishing and FIB and both were utilised during TEM analysis. These two methods were used to prepare a sample due to their contrasting benefits. Lamellae prepared by mechanical polishing provide significantly more surface area to image, but lamellae prepared by FIB are typically thinner providing greater resolution and clarity.

The two sets of patterned samples were prepared for SEM imaging with a simple wash and were mounted on to a stub. The first set of devices had been partially measured to identify its RA and TMR and the second set had been completely measured similarly. The measurements were performed using the same standard four-terminal measurement. The TMR values were not supplied by the collaborator, however the second set of samples had a yield of 19.4% of devices with $> 80\%$ TMR. The average RA measurement for a successful sample was $(8\pm1)\times10^4$ $\Omega\text{mm}^2$. The average RA measurement for a failed sample was $(4\pm2)\times10^3$ $\Omega\text{mm}^2$.

### 5.3.1 Simulations of Patterned Samples

Due to the large size of the patterned devices only 2-D simulations were employed to estimate the acceleration voltages that were to be used. These simulations can be seen in fig. 5.14. Due to the very thick Au electrodes, 200 and 280 nm respectively, the voltage required was very high, >18 kV. However this voltage is still within the operating range of the SEM but it did mean that gentle beam super high resolution (GBSH) could not be used during this analysis as with the other investigations. However given the high voltages that were required, the effects of the loss of GBSH would be minimal.

### 5.3.2 SEM Imaging

The criteria outlined in section 4.2.1 was utilised here. Once the voltages had been determined through the use of simulations imaging of the junction area took place and is shown in fig. 5.14. The voltages used initially were 20 kV and 18.3 kV. Once images were collected they were processed to produce composite subtraction images. An example is shown in fig. 5.15. As can be seen there is no contrast visible and the subtraction image looks almost identical to the SEM image. Closer inspection of the subtraction image did reveal that there had been a lot of redeposition around the edges of the pillar and that

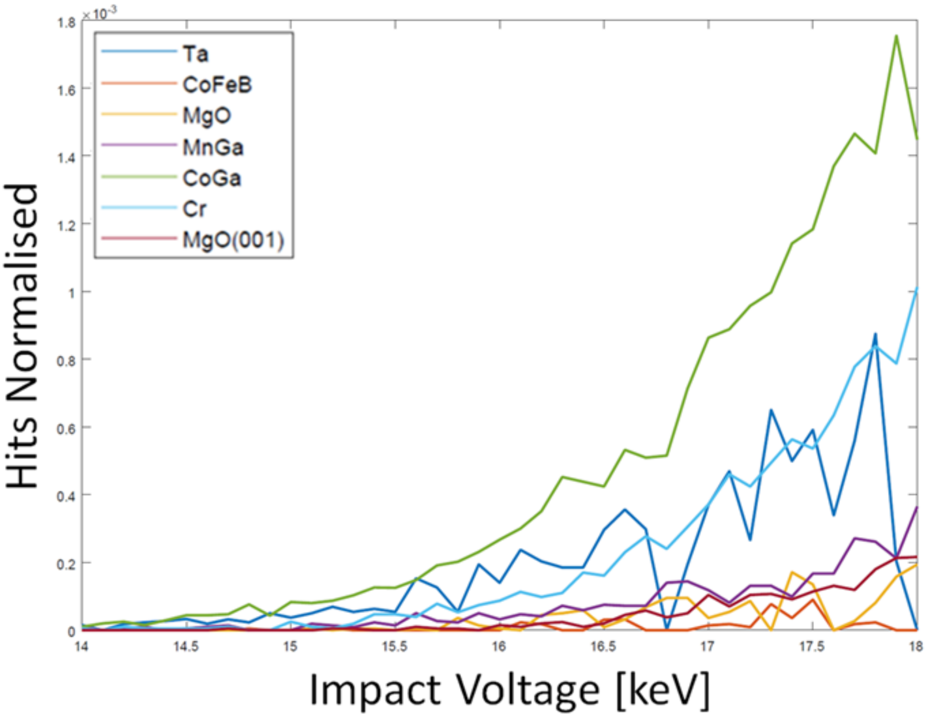

Figure 5.14: A graphical representation of the electron scattering data produced for these samples.

the surface was very rough. Cleaning the sample extensively had very little impact on the quality of the surface. Given these conditions it was presumed that a capping layer of a thickness >150 nm, alongside such a poor quality surface, was too challenging to image.

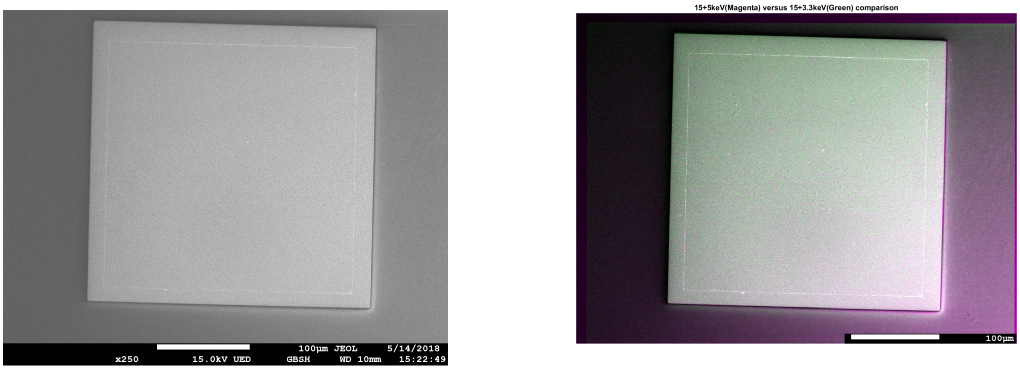

a

b

Figure 5.15: Initial SEM imaging of the devices. a. is the BSE image taken at 18.3 kV and b. is the composite subtraction image. A colour bar has not been included as the thickness of the Au capping layer has distorted the images. This means it would not be a useful gauge.

To resolve this there were two possibilities, produce devices with thinner capping layers similar to those documented in section 5.1, or reduce the thickness of the Au layer manually. In order to test the limits of this technique it was decided to reduce the Au thickness manually to determine the maximum that can be used.

Several methods were available to reduce the thickness of the Au capping layer in a controllable manner. These were: mechanical polishing, acid etching, FIB removal and plasma etching. Mechanical polishing was discounted as lapping pads have coarse grains, typically >100 nm. Similarly acid etching was discounted as it would be difficult to control and would require hot Aqua Regia. This left both the plasma and the FIB as options.

Plasma removal was trialled first using a sputtering device and placing the sample in the target position. Trial wafers were created to test the rate of removal. These samples were thick deposits of Cu on quartz. Cu was chosen as it was readily available and the difference in atomic number could be accounted for when finding the removal rate of Au. To measure the thickness of the Cu layer XRR was used. XRR measures the intensity of a beam of X-rays that have been reflected off the flat surface of a sample, across a range of incident angles [79]. Changes in intensity correspond to the density of the sample which in turn can be fitted to identify the thickness of the samples layers. Once the initial thicknesses had been identified the sample was exposed to the plasma for 30 seconds then repeated. The average removal rate was found to be 2.4 nm/s.

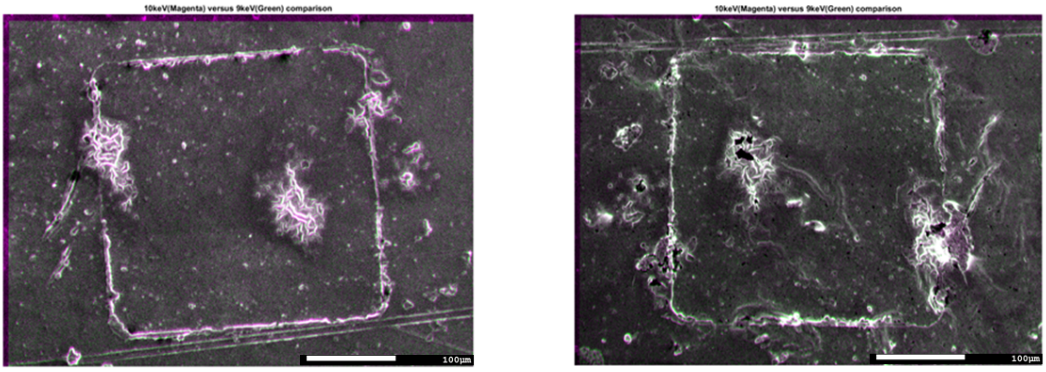

a

b

Figure 5.16: Composite subtraction images taken a. before and b. after the attempted removal/reduction of the Au layer. A colour bar has not been included as the thickness of the Au capping layer has distorted the images. This means it would not be a useful gauge.

With a calibrated removal rate the devices were exposed to the plasma for

60 seconds. This was intended to remove 140 nm of the Au capping layer. It was not possible to test the change in thickness using XRR as the devices were too small. Imaging of the sample was done at 9 and 10 kV to match images of the devices taken before undergoing the plasma treatment. These images are shown in fig. 5.16a. As can be seen in the original image in fig. 5.16a the sample surface contained a lot of redeposited material, particularly around the pillar. The small amount of contrast highlighted by the subtractive imaging was due to surface related material, such as redeposited Au or carbon deposits.

The image taken after the plasma removal, fig. 5.16b shows that there is even more redeposition and there are dark patches on the surface. These may be holes that were punched into the sample or large deposits of carbonaceous material that built up following the plasma treatment. Despite these artefacts it is clear that the treatment had an effect on the thickness of the surface. This is evident in the increase of contrast seen in the subtraction image. This contrast is probably related to the surface topography as it stems from the lower voltage image. This change in the surface shows that a significant amount of material must have been removed, approximately 100 nm.

Without an approximate knowledge of the thickness of the capping layer and a more polished surface, these devices will yield little information. Evidently the technique relies on knowledge of the structure to interpret the data. To be able to complete this study it would be necessary to reproduce the devices and greatly reduce the thickness of the Au capping layer. This would allow the interfaces of interest to be probed at a more typical voltage. However this study did manage to highlight the limits of this technique when resolving thin layers of light element layers below thick layers of heavy elements.

### 5.3.3 TEM Analysis

The TEM analysis was focussed both on the interface quality, specifically the dislocation frequency and the crystallinity of the MgO. After the cross section TEM samples were prepared and mounted on a grid they were imaged at 200 kV. A double tilt holder was used to allow two axes of rotation. This allowed an orthonormal alignment to be achieved. Images were taken focusing on the interfaces on either side of the CFMS. An example is shown in fig. 5.17a. The interface roughness was investigated and the frequency of dislocations estimated. This is important as this has a direct link to the TMR of a device.

The more frequent dislocations the lower the TMR. An example of the data obtained is shown in fig. 5.17b.

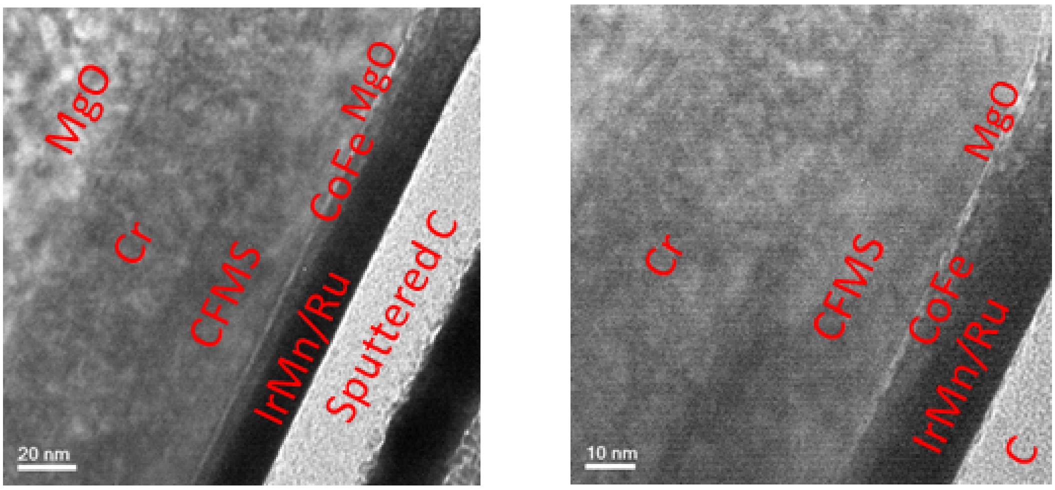

a

b

Figure 5.17: TEM analysis on the thin film wafer. a. is a representative image and b. highlights the interface more.

Using the images gathered from all the samples an attempt to measure the interfacial roughness was made. This was done by measuring the deviation of the light to dark transition point along the interface using a program written in MATLAB. This measure in pixel variation was then compared with the length of the scale bar in pixels to convert it to a measure in nm. This gave a roughness of (0.2±0.1) nm for the Cr/CFMS interface and (0.3±0.2) nm for the CFMS/MgO interface. The number of visible dislocations across the images interface were counted and divided by the total length of interface. This gave an estimate of one dislocation every (1.8±0.4) nm.

To evaluate the crystallinity of the MgO in the samples the ideal method is to use selected area diffraction. This allows the diffraction pattern of whatever is in the field of view to be gathered without the presence of the rest of the sample. As the MgO is only 2 nm thick it was not possible to select just this layer with the available apertures. Any attempt to gather the diffraction pattern of the MgO in isolation was thwarted by the strong patterns of the surrounding material. This means an evaluation of the crystallinity of the MgO was not possible. Using a higher resolution TEM might make it possible, but that is beyond the scope of this study.

In regards to the TEM analysis, whilst the methodology for finding the interfacial roughness and frequency of dislocations is sound they do not mean anything when there is nothing with which to compare them. This means that in the future more samples should be measured in similar ways, particularly patterned and electrically characterised devices, as this allows the TMR to be linked more decisively to these values.

## 5.4 Summary

The studies into MTJ devices have revealed many strengths and some weaknesses regarding this technique. The ability to image sub-surface interfaces even beneath a capping layer was championed in the first study [71]. This was shown to have limitations in this work. However the ability to use this non-destructive imaging technique alongside other microanalysis techniques was proven multiple times. Used alongside EDX a full structural and chemical evaluation of multiple MTJ junctions was performed. The quality of the patterning and deposition of many MTJs was assessed with no damage to the devices [80]. It was also possible to make estimates of the curvature of the top of the devices. A study also demonstrated the necessity of prior knowledge of the thickness of the sample. At the moment the technique is unable to be used to estimate sample or layer thicknesses.

# Chapter 6

# Organic Magnetic Tunnel Junctions

The integration of organic materials into electronic devices has been a major research topic since the discovery of graphene [81]. This has been driven by the array of properties different organics can offer and their low cost. In this particular study an external collaborator in Osaka University was exploring the use of an organic molecule, Cobalt(II) Phthalocyanine (CoPc), as part of the tunnel barrier in an MTJ device. These molecules, shown in fig. 6.1a, are used primarily due to their ability to self-assemble into 2-D constructs such as wires and monolayer films [82].

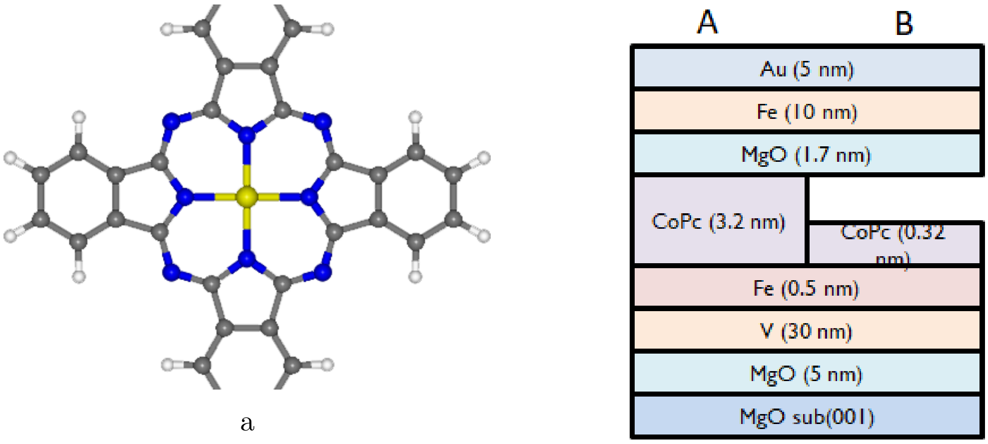

a

b

Figure 6.1: a. the Cobalt(II) Phthalocyanine molecule. Hydrogen is white, Carbon is grey, Nitrogen is blue and the Cobalt is Yellow. b. the stack structure. The two structures were deposited on the same wafer side by side creating two 10 mm X 20 mm samples.

Two similar stack structures were produced on one MgO substrate, as shown in fig. 6.1b. These were deposited using a molecular beam epitaxy (MBE) system in Osaka University. The 0.32 nm layer of CoPc, deposited on half the sample, corresponds to one monolayer. The MgO tunnel barrier had its thickness calibrated using reflection high energy electron diffraction (RHEED) oscillations. This technique is used consistently in MBE to measure the surface structure and layer thickness in real time [83].

These were designed to test the condition of both the CoPc and MgO after deposition. The non-destructive imaging technique was chosen to lead this investigation as there was an expectation to have macro-trends in the structures which may be missed in conventional TEM analysis. To highlight this and observe the crystallinity and interfacial roughness of these samples it was decided that cross section TEM should be performed alongside the non-destructive imaging.

The wafer was cleaved horizontally into two pieces which each contained both of the stack structures. One half was used for SEM imaging meaning it was mounted to a stub using carbon tape. The other half was retained to prepare TEM samples. It was not possible to prepare the cross section samples using mechanical polishing. This was due to the fact that the chemicals used to wash the sample throughout the process would react strongly with the CoPc. Whilst the same chemicals are used to clean samples for SEM, due to the much larger size and the protection of the capping layers they should have little effect. For this reason samples were prepared for cross section TEM analysis using FIB. This meant no chemicals were needed to clean the sample during the preparation.

## 6.1 2-D Simulations

Using the structures shown in fig. 6.1b simulations were performed in CASINO to find the acceleration voltages to study MgO and CoPc layers. The simulations were done in 0.1 kV intervals between 0.1 and 5 kV. The resultant graphs are shown in fig. 6.2. The criteria outlined in section 4.2.1 was utilised here. The voltages that were chosen to image both sides of the sample were 2, 2.2 and 2.4 kV. The reason the same voltages were being used for both sides was that C, which makes up most of CoPc, has a low interaction cross section meaning it does not interact strongly. Using the same voltages also made exploring the interfacial region, where the two regimes meet, a little easier.

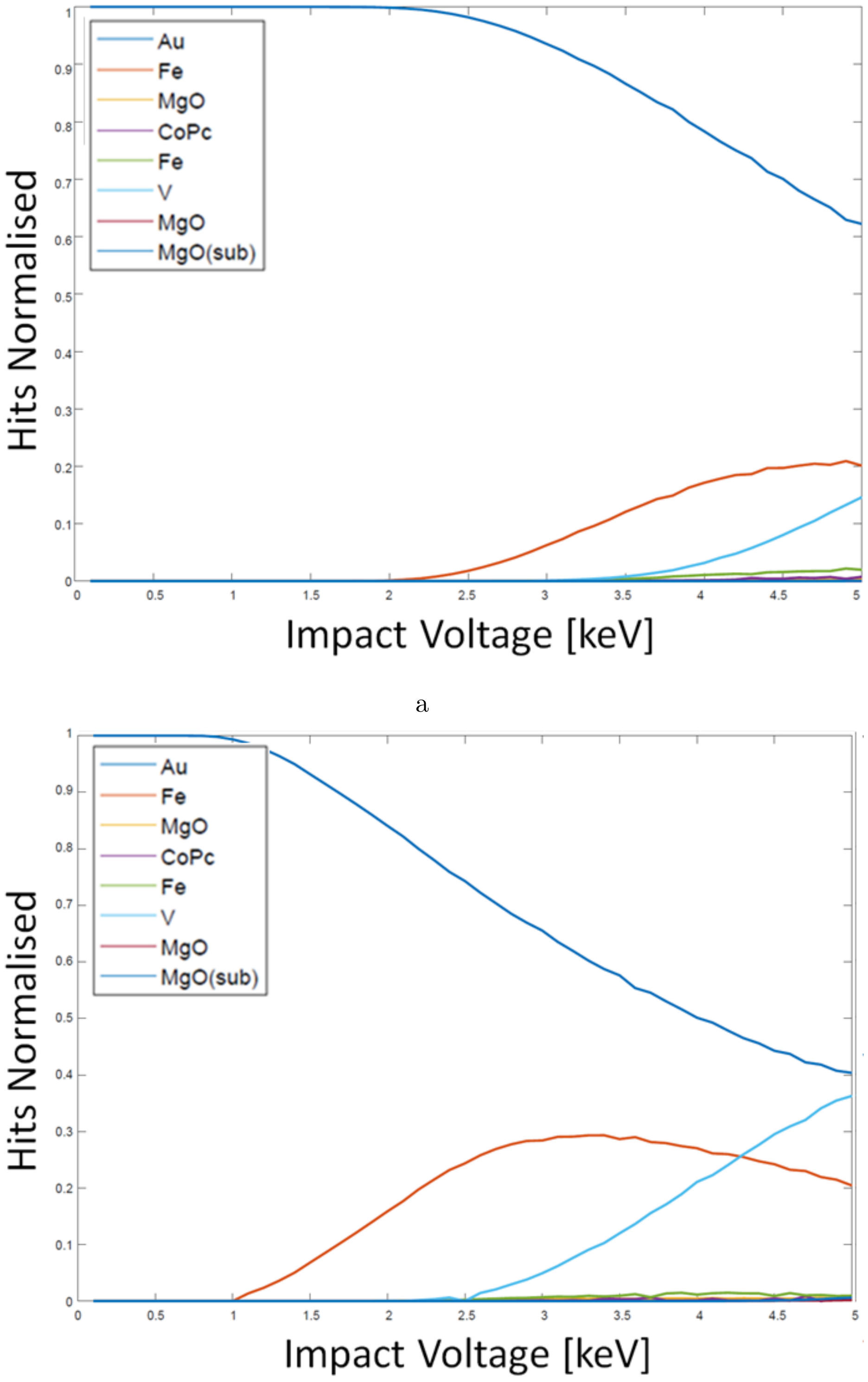

a

b

Figure 6.2: CASINO simulations for the a. 3.2 and b. 0.32 nm CoPc samples.

## 6.2 Considerations when Imaging Organics

When imaging organic samples with electrons there are many considerations to make. These considerations are largely due to the fragility of the molecules and its reactiveness. The most important consideration is the acceleration voltage. Depending on the sample a high voltage can damage interconnects between the organic molecules very easily. For this specific sample the Au and Fe capping layers protect the organics. Due to this there was no issue with permanent damage, but care was taken to keep the voltages used as low as possible.

When imaging in a TEM this becomes a much larger consideration. As a TEM typically functions with an acceleration voltage $>$100 kV there is strong potential for sample damage. This is even more relevant in cross section TEM as the layer is fully exposed to the beam. To avoid any permanent damage the exposure time was reduced ($<$0.5 s) as that decreased the total flux. Working at lower magnifications also helps although that is not always possible depending on the study requirements.

An additional concern shared by all non-metallic samples is charging. This is the build up of negative charge, either across the samples or in isolated regions, which cannot dissipate the electrons. In an SEM this charge usually appears as a shifting bright spot due to the deflection of electrons. In a TEM this charging will appear as a more subtle distortion of the image. This will make it appear out of focus and will be difficult to resolve. There are two ways to reduce the effects of charging. The sample can be coated with a conductive material. This is particularly useful in an SEM when looking at entirely non-metallic samples. However, this would be impractical when used alongside the non-destructive imaging technique as it adds extra unknowns. A lower beam current can also be used. This has been shown to reduce the build up of charge on samples, but will reduce te number of scattered electrons available to detect. When imaging this particular sample charging was unlikely to be much of an issue. This was because the non-metallic layer is sandwiched between metal layers; which conduct away any electrons.

Another significant issue is the build up of carbonaceous compounds. In a TEM this only happens on a small scale due to the very high vacuum. In addition C has a very low scattering cross section so it will have a very minor effect on the transmission image. Due to the similar Z values, this carbon can still affect other light elements making them appear less crystalline. This should be an effect that is hard to observe. In an SEM this is not the case. Due to the lower vacuum in an SEM there are more contaminants which in turn increases the amount of C fixed to the surface. Usually this is somewhat uniform but still amounts to a layer around 5 nm thick. When trying to study other light element layers this may make a difference. To reduce the effects of this C several steps were taken. The sample was cleaned between sessions. This ensures that subsequent build up will not cause issues. Ensuring the vacuum is as high as possible before switching on the beam also helped. On a related note, reducing the exposure time of the sample would help significantly as a lower flux reduces the build up. In a practical sense this meant that focussing was done away from areas of interest.

## 6.3 Non-destructive Imaging Investigation

Once the simulations had identified the accelerating voltages required to probe the CoPc and MgO interfaces imaging could be undertaken. Whilst preparing to image the sample the listed considerations were taken as recommendations. The sample was cleaned thoroughly before mounting and the system was pumped to as high a vacuum as possible, approximately $10^{-7}$ Pa, before imaging commenced.

The first stage of imaging was performed at the centre of the sample along its boundary. This was done as it would be an area with a very clear contrast change which would allow the suitability of the accelerating voltages to be checked. Many images were taken along this boundary at 2, 2.2 and 2.4 kV. These images were focussed away from the boundary to reduce the exposure time. Once taken these images were processed using the method outlined in section 4.1 and reviewed. An example of these sets of processed images and their constituents is shown in fig. 6.3.

The clearest feature in the subtraction images is the line down the centre of the image. This is the boundary between the two sample structures. Importantly this feature is not visible in the SEM images, fig. 6.3c and fig. 6.3d. This is a great example of the non-destructive subsurface imaging technique in practice. The large contrast change caused by the different thicknesses of the CoPc has been highlighted very clearly. This also demonstrates that the

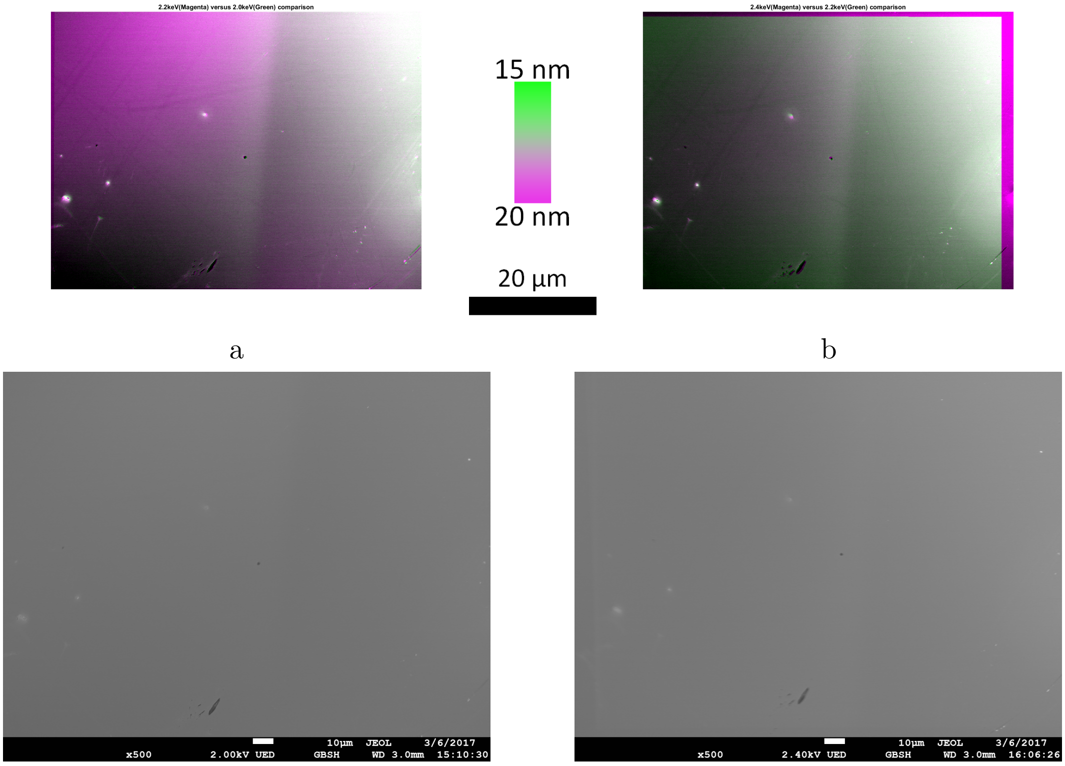

a b

c d

Figure 6.3: Figures a. and b. are the composite subtraction images for 2.2-2 keV and 2.4-2.2 keV respectively. These were taking along the boundary. Figures c. and d. are the 2 and 2.4 keV SEM images used when making the composite subtraction images.

voltages selected are optimal for this sample.

Looking closer at the composite subtraction images dark line features can be seen, particularly on the left side of the boundary. These dark channels are not evident on the unprocessed electron images and are only visible in the composite subtraction images. This must mean they are subsurface features. As they appear to be more strongly visible in fig. 6.3a it is probable that these channels originate in the CoPc layer. However it is difficult to understand why they seem to only appear on the left side of the image *i.e.* the side with the thicker CoPc layer.

To attempt to find the origin of these channels extensive imaging was performed on the side of the sample with 3.2 nm of CoPc. The same imaging conditions were used for this set of images as before. A similar array of images are shown in fig. 6.4. These include both the SEM images and the composite subtraction images. These were taken >2 mm from the boundary to assist in identifying the origin of these channels. If they were similar in form far away from the boundary then it is clear that the boundary is not their origin.

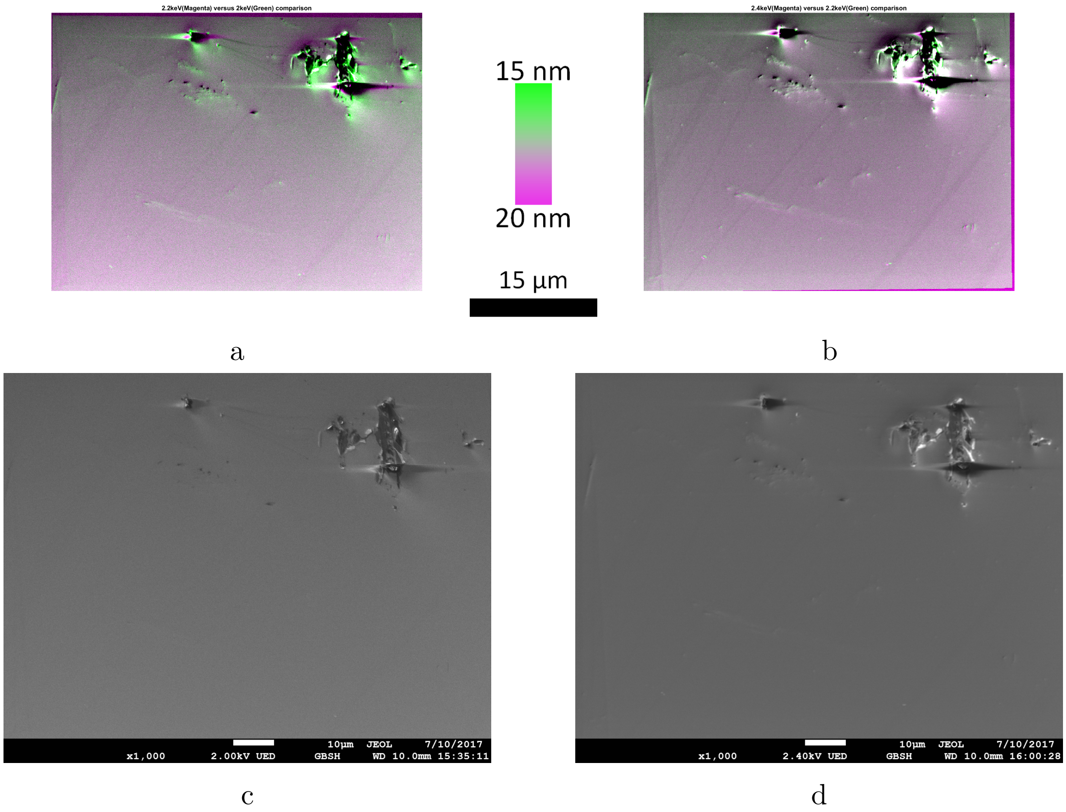

Figure 6.4: Figures a. and b. are the composite subtraction images for 2.2-2 keV and 2.4-2.2 keV respectively. These were taking at the 3.2 nm CoPc site, A. Figures c. and d. are the 2 and 2.4 keV SEM images used when making the composite subtraction images.

Looking at the SEM image of the area there were not many features and no channels. As the features only appear once the images have been processed little can be gained from these images apart from confirming the presence of surface defects. In the processed images a series of channels are revealed. These are numerous but do not seem to have a preferred direction. There was also a range of thicknesses of the channels, from around 0.5 to 3 $\mu$m wide. Again the idea of a lack of preferential direction holds true and the size of the channels stays within the given range consistently.

It was not possible to get an estimate of the length of these channels as a lot of them run from edge to edge of the images. However some are relatively short around 20 $\mu$m. This gives the impression that the cause of these channels are structural but it must have a random ordering, much like a stacking defect. These images alone were not enough to identify what these channels are and what causes them.

To provide further information on the mechanism of formation of these channels further imaging was performed on the side of the sample with 0.32 nm of CoPc. Once again the same imaging conditions were used for this set of images. Examples of the SEM images and the composite subtraction images are shown in fig. 6.5. As with the 3.2 nm CoPc sample these were taken >2 mm from the boundary to ensure it would have no influence on the structure. In this case the interest lay in whether or not there were channels and if there were to determine if they were similar.

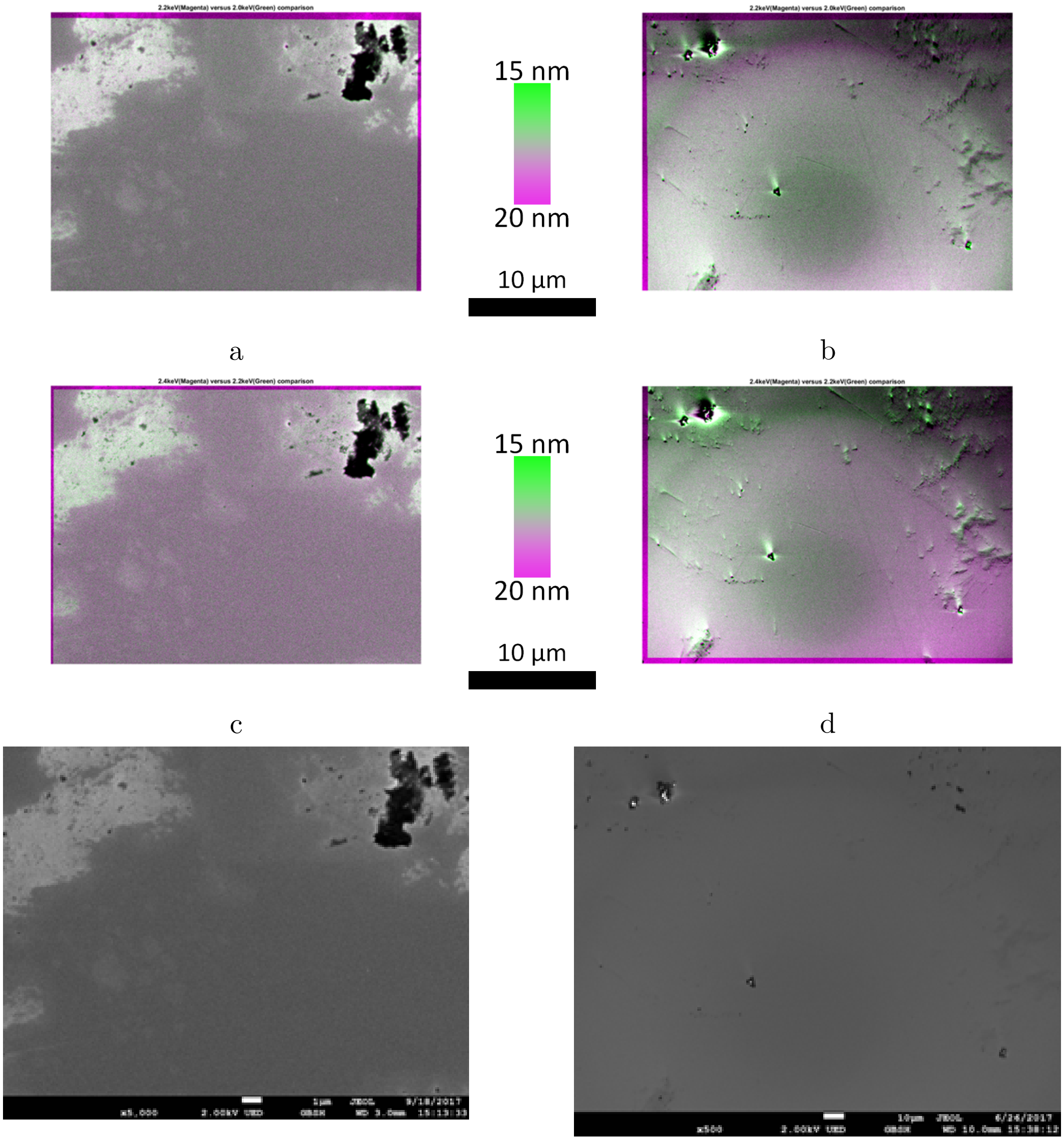

a

b

c

d

e

f

Figure 6.5: All images were taking at the 0.32 nm CoPc site, B. Figures a. and b. are the composite subtraction images for 2.2-2 keV taken from two different sites. Figures c. and d. are the composite subtraction images 2.4-2.2 keV and 2.4 keV taken from two different sites. e. and f. are the 2 keV SEM images used when making the composite subtraction images.

During the imaging process a significant number of images were similar to fig. 6.3 and fig. 6.4. In these cases no channels were found after the subtraction was performed. This was unexpected as some channels could be seen on this side of the sample such as in fig. 6.3b. However it was possible that these channels were induced across the boundary by the channels on the side of the sample with 3.2 nm of CoPc.

However this idea was dismissed once similar subsurface features were found such as the ones shown in fig. 6.5b. In these composite subtraction images there are channels. The channels on the 0.32 nm CoPc sample are similar in form to those on the 3.2 nm CoPc side. The main difference is the frequency of occurrence. It seems that the channels form much more sparingly on the 0.32 nm CoPc when compared to the other sample. However these channels also seem to be randomly oriented. Once enough channels had been found the thicknesses were measured. They had a similar range of thicknesses, from around 0.5 to 2.5 $\mu$m wide.

The CoPc molecule has a platelet-like structure seen earlier in fig. 6.1a. It is preferred for the structure to lie flat relying on the intermolecular bonds to aid in assembling a monolayer or a series of them. If deposited perfectly these monolayers would have a consistent density and thickness. However, either due to a rough surface or a stacking fault it would be possible for these platelets to overlap like a roof tile. In extreme cases the CoPc molecule may even stand on its edge. Both situations would create regions with a different density and potentially a different thickness. This is the most probable cause of the channels.

The observed difference between the 0.32 and 3.2 nm CoPc sample can be explained by extending this idea. In the case of the 0.32 nm CoPc sample there is an expectation that there will be one monolayer deposited. Whilst both of the described faults are possible they are only likely to occur in areas with either a large degree of surface roughness or areas where there has been an irregular sputtering rate. However where this does happen the effect will be pronounced and the overlapping can double the thickness for example. The 3.2 nm CoPc sample would have significantly more layers. This would greatly increase the chances of some form of stacking fault occurring. Additionally it is likely that once an area has on overlap or an upright molecule this will cause a knock-on effect continuing the fault into higher layers. This could explain why the channels appeared much more frequently in the 3.2 nm CoPc sample.

In either case further investigation was needed to confirm this hypothesis. EDX was performed in the manner described previously but the results were not conclusive. This was due to the presence of carbonaceous compounds on the surface making it difficult to discern the origin of any carbon X-ray signal. Whilst there were other additional options it was decided that the best technique to try to identify the origin of these channels would be cross-sectional TEM. This would also allow the two techniques to be compared directly.

## 6.4 Transmission Electron Microscopy Investigation

The sample preparation for cross-sectional TEM was described in section 2.1.4. As discussed earlier, it is not possible to use a lot of cleaning fluids such as acetone with organic compounds. For this reason mechanical polishing could not be used. This meant that the cross-sectional sample had to be produced and mounted in the FIB. Lamellae were produced with large regions with a thickness of approximately 50 nm. These were mounted to 4 post lift out grids for use in the TEM. These grids allowed four samples to be prepared sequentially without the sample needing to leave vacuum. Each sample, the 0.32 and 3.2 nm CoPc, were turned into lamellae during separate sessions and later mounted onto separate grids. This was to reduce the chance for confusion during TEM analysis.

Once the lamellae were prepared imaging was performed. This was done using a JEOL JEM-2010 TEM. Imaging was performed at 200 kV. This allowed for sufficient resolution to resolve all the layers, whilst reducing the likelihood of beam induced damage to the more sensitive organic layer. In addition a double-tilt sample holder was used to allow an orthonormal projection to be achieved. The 3.2 nm CoPc samples were imaged and examples of these images are shown in fig. 6.6. As can be seen the layers are very discrete and have been labelled in fig. 6.6b. The layers above the capping layer are protective layers that were deposited before the milling process began.

Apart from having discrete layers the continuity of the layers, particularly the CoPc layer, are shown in these images. Sampling the thickness gave a

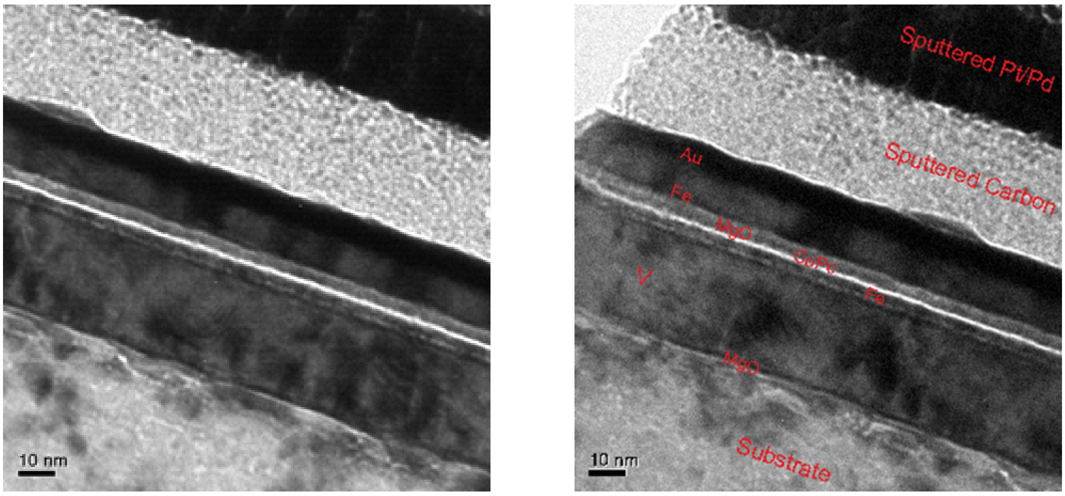

a b

Figure 6.6: Two cross-sectional TEM images of the 3.2 nm CoPc stack. One of the images is labelled.

result of (2.2±0.2) nm. Whilst the thickness remains consistent there is a small deviation in position across the imaged sample of approximately ±0.2 nm. This is likely to be caused by the roughness of the structure below the CoPc layer. It was not possible to get a diffraction pattern using selected area diffraction as there was not an aperture which could isolate a layer of this thickness. This would have given a strong insight into the crystallinity of the samples layers, particularly the MgO layer on top of the CoPc.

Imaging was also performed on the similarly prepared 0.32 nm CoPc lamellae. The same conditions were used and examples of the data collected are shown in fig. 6.7. fig. 6.7b shows the labelled layers.

Once again discrete layers are observed, although the CoPc layer isnt equally distinct. This may be due to its proposed thickness of 0.32 nm. Whilst it is clearly observable it maintains the same thickness, measured to be (0.6±0.1) nm, however the layer disappears for a stretch, approximately 4 nm, in one of the images shown in fig. 6.7b. In contrast to the 3.2 nm CoPc sample, this sample had almost no position deviation. This may be due to the fact that the layer is so thin, either there isnt enough material to deviate or the deviation is too small to measure at this resolution. Once again selected area diffraction was not possible due to the available apertures.

Apart from the different thicknesses found in the CoPc layer the structure of the two samples were very similar. The only variance was the roughness in

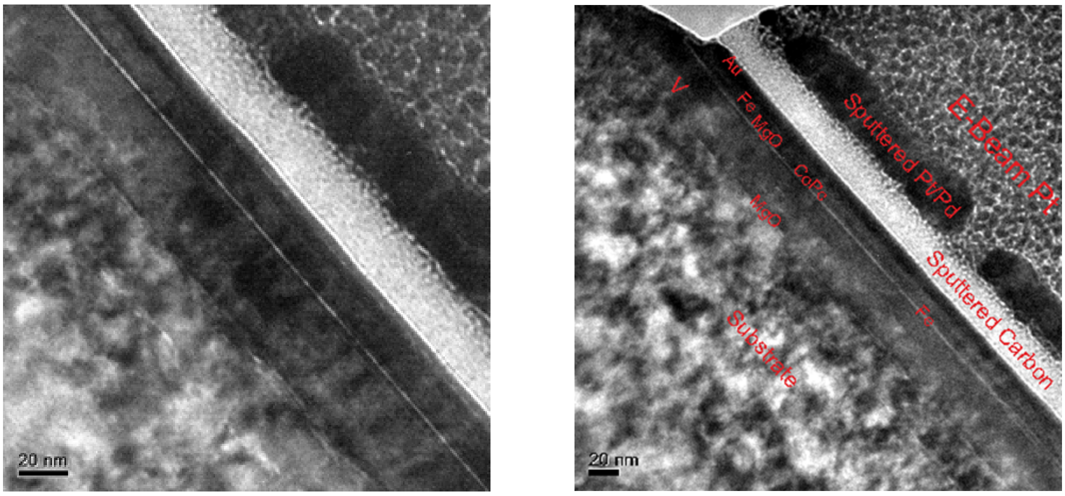

a

b

Figure 6.7: Two cross-sectional TEM images of the 0.32 nm CoPc stack. One of the images is labelled.

the CoPc layer, although it is unknown whether that is due to the resolution or structure. In addition there were no instances of channels being seen, unless the area where the CoPc disappeared from view in fig. 6.7b was one such channel. To gain more information on both the structure and the channels it was decided to attempt higher resolution imaging. This would still not allow diffraction patterns to be gathered due to how thin the layers are, but would probably show lattice fringes which can be indicative of the crystallinity.

To take higher resolution images, it was not necessary to change the equipment, but in some cases it was necessary to thin the samples further. This was to ensure there was enough electron transmission to image properly. To check if this was needed it was necessary to try to image the samples. Any that did need thinning were returned and thinned in the FIB.

Once the samples were prepared they were imaged. It was important to ensure the sample was aligned along the zone axis. Whilst this allows for the best imaging it is worth noting that not every layer will prefer the same alignment but the most prevalent layer will contribute the most. In this case that is the Vanadium seed layer. Example images are shown in fig. 6.8.

These images can be used to both accurately measure the CoPc thickness and get information about the crystallinity. It was not possible to measure the diffraction pattern directly because a small enough aperture was not available to isolate a 3.2 nm layer on this TEM.

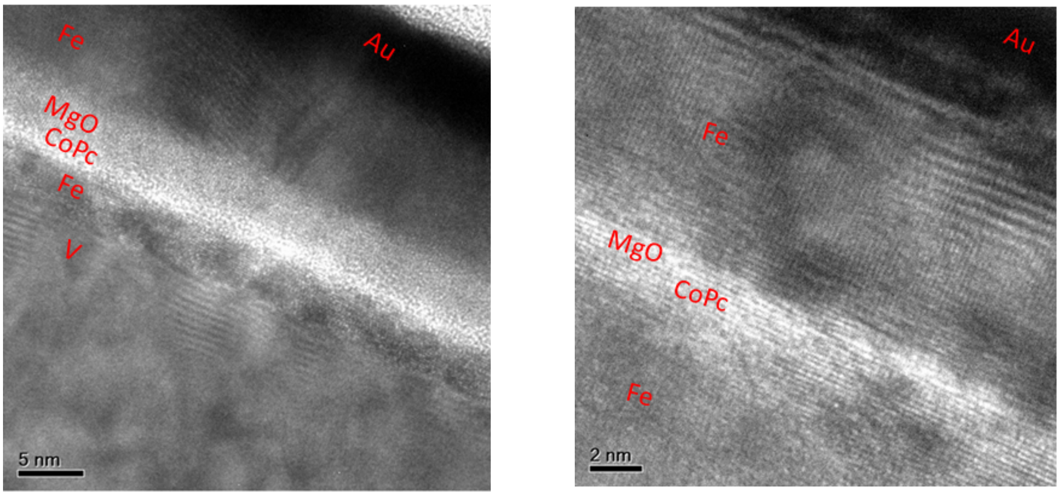

a

b

Figure 6.8: Two high resolution cross-sectional TEM images of the CoPc stack, a. is from the 3.2 nm sample and b. is from the 0.32 nm sample.

The CoPc layer was measured to be (1.7±0.2) nm in the 3.2 nm sample, where as it was measured to be (0.50±0.07) nm in the 0.32 nm sample. It is worth noting that there was more error in the 0.32 nm sample as the layer was much harder to differentiate due to its diffuse nature. That is important as this will disrupt the integrity of the layers. This diffusion of material above and below the platelet-like CoPc molecules could also be the cause of the channels in the 0.32 nm sample instead of mis-orientation as was first thought.

In addition to the measurements it was possible to see the crystalline structure of the MgO that was grown on top of the CoPc. The ordering cannot be found out from the images shown in fig. 6.8 because all of the layers were in the field of view, making the isolation of the MgO reflections very difficult. However its ordered nature is encouraging as it demonstrates that this combined metal oxide/organic tunnel barrier can be produced.

## 6.5 Summary

Two differing sections were produced on one sample. These samples have the stack structure shown in fig. 6.1b, where the only difference is the thickness of the CoPc layer, each section having either 3.2 or 0.32 nm respectively. These were imaged using the non-destructive imaging technique and this revealed channels in both sets of samples although they appeared less frequently in the 0.32 nm sample.

To help identify the cause behind this, to observe the distribution of the CoPc and to observe the crystallinity of the structure in general, TEM was employed. This confirmed that the MgO layer was largely crystallised as were the other layers. The CoPc layer was the only one that was largely non-crystalline. The thickness of the CoPc layer was measured at two different magnifications. This gave an average result of (1.9±0.2) nm for the 3.2 nm CoPc and (0.54±0.04) for the 0.32 nm CoPc. These measurements are different from the expected thickness of the layers. In the case of the 0.32 nm CoPc it is likely that this is caused by the molecule itself, the difference between the measured and expected value is on the same scale as the dimensions of the molecule. Simply adding one extra mono layer would explain this. In addition it is possible that intermixing of the MgO has made the layer appear thicker than it is. High resolution EDX would be needed to identify this. The 3.2 nm CoPc layer is a little different. In this case there is a large difference. However This could be explained by mis-orientation of the molecule during deposition. If the molecule stacked edge-on during deposition, then relaxed to be flat, it could explain such a large difference. In addition it explains the thickness and position variance. This could also be the reason for more channels, areas which did not relax would cause similar features.

As for the origin of the channels there are two possible causes: Given the structure of the molecule it would be possible for it to generate a stacking fault if it was deposited in the wrong orientation. These stacking faults would then cause a shift in the density of the region causing it to have a lower BSE yield. This would be more likely to happen in the 3.2 nm CoPc sample which is what is observed in the SEM images. However when looking at the TEM images no evidence of these stacking faults were seen. It is quite likely that this is due to the fact that the non-crystalline nature of the CoPc would make it too difficult to observe the molecular orientation. It does mean that this cannot be confirmed as the source of these channels.

When looking at the TEM images particularly in the case of the 0.32 nm, there was a lot of displacement of material around the CoPc layer. Whilst this did not seem to break up the layer it definitely caused more roughness. This sort of displacement could also be responsible for the channels. A large adjustment of layer position like the one observed, would be seen on the BSE image. It is possible that this would appear darker than the surroundings as lighter elements are more likely to diffuse into the space. However the layer in question is largely C based so any change should actually produce more BSE, which is not observed in the SEM.

Due to limitations on resolution it was not possible to successfully identify the cause of the channels. However the technique was able to identify the presence of them and now it is necessary to find alternative methods to investigate this sample.

# Chapter 7

# Investigating Devices *in situ*

The non-destructive imaging technique has already been used to image sub-surface interfaces in devices. The previous studies investigated the active interfaces with particular focus on the interface quality. This required finding the structural differences in the device using the elemental composition of the material. However, another way to investigate the interfaces in similar devices would be to track the charge distribution at these junctions. This would be particularly useful in devices where the adjacent layers have similar values of Z.

The charge in a sample has a predictable effect on the BSE images. The sensitivity of the BSEs is dependent on the incident energy of the electrons. When the accelerating voltage is high (>10 kV), the images become less sensitive to a low level of charge <1 keV. This allows the charge distributions to be visualised across a surface. Using the methodology that has already been developed, this can then be analysed subtractively to look at charge distributions at a sub-surface region of interest.

The only difficulty to overcome when using charge as a contrast in sub-surface regions is providing that charge. The electron beam is highly unlikely to induce charge in a sub-surface region so it is necessary to supply the charge externally. As the region of interest is typically the active region, this can be done *ex situ* or *in situ*. An *ex situ* supply is simple to arrange but it is hard to ensure the charge doesn't dissipate when preparing the sample for imaging. In addition this can only provide one example of the distribution. An *in situ* supply circumvents these issues providing the supply continuously to the sample and it allows for a study into the change of the charge distribution.

The major difficulty with supplying the current using an *in situ* method is ensuring it will work within the SEM environment.

## 7.1 Experimental Set-up

Two distinct parts are needed to create a suitable *in situ* system. The first part is a feedthrough and the second part is a stage mount. The feedthrough will allow connections to enter the vacuum environment of the SEM, meaning it will have to both be airtight and prevent X-ray escape. On the projects SEM, the JEOL JSM-7800F *Prime*, the transmission electron detector port was chosen to mount the feedthrough. This port was non-standard so a custom feedthrough was designed. This is shown in fig. 7.1.

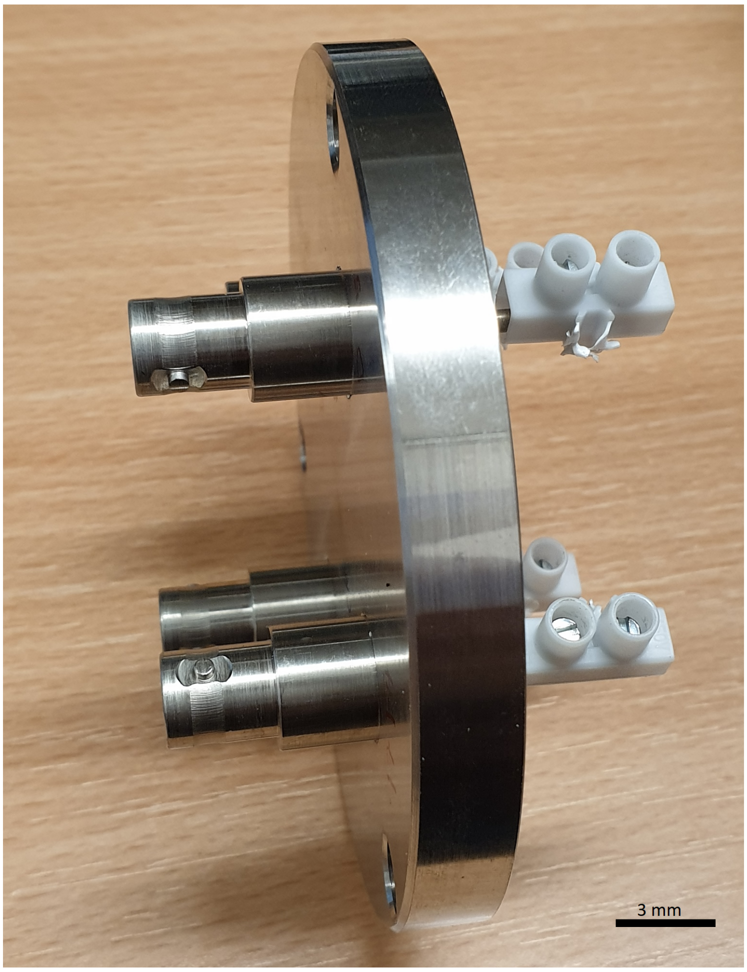

Figure 7.1: The custom feedthrough for the transmission electron detector port of the JEOL JSM-7800F *Prime*. This feedthrough has four external BNC connectors each with an internal signal connection.

Once the feedthrough was manufactured it was tested for both vacuum and radiation leaks. This was done by mounting it on the SEM and pumping it down. The vacuum was then held for 24 hours. The electron beam was then turned on with an acceleration voltage of 20 kV. A Geiger counter was then used to check for radiation leaks. Once it was confirmed that there were no leaks of any kind the feedthrough was approved for use.

The stage mount had to be made of a material suitable for the conditions within an SEM and support or fix the connections to the device. 3-D printing was chosen as the method for fabrication for this mount. This allowed many iterations to be made, with minute detail, in a very short time period. The plastic chosen, acrylonitrile butadiene styrene, was stable enough to be exposed to an electron beam and design features were included to reduce the out gassing within the vacuum. The final design is shown in fig. 7.2.

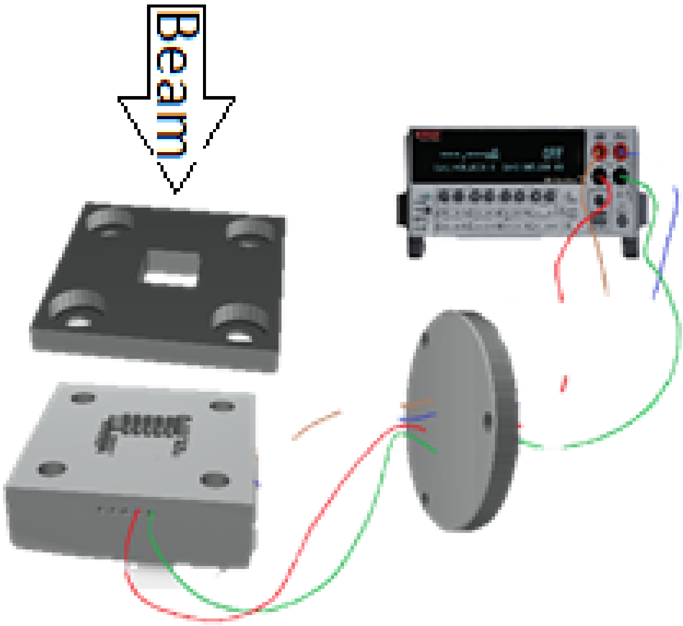

Figure 7.2: The designs for a custom sample mount to hold chip carriers within the JEOL JSM-7800F *Prime*.

As well as being able to be within a vacuum environment, the stage mount also had to support or fix the connections to the chip carrier. It was known that all devices would be mounted and bonded to a standard size chip carrier. Typically connections would either be soldered to the chip carrier, or like in this case, a mount would press the connections into contact. To this end a lid was added to the sample mount, also shown in fig. 7.2. This lid acted to both secure the chip carrier in place but also to press the wires into the contacts, providing the connection. This design was tested both on a bench and in the SEM environment.

With both the feedthrough and sample mount designed, both a source and meter were required. A Keithley 2400 SourceMeter was chosen to perform both of these functions. This allowed the flexibility to either supply a constant current or voltage, depending on the devices being investigated and to measure both the current and voltage using a standard four-terminal set-up.

## 7.2 Spin Torque Devices

With a set-up designed and ready it was necessary to design a study to test the system. A series of lateral spin valve devices were chosen for this. These were Fe(100 nm)/GaAs(001) lateral spin-valves, designed and produced by colleagues in the University of York. The epitaxial Fe films were grown using UHV MBE. This process was optimised previously by Fleet *et al.* [84]. The films were then patterned using a combination of electron-beam lithography, photolithography, Ar-ion milling and chemical etching. They are shown in fig. 7.3.

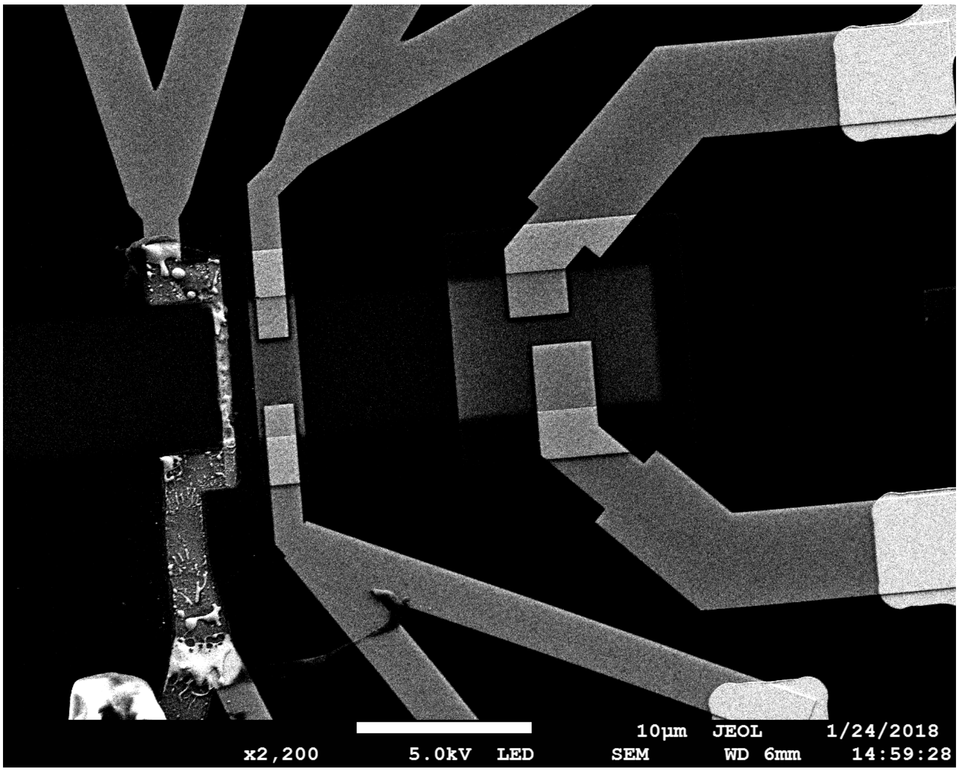

Figure 7.3: Fe(100 nm)/GaAs(001) lateral spin valves. These have 1, 4 and 20 $\mu$m wide Fe wires, moving from left to right as seen. These are the first detector, injector and second detector respectively.

As can be seen in fig. 7.3, the width of the Fe wires, from left to right as seen, were 4, 1 and 20 $\mu$m. The 4 $\mu$m wire acted as the injector. The 1 and 20 $\mu$m wires acted as the first and second injector respectively. The GaAs mesa was 2 $\mu$m thick. This device utilised a non-local geometry to introduce spin-polarised electrons into the GaAs mesa. This required an applied current, between 0.25 and 400 $\mu$A which excites and activates the mesa, allowing electron egress.

To simulate these devices to identify the correct impact voltages needed, CASINO was used. In this case the 2D structure used was that of Fe(100 nm)/GaAs. Whilst this was not suitable for areas without Fe coverage away from the wires, it was the better choice to study the Fe/GaAs interface. Impact voltages of 2.5 and 3 kV were found to be most suitable to investigate the interfaces of interest.

Before imaging went ahead the system in its entirety was tested on the bench top. This involved wiring the entire system including the feedthrough. Then the voltage response to a changing current was measured and compared with previous results. All measurements were within ±0.02 mV of each other across the 100 - 300 $\mu$A range that was tested. With this confirmed the system could be mounted on the JEOL JSM 7800F *Prime*. Given the time spent developing the experiment before this point, it was not necessary to make any adjustments.

Once the experiment had been set-up, as discussed in section 7.1, the way the beam affected the electronic properties of the lateral spin valve was tested. This involved using a low magnification beam, 200x magnification, at a typical beam current, approximately $10^{-8}$ A. Once the spin valve was exposed to the beam the voltage values at a given current were measured across the same range. This yielded no change as was expected. This was due to the fact that the incident beam current was much lower than the applied beam current, being at least three orders of magnitude lower.

After these tests were complete, and the electronic properties were confirmed to be stable under the SEM. It was then possible to image the lateral spin valve. The plan for this imaging was to create a series of composite subtraction images whilst increasing the current flow through the device. As the scattering product yield would be affected by the presence of a current, this would allow the activated areas of the lateral spin valve to be imaged. To sample the maximum range three main supplied currents were chosen 0.25 $\mu$A, 200 $\mu$A and 400 $\mu$A. The resultant composite subtraction images are shown in

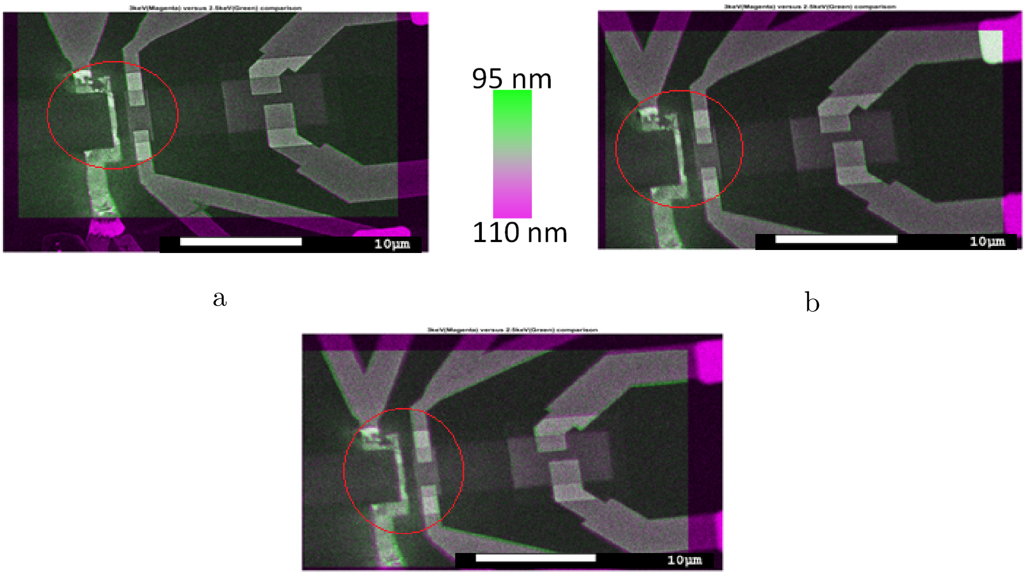

a

b

c

Figure 7.4: Composite subtraction images of a lateral spin valve taken at a. 0.25 $\mu$A, b. 200 $\mu$A and c. 400 $\mu$A

fig. 7.4.

As shown in fig. 7.4a, the spin injector, circled far left, is very bright. This indicated that the Fe/GaAs interfaces underneath the injector were activated. There were some distributions visible in the composite subtraction image. Three 1 $\mu$m diameter grey dots were on the 4 $\mu$m wide injector, circled right side. These darker regions are generating less BSEs than the surrounding area. This signifies that the number of scattering products generated in that dot were smaller than those in the surrounding are.

Based on this it can be concluded that the current distributions were not uniform when there was an applied current application of 0.25 $\mu$A. When the applied current was increased to 200 $\mu$A as shown in fig. 7.4b, only one grey dot is observed in the centre of the injector. This indicates that more of the mesa could be activated. Finally, increasing the current further to 400 $\mu$A removed all visible dark regions in fig. 7.4c. This indicates that the current distribution was likely to be uniform. This demonstrated that the method can visualise electron charge concentrations and the activation mechanism of these devices.

Given that this can be used to visualise the electron charge concentrations, it follows that it is possible to calculate an effective junction area which is active for transport. This was done by measuring the total area and then subtracting the area of the dark spots. This would leave a total active area. It is easier to subtract the dark spots as they appear to be more spot-like so their area can be estimated as a circle of the same diameter.

| **Supplied Current ($\mu$A)** | **Effective area (%)** |
|---|---|
| 0.25 | 82 |
| 200 | 88 |
| 400 | 92 |

Table 7.1: The average effective area of the injector at each current for the five lateral spin valves measured.

This method of calculating the effective junction area was used to measure the active area of the injector for the whole batch of lateral spin valves imaged. The areas were then averaged across the samples at each of the three currents. This data was collected in table 7.1. The average values demonstrated a similar trend to the earlier observations. However being able to quantify the active area is still useful particularly for more complex systems.

The cause for the incomplete activation of the injector is structural. When looking at both the change between image sets and the composite subtraction images themselves, it appears that there were both macro and micro-structural problems. A couple of regions remain dark throughout the image set. These regions are probably related to issues with the surface bonding. Areas where the Fe wire has peeled off will narrow increasing the resistance in the area. This will encourage the use of other current pathways causing the inactivity of that region. However it would be expected that if enough current was provided these areas would eventually brighten up.

Areas that brightened readily as more current was supplied are more likely to be micro-structural issues. These are issues such as pinholes or in general areas where individual charge carriers can be trapped. As the current is increased slightly, these sites will no longer be able to reduce the flow of charge carries in the area allowing it to become active.

## 7.3 Summary

An ambitious extension to the non-destructive imaging technique, *in situ* imaging proved to be challenging. However, with careful modifications to the base SEM system the ability to power and image devices was possible. Some well characterised lateral spin valves were chosen to test the systems limits.

After the equipment and modifications, the effect of the electron beam on the devices behaviour was the largest concern. Testing under gentle beam conditions ensured that if there was any issue it would be minimal. In this case no change in behaviour was noted. This is probably due to the large difference between the incidental beam current and the current supplied. However it is worth noting that devices that require currents in the region of nA may be affected by the beam.

Generating composite subtraction images revealed areas of the injector that were not active. This changed with the applied current with the amount of active area increasing with current. Based on this an effective area was defined as the total area of the device minus the inactive area which corresponds to dark spots on the sample.

# Chapter 8

# Conclusions and Further Work

This project has taken the proof of principle presented by Hirohata *et al.* [6] and developed a tested, repeatable methodology. This involved the development of software capable of creating composite subtraction images without the need for expertise. In addition, both the 2D and 3D version of CASINO was utilised to assist in calibrating this technique. These were all developed with the intent to use the technique in quality assurance, but also to investigate other areas it could be used.

Once the methodology had been developed it was tested by comparing four similar thin film wafers. These different devices primarily varied the seed layer of Ta. When investigating the devices defects were identified as domain wall pinning sites. with different seed layers offering different densities of these sites. To follow this up magnetic measurements were performed to see how the magnetisation curves were affected. These measurements helped to demonstrate that the number of sites at the CoFeB/MgO interface could be correlated with an increase in the number of weakly magnetised regions. This identified a preferred seed layer thickness, 0.5 nm.

This study acted to both confirm the methodology that had been developed and opened up a new area for the technique to be utilised, optimisation. To explore this avenue a series of investigations into magnetic tunnel junction were performed. The first investigation looked at a series of patterned junctions provided by Tohoku University, described in section 5.1. These devices were split into two groups based on their TMR. The investigation aimed to identify some of the reasons behind this difference. The non-destructive imaging technique and EDX were used to identify a build up of aluminium carbide along the edges of the pillar. It was put forward that this formation, which occurred during the device fabrication, shorted the pillars which had low TMR. This was tested by adjusting the fabrication conditions and measuring an improved yield.

The next MTJ study looked into production quality MTJs, discussed in section 5.2. The aim of this study was to image the MgO tunnel barrier, to assess its quality. This was not possible due to either the size of the pillar which was 100 nm by 100 nm, or due to discrepancy between the MgO layer thickness and the rest of the stack above it. The latter is the most likely cause as the difference in percentage of electrons contributing to the images created by the two acceleration voltages is not large. However the technique was able to provide a unique way to characterise the shape of the pillar including its domed top. The non-destructive imaging technique also managed to measure the distribution of both pillar sizes and the $Si_3N_4$ encapsulating it.

The final MTJ study looked at structures with Au capping layers >200 nm, made in Tohoku University. The aim of this study was to investigate the tunnel barrier layer and its surrounding support layers, then compare them with TEM images collected. Given the thickness of structure above the layer it was expected that this would be difficult. The simulations performed acted to confirm this. Due to these reasons, the imaging provided no information. These conditions were evidently outside of the limitations of this technique. Attempts were made to reduce the thickness of the Au capping layer to attempt to proceed with the imaging, but they proved unsuccessful. TEM images were collected but without any composite subtraction images to compare it to they were just passed on to the collaborators. This investigation was unsuccessful as the limits of the non-destructive imaging technique were not fully known. It showed that there are sample structures that are not suited to this sort of investigation.

Given the good results whilst investigating thin film samples, another collaborator provided a thin film wafer, intended for use in organic based MTJs. These MTJs used a dual layer tunnel barrier, consisting of an organic molecule CoPc and MgO. Two samples were produced on the same wafer. The thickness of th CoPc layers were varied, the details can be found in chapter 6. The non-destructive imaging technique was used to great effect here, identifying channels in both samples. These channels occurred more frequently in the thicker 3.2 nm CoPc sample. A TEM investigation was undertaken to attempt to discover the cause of these channels. The most likely cause of these channels is stacking faults caused by the mis-orientation of the CoPc. This is unlikely to be visible in a cross-sectional TEM image as damage caused by sample preparation will cover it, so it could not be confirmed.

The final study looked at the possibility of using the non-destructive imaging technique to image active layers in powered devices. This involved designing and fabricating an *in situ* interface system, for use with the SEM. Once that was completed some Fe(100 nm)/GaAs(001) lateral spin-valves were imaged. This imaging managed to identify dark spots in the device when powered. These were considered to be areas of low current and changed as the applied current was increased. This allowed the effective area of the junction to be identified.

## 8.1 Further Work

This project aimed to take an idea that had a simple proof of concept and develop a methodology to use it. Once that was done the aim was to test it on a wide variety of systems that would benefit from a non-destructive method to investigate the sub-surface. This was accomplished, however the fact that the study aimed to look at as many different samples as possible did leave many gaps useful to fully realise this non-destructive imaging technique.

The largest issue and the first proposal is related to the depth of each study. As the samples were supplied by a collaborator with little options of making changes the study process was very one directional. A sample came in, findings were returned and the study was over. The most successful study was where the findings were fed back into the fabrication methodology.

Given this any future study should involve a committed collaboration with the aims to fully optimise a system. Alternatively a study could be done in house, where the growth and fabrication of devices can be managed. Given the success at looking at thin films I would suggest first an investigation into the optimisation of the seed layer thickness of a sample such as the one used in section 4.2. This could be easily employed alongside cross-sectional TEM allowing the techniques to be compared directly. In addition magnetic measurements could be performed alongside the imaging study, on the thin films, to confirm that the changing seed layer is not affecting the magnetic properties.

An additional system worth investigating in a similar manner would be a tall device structure, such as in section 5.1. The non-destructive interfacial imaging technique could once again be used to optimise the fabrication of devices. In this case the study would start with an already optimised thin film, possibly continuing from the previously suggested study. Care must be taken that the device is suitable for imaging, *i.e.* they don't have veryelectrodes that are $>$ 100 nm. Devices should then be fabricated, tested and measured. This will allow an investigation into the yield to take place. The imaging could be performed alongside EDX and TEM with any substantial results being fed back into the fabrication process.

Beyond device optimisation there is a need for a study which focusses more on the absolute spatial resolution of the non-destructive interfacial imaging technique. This would also need to track how those values change with the depth of penetration. This could also investigate the effects of changing Z of the target layer. In this study it would be ideal to use MBE to produce a set of 'targets' to test the resolution. For example a 1 nm by 1 nm square alongside a 10 nm by 10 nm square. If they were made from a very high Z number material it would be easier. This should then be capped with a layer of known thickness. The lower the Z of this layer the better. The focus on imaging can be on the interface between the substrate and capping layer. This simple system could test the spatial resolution of the non-destructive interfacial imaging technique. the thickness of the capping layer can be adjusted to see how this resolution changes with depth.

With these additional studies the non-destructive interfacial imaging technique will be fully realised and ready be used to explore additional applications.

# Appendix A

# Publications

This Appendix lists the publications that have been produced as part of this project. It also links them to the chapter that contains the published material where relevant.

The following work is discussed in section 5.1.

Jackson, E. *et al.* Chemical and structural analysis on magnetic tunnel junctions using a decelerated scanning electron beam. *Sci Rep*, **8**, 7585 (2018)

The following work is partially discussed in both section 5.3 and chapter 7.

Jackson, E. *et al.* Nondestructive imaging for quality assurance of magnetoresistive random access memory junctions. *J. Phys. D: Appl. Phys*, **53**, 14004-14015 (2020)

The remaining two publications were not discussed in this thesis, but were contributed to.

Yamaguchi, A.*et al.* Controllability of cupric particle synthesis by linear alcohol chain number as additive and pH control in cupric acetate solution using X-ray radiolysis. *J. Synchrotron Rad*, **26**, 1986-1995 (2019)

Ogasawara, T, *et al.* In-plane and perpendicular exchange bias effect induced by an antiferromagnetic $D0_{19}$ $Mn_2FeGa$ thin film. *J. Magn. Magn. Mater*, **484**, 307-312 (2019)

# Appendix B

# Technique Development

This Appendix supplements Chapter 4. Below is the code used to manually align, compare and subtract two electron images with different voltages. This was coded in the MATLAB environment.

```
%Purple is A, green is B

A = imread('image002.bmp'); %higher voltage
B = imread('image034.bmp'); %lower voltage

%crops the information from the black bar leaving just the photo
A2 = imcrop(A,[0 0 1280 960]);
B2 = imcrop(B,[0 0 1280 960]);

%readjusts the intensity values of the photos. it saturates
%the bottom and top 1% of all pixels
A3 = imadjust(A2);
B3 = imadjust(B2);

%this uses manually chosen control points to translate and
%transform the lower voltage image to match the
%higher voltage image
[Apoints,Bpoints] = cpselect(B3,A3,'Wait',true);
Bpoints2 = cpcorr(Bpoints,Apoints,B3,A3);
tIC = fitgeotrans(Apoints,Bpoints2,'nonreflectivesimilarity');
RB = imref2d(size(B3));
movingIC = imwarp(B3,tIC,'OutputView',RB);
```

```
%performs and plots a pixel by pixel comparison.
h = figure, imshowpair(movingIC,A3);
title('7keV(Magenta)␣versus␣6keV(Green)␣comparison');
saveas(h, 'Comparison.bmp');

C = imsubtract(movingIC,A3);

g = figure, imshow(C);
title('7keV␣versus␣6keV␣subtraction');
saveas(g, 'Subtraction.bmp');

C2 = imadjust(C);

f = figure, imshow(C2);
title('7keV␣versus␣6keV␣subtraction␣adjusted');
saveas(f, 'AdjustedSubtraction.bmp');
```

Below are further results for section 4.2. These extra results aim to assist in demonstrating the argument made in the main text.

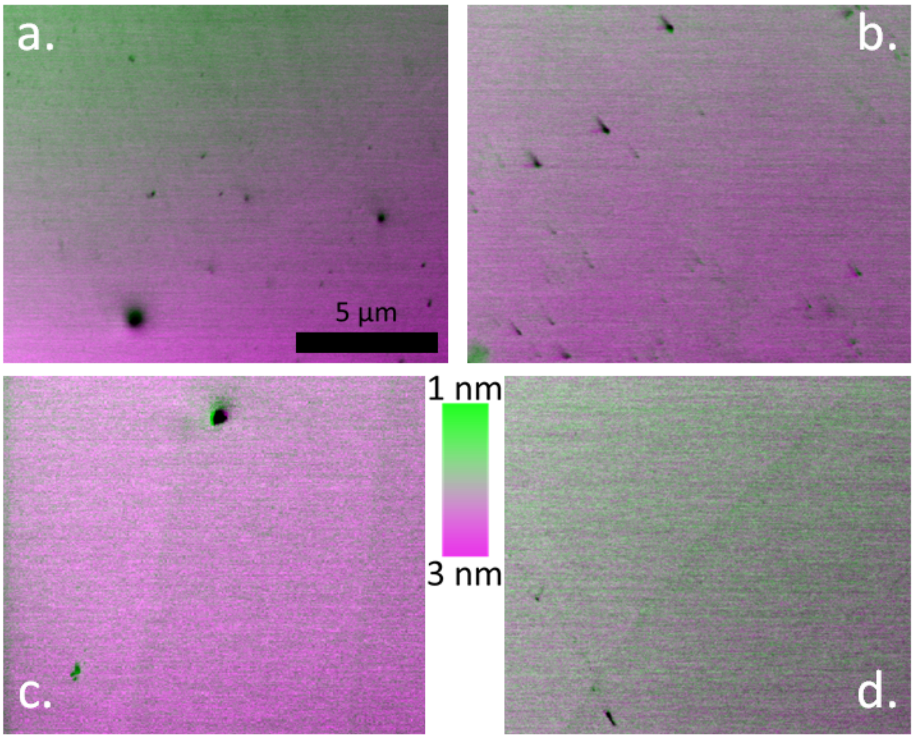

Figure B.1: Further comparison images for samples a.1, b.2, c.3 and d.4. These focus on the Ta/MgO interface. The structure of these samples can be found in table 4.1.

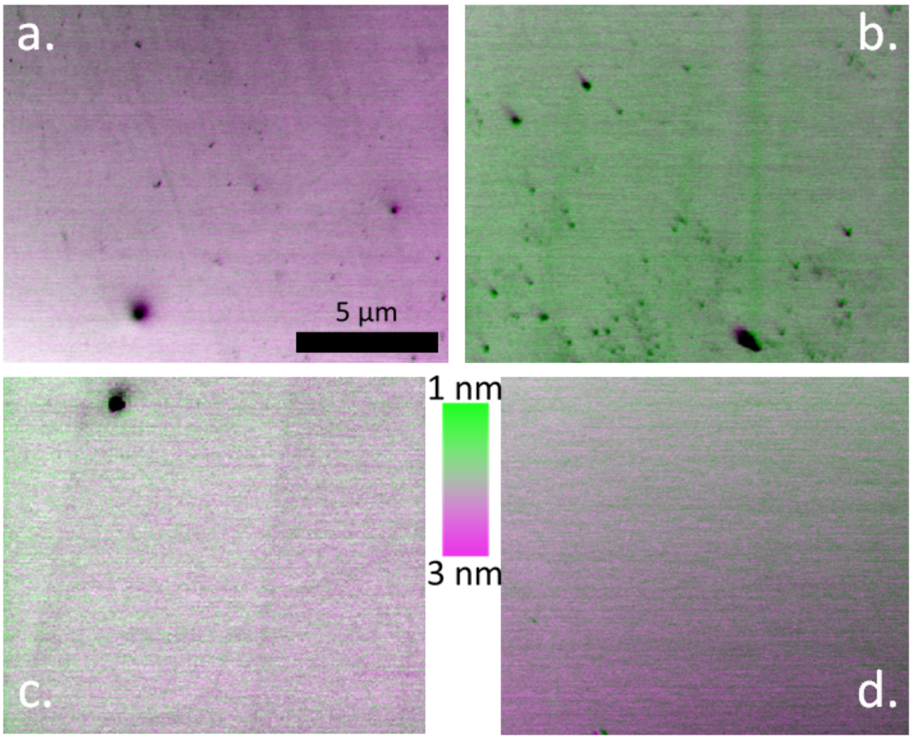

Figure B.2: Further comparison images for samples a.1, b.2, c.3 and d.4. These focus on the CoFeB/MgO interface. The structure of these samples can be found in table 4.1.

# List of Acronyms and Abbreviations

| Notation | Description | Page List |
|---|---|---|
| BSE | backscattered electron | 20–24, 26, 28, 36, 40, 43–52, 62, 63, 66, 74, 76, 77, 81, 82, 99, 102, 106, 124–126, 131 |
| CASINO | Monte Carlo simulation of electron trajectory in solids | 39, 43–47, 50, 58–61, 63, 64, 73, 76, 88, 97, 98, 112, 130, 134 |

| Notation | Description | Page List |
|---|---|---|
| CFMS | $Co_2Fe_{0.4}Mn_{0.6}Si$ | 86, 88, 89, 95, 103, 108, 109 |
| CoPc | Cobalt(II) Phthalocyanine | 111, 112, 115, 116, 118–120 |
| DRAM | dynamic random access memory | 85 |
| EDX | energy dispersive X-ray spectroscopy | 6, 33–37, 91, 94, 103, 110, 120, 124, 134, 137 |
| FIB | focussed ion beam | 1, 31, 32, 105, 107, 112, 120, 122 |
| GBSH | gentle beam super high resolution | 105 |
| $LaB_6$ | Lanthanum Hexaboride | 9–11 |
| LED | lower electron detector | 22–26 |
| MBE | molecular beam epitaxy | 112, 129, 137 |

| **Notation** | **Description** | **Page List** |
|---|---|---|
| MR | magnetoresistance | 86 |
| MRAM | magnetoresistive random access memory | 1, 85, 102, 104 |
| MTJ | magnetic tunnel junction | 85–88, 96, 98, 103, 110, 111, 135 |
| PIPS | precision ion polishing system | 31, 32 |
| QA | quality assurance | 96 |
| RA | resistance-area product | 86, 87, 94, 105 |
| RHEED | reflection high energy electron diffraction | 112 |
| SE | secondary electron | 20–25, 28, 43, 48–52, 57, 98 |

| **Notation** | **Description** | **Page List** |
|---|---|---|
| SEM | scanning electron microscope | 3, 6, 13–16, 18–22, 25–30, 36–43, 46–49, 54, 63, 65, 66, 68, 89, 91, 94, 101–103, 105, 106, 112, 114–118, 124, 125, 127, 128, 130, 133, 136 |
| TE | transmission electron | 28, 30, 47, 52 |

| Notation | Description | Page List |
|---|---|---|
| TEM | transmission electron microscope | 2, 3, 6, 28, 30–32, 38, 40–43, 47, 48, 52, 103, 105, 108, 109, 112, 114, 120, 122, 124, 135–137 |
| TMR | tunnelling magnetoresistance | 86–91, 94, 95, 104, 105, 108–110, 134, 135 |
| UED | upper electron detector | 24–26 |
| UHV | ultra-high vacuum | 86, 96, 129 |
| VSM | vibrating sample magnetometer | 80, 81 |
| XRR | X-ray reflectivity | 2, 107, 108 |

# List of Symbols and Units

| Notation | Description | Page List |
|---|---|---|
| $C$ | weight fraction | 62 |
| $C_\mathrm{s}$ | chromatic aberration coefficient | 18 |
| $C_\mathrm{s}$ | spherical aberration coefficient | 17 |
| $E$ | energy of a photon | 33 |
| $E_B$ | beam energy | 18–21 |
| $I_c$ | current through coil | 14 |
| $J$ | mean ionisation potential | 62 |
| $K$ | variable dependant on atomoic number | 62 |
| $L$ | distance between two collisions | 61, 62 |
| $N$ | number of turns in a coil | 14 |
| $N_0$ | Avogadro's number | 41 |
| $R$ | random number | 61 |
| $U$ | overvoltage | 55 |
| $V$ | acceleration voltage | 8, 28 |
| $V_0$ | beam accelerating vltage | 14 |
| $\Delta\mathrm{E}$ | change in energy | 55 |
| $\Delta E_B$ | energy spread of the beam | 8, 18–20 |
| $\Omega$ | solid angle | 21 |
| $\Phi$ | work function | 10 |
| $\Psi$ | take-off angle | 21 |
| $\alpha$ | screening parameter | 40 |
| $\alpha_0$ | beam divergence | 7, 18 |
| $\alpha_S$ | angle subtended by source on specimen | 8 |
| $\alpha_\mathrm{p}^2$ | probe convergence angle | 19 |
| $\alpha_a$ | angle subtended after the aperture | 18 |

| **Notation** | **Description** | **Page List** |
|---|---|---|
| $\alpha_o$ | angle of the outer ray | 17 |
| $\beta$ | brightness | 7, 19 |
| $\delta$ | secondary electron coeficient | 50–52 |
| $\epsilon$ | peak absorption | 33 |
| $\eta$ | coefficient of backscattering | 50–52 |
| $\eta(\phi_0)$ | angular coefficient of backscattering | 52 |
| $\eta_n$ | coefficient of backscattering at the normal | 52 |
| $\lambda$ | electron wavelength | 7, 8 |
| $\lambda_c$ | coherence length | 8 |
| $\lambda_{el}$ | mean free path | 41, 62 |
| $f$ | focal length | 14, 17 |
| $\mu$A | micro Amp | 31, 86 |
| $\mu$eV | micro electron volt | 12 |
| $\mu$m | micrometre | 9, 10, 31, 32, 43, 79, 86, 104, 117, 119, 129–131 |
| $\mu\mathrm{m}^2$ | micrometer squared | 37 |
| $\omega$ | fluorescence yield | 57 |
| $\overline{\nu}$ | electron velocity | 8, 15 |
| $\overline{\mathrm{B}}$ | magnetic field strength | 15 |
| $\overline{\mathrm{E}}$ | electric field strength | 15 |
| $\overline{\mathrm{F}}_L$ | Lorentz force | 14 |
| $\phi_0$ | specified angle | 40, 52 |
| $\rho$ | volumetric density | 41 |
| $\sigma_{el}$ | elastic cross section | 40, 44, 62 |
| $\sigma_{xc}$ | characteristic x-ray cross section | 55 |
| $\mathrm{E}_c$ | critical ionisation energy | 55, 56 |

| Notation | Description | Page List |
|---|---|---|
| $\theta$ | angle of incidence | 44–47 |
| $b_s$ | x-ray related, shell specific constant | 55 |
| $c_s$ | x-ray related, shell specific constant | 55 |
| $d$ | CASINO beam diameter | 61 |
| $dE$ | rate of energy loss | 42 |
| $d_0$ | diameter of crossover/focus point | 7 |
| $d_{\mathrm{G}}$ | aberration-free probe diameter | 19 |
| $d_{\mathrm{c}}$ | diameter of the chromatic aberration disk of least confusion | 18 |
| $d_{\mathrm{d}}$ | contribution of the aperture diffraction to the spot size | 18 |
| $d_{\mathrm{p}}$ | probe diameter | 19, 20 |
| $d_{\mathrm{s}}$ | diameter of the spherical aberration disk of least confusion | 17 |
| $d_c$ | effective source size for coherent illumination | 8 |
| $ds$ | distance travelled | 42 |
| $e$ | charge of an electron | 8, 15, 42 |
| $h$ | Planck's constant | 8, 56 |
| $i_{\mathrm{p}}$ | probe current | 19, 20 |
| $i_e$ | total emission current | 7 |
| $k_1$ | first Fowler-Nordheim constant | 12 |
| $k_2$ | second Fowler-Nordheim constant | 12 |
| $m_0$ | rest mass of electron | 8 |
| $n$ | maximum number of charges a photon will produce | 33 |
| $n_B$ | number of beam electrons | 50 |
| $n_s$ | number of electrons in a shell or subshell | 55 |
| $n_{BSE}$ | number of backscattered electrons | 50 |
| $n_{SE}$ | number of secondary electrons | 50 |
| $q$ | charge | 14, 15 |
| $r_{\mathrm{min}}$ | minimum radius of resolution | 30 |
| $r_{\mathrm{th}}$ | radius of the Airy disk | 29 |
| $v$ | frequency | 55 |

| Notation | Description | Page List |
|---|---|---|
| A | atomic weight of specimen | 41 |
| A | Ampere | 10, 12, 13, 130–133 |
| $A_C$ | absorption correction | 35 |
| $A_C$ | Richardson's constant | 10 |
| C | Coulomb | 33 |
| cm | centimetre | 41, 42, 94 |
| $cm^2$ | centimetre squared | 10, 12, 13, 40, 41 |
| $cm^3$ | centimetre cubed | 41 |
| $E_e$ | electron energy | 40, 42–45, 47, 51, 54, 56, 62 |
| $E_{ap}$ | applied electric field | 12 |
| eV | electron volt | 4, 10–14, 20, 21, 33, 34, 40, 49, 54 |
| $F_C$ | fluorescence correction | 35 |
| J | average energy loss per event | 42, 43 |
| $J_C$ | current density | 10, 12, 20 |
| K | Kelvin | 9, 13, 14, 94 |
| k | element specific variable | 42, 43 |
| $k_B$ | Boltzmann's constant | 10 |

| Notation | Description | Page List |
|---|---|---|
| keV | kilo electron volt | 12, 13, 19, 20, 22, 25, 26, 28, 30, 34, 35, 39, 41–43, 45–47, 51, 54, 58, 62, 63, 68, 70–72, 76–79, 82, 126 |
| kV | kilo volt | 4, 10, 11, 14, 22, 27, 31, 78, 81, 86, 88, 89, 91, 94, 95, 97, 99, 103, 105, 106, 108, 112, 114, 115, 120, 126, 128, 130 |

| Notation | Description | Page List |
|---|---|---|
| $m_s$ | saturation magnetisation | 81 |
| mA | milliAmp | 95 |
| mm | millimetres | 2, 14, 26, 30, 116, 118 |
| $mm^2$ | square millimeter | 10, 105 |
| mrad | milliradian | 39, 42, 55 |
| nm | nanometre | ii, 2–4, 11–13, 20, 27, 28, 30–32, 41–43, 45, 49, 60–62, 70, 71, 78, 79, 84, 91, 95, 96, 98–100, 102, 104–109, 115, 116, 118–124, 129, 130, 134–137 |

| **Notation** | **Description** | **Page List** |
|---|---|---|
| Pa | Pascals | 10, 11, 13, 14, 115 |
| sr | steradian | 10, 12, 13, 21, 53, 55 |
| T | temperature | 10 |
| T | tesla | ii, 16, 75, 81 |
| V | volt | 12, 14, 95, 130 |
| Z | atomic number | 35–37, 40, 41, 43, 44, 46–48, 50, 51, 54, 56, 57, 62, 63, 74, 115, 126, 137 |

# References

[1] J.R. Thomson. The Second Industrial Revolution A Brief History of Computing. In *High Integrity Systems and Safety Management in Hazardous Industries*, pages 127–136. Elsevier, 2015.

[2] D Kahng and MM Atalla. Silicon-silicon dioxide field induced surface devices, IRE-AIEEE Solid-State Device Research Conference, Carnegie Institute of Technology. 1960.

[3] Gordon E. Moore. Cramming more components onto integrated circuits, Reprinted from Electronics, volume 38, number 8, April 19, 1965, pp.114 ff. *IEEE Solid-State Circuits Society Newsletter*, 11(3):33–35, feb 2009.

[4] Sabpreet Bhatti, Rachid Sbiaa, Atsufumi Hirohata, Hideo Ohno, Shunsuke Fukami, and S N Piramanayagam. Spintronics based random access memory: a review . *Materials Today d*, 20(9), 2017.

[5] Johan Åkerman. Toward a universal memory. *Science*, 308(5721):508–510, apr 2005.

[6] Atsufumi Hirohata, Yasuaki Yamamoto, Benedict A. Murphy, and Andrew J. Vick. Non-destructive imaging of buried electronic interfaces using a decelerated scanning electron beam. *Nature Communications*, 7:12701, 2016.

[7] W H Bragg and W L Bragg Apr. The Reflection of X-rays by Crystals. *Proceedings of the Royal Society A: Mathematical, Physical and Engineering Sciences*, 88(605), 1913.

[8] J Goldstein, D E Newbury, D C Joy, C E Lyman, P Echlin, E Lifshin, L Sawyer, and J R Michael. *Scanning Electron Microscopy and X-ray Microanalysis: Third Edition.* Springer US, 2013.

[9] David B Williams and C Barry Carter. *Transmission Electron Microscopy: A Textbook for Materials Science.* Plenum Press, 1996.

[10] JEOL. *JSM-7800F Prime User Manual*. JEOL Ltd., Tokyo, 2015.

[11] T Wells and M El-Gomati. The energy spread of a LaB6 cathode operated in the virtual source mode. *Journal of Physics: Conference Series*, 522(1):012054, jun 2014.

[12] M E Haine and P A Einstein. Characteristics of the hot cathode electron microscope gun. *British Journal of Applied Physics*, 3(2):40–46, feb 1952.

[13] M.E. Haine and V.E. Cosslett. *The Electron Microscope*. Interscience Publishers, New York, 1961.

[14] C.R. Crowell. The Richardson constant for thermionic emission in Schottky barrier diodes. *Solid-State Electronics*, 8(4):395–399, apr 1965.

[15] W.F. Gale and T.C. Totemeier. *Smithells Metals Reference Book*. Butterworth-Heinemann, London, eighth edi edition, 2003.

[16] J. M. Lafferty. Boride Cathodes. *Journal of Applied Physics*, 22(3):299–309, mar 1951.

[17] A. J. Melmed and R. Gomer. Field Emission from Whiskers. *The Journal of Chemical Physics*, 34(5):1802–1812, may 1961.

[18] W. A. de Heer, A. Chtelain, and D. Ugarte. A Carbon Nanotube Field-Emission Electron Source. *Science*, 270(5239):1179–1180, nov 1995.

[19] R. H. Fowler and L. Nordheim. Electron Emission in Intense Electric Fields. *Proceedings of the Royal Society A: Mathematical, Physical and Engineering Sciences*, 119(781):173–181, may 1928.

[20] Shi-Dong Liang. *Quantum Tunneling and Field Electron Emission Theories*. WORLD SCIENTIFIC, apr 2014.

[21] L.W. Swanson and D. Tuggle. Recent progress in thermal field electron source performance. *Applications of Surface Science*, 8(1-2):185–196, may 1981.

[22] D. W. Tuggle, J. Z. Li, and L. W. Swanson. Point cathodes for use in virtual source electron optics. *Journal of Microscopy*, 140(3):293–301, dec 1985.

[23] P. W. Hawkes. *Electron optics and electron microscopy*. Taylor and Francis, 1972.

[24] T Mulvey and M J Wallington. Electron lenses. *Reports on Progress in Physics*, 36(4):347–421, apr 1973.

[25] Ludwig Reimer. Elements of a Transmission Electron Microscope. In *Transmission Electron Microscopy Physics of Image Formation and Microanalysis*, pages 86–135. Springer-Verlag Berlin Heidelberg, 1993.

[26] Oliver C. Wells. *Scanning electron microscopy.* McGraw-Hill, 1974.

[27] Charles William. Oatley. *The Scanning electron microscope.* Cambridge University Press, 1972.

[28] R F W Pease and W C Nixon. High resolution scanning electron microscopy. *Journal of Scientific Instruments*, 42(2):81–85, feb 1965.

[29] H. Boersch. Experimentelle Bestimmung der Energieverteilung in thermisch ausgeloesten Elektronenstrahlen. *Zeitschrift fuer Physik*, 139(2):115–146, apr 1954.

[30] Zhifeng Shao and A.V. Crewe. On the resolution of the low-energy electron reflection microscope. *Ultramicroscopy*, 31(2):199–203, oct 1989.

[31] T E Everhart and R F M Thornley. Wide-band detector for micro-microampere low-energy electron currents. *Journal of Scientific Instruments*, 37(7):246–248, jul 1960.

[32] Ankur Chauhan. Deformation and damage mechanisms of ODS steels under high-temperature cyclic loading. *Internation Journal of Fatigue*, 93:1–17, 2018.

[33] Klaus-Ruediger Peters. Scanning Electron Microscopy: Contrast at High Magnification. In *Proceedings of the 19th Annual Conference of the Microbeam Analysis Society*, pages 77–80, 1984.

[34] Luděk Frank, Richard Steklý, Martin Zadražil, Mohamed M. El-Gomati, and Ilona Müllerová. Electron Backscattering from Real and In-Situ Treated Surfaces. *Mikrochimica Acta*, 132(2):0179–0188, apr 2000.

[35] L.A. Giannuzzi and F.A. Stevie. A review of focused ion beam milling techniques for TEM specimen preparation. *Micron*, 30(3):197–204, jun 1999.

[36] Joachim Mayer, Lucille A. Giannuzzi, Takeo Kamino, and Joseph Michael. TEM Sample Preparation and FIB-Induced Damage. *MRS Bulletin*, 32(05):400–407, may 2007.

[37] Kieth Thompson. Technical Note 52342 - Silicon Drift Detectors. Technical report, Thermo Fischer Scientific.

[38] Emilio Gatti and Pavel Rehak. Semiconductor drift chamber  An application of a novel charge transport scheme. *Nuclear Instruments and Methods in Physics Research*, 225(3):608–614, sep 1984.

[39] C E Fiori and D E Newbury. Artifacts in energy dispersive x-ray spectrometry in the scanning electron microscope (II). *Scanning electron microscopy*, (Pt 2):251–8, 250, 1980.

[40] Kurt F. J. Heinrich and Dale E. Newbury. *Electron probe quantitation.* Plenum Press, 1991.

[41] Jean-Louis Pouchou and Françoise Pichoir. Quantitative Analysis of Homogeneous or Stratified Microvolumes Applying the Model PAP. In *Electron Probe Quantitation*, pages 31–75. Springer US, Boston, MA, 1991.

[42] A. LeFurgey, S. D. Davilla, D. A. Kopf, J. R. Sommer, and P. Ingram. Real-time quantitative elemental analysis and mapping: microchemical imaging in cell physiology. *Journal of Microscopy*, 165(2):191–223, feb 1992.

[43] Pierre Hovington, Dominique Drouin, and Raynald Gauvin. CASINO: A new monte carlo code in C language for electron beam interaction -part I: Description of the program. *Scanning*, 19(1):1–14, 2006.

[44] E. Rutherford. LXXIX. The scattering of $\alpha$ and $\beta$ particles by matter and the structure of the atom. *The London, Edinburgh, and Dublin Philosophical Magazine and Journal of Science*, 21(125):669–688, may 1911.

[45] J. Henoc and F. Maurice. Characteristics of a Monte Carlo program for microanalysis study of energy loss. *NBS special publication*, 460:61–95, 1976.

[46] Raynald Gauvin and Dominique Drouin. A formula to compute total elastic mott cross-sections. *Scanning*, 15(3):140–150, 1993.

[47] N.F. Mott and H.S.W. Massey. *The Theory of Atomic Collisions.* Clarendon Press, Oxford, third edit edition, 1965.

[48] H. Bethe. Zur Theorie des Durchgangs schneller Korpuskularstrahlen durch Materie. *Annalen der Physik*, 397(3):325–400, jan 1930.

[49] Martin J. Berger and Stephen M. Seltzer. Tables of Energy Losses and Ranges of Electrons and Positrons. NASA SP-3012. *Tables of Energy Losses and Ranges of Electrons and Positrons. NASA SP-3012, by Martin J. Berger and Stephen M. Seltzer, 127 pages, published by NASA, Washington, D.C., 1964*, 3012, 1964.

[50] D. C. Joy and S. Luo. An empirical stopping power relationship for low-energy electrons. *Scanning*, 11(4):176–180, jan 1989.

[51] T.E. Everhart and T.L. Hayes. The scanning electron microscope. *Scientific American*, 226(1):55–69, 1972.

[52] K Kanaya and S Okayama. Penetration and energy-loss theory of electrons in solid targets. *Journal of Physics D: Applied Physics*, 5(1):308, jan 1972.

[53] T Koshikawa and R Shimizu. A Monte Carlo calculation of low-energy secondary electron emission from metals. *Journal of Physics D: Applied Physics*, 7(9):318, jun 1974.

[54] Dale E. Newbury and Robert L. Myklebust. Monte carlo electron trajectory simulation of beam spreading dm thin foil targets. *Ultramicroscopy*, 3:391–395, jan 1978.

[55] David C. Joy. A model for calculating secondary and backscattered electron yields. *Journal of Microscopy*, 147(1):51–64, jul 1987.

[56] H Seiler. Secondary electron emission in the scanning electron microscope. *Journal of Applied Physics*, 54(11):R1–R18, nov 1983.

[57] K.F.J. Heinrich. Electron probe microanalysis by specimen current measurement. *X-ray Optics and Microanalysis*, pages 159–167, 1966.

[58] D.B. Wittry. *Proceedings of the 4th International Conference on X-Ray Optics and Microanalysis.* Hermann, Paris, 1966.

[59] H Bishop. *Proceedings of the 4th International Conference on X-Ray Optics and Microanalysis.* Hermann, Paris, 1966.

[60] L. Reimer and C. Tollkamp. Measuring the backscattering coefficient and secondary electron yield inside a scanning electron microscope. *Scanning*, 3(1):35–39, 1980.

[61] Rolf Woldseth. *All you ever wanted to know about x-ray energy spectrometry.* Kevex Corporation, 1973.

[62] United States. National Bureau of Standards and Charlotte E Moore. *Atomic Energy Levels - As Derived From the Analyses of Optical Spectra.* U.S. Department of Commerce, Michigan, 1971.

[63] C. J. Powell. Cross sections for ionization of inner-shell electrons by electrons. *Reviews of Modern Physics*, 48(1):33–47, jan 1976.

[64] S.J.B Reed. *Electron Microprobe Analysis and Scanning Electron Microscopy in Geology.* Cambridge University Press, Cambridge, UK, 2005.

[65] D. Briggs and J.T. Grant. *Surface Analysis by Auger and x-Ray Photoelectron Spectroscopy.* Murray Media, North Miami Beach, 2003.

[66] Dominique Drouin, Alexandre Réal Couture, Dany Joly, Xavier Tastet, Vincent Aimez, and Raynald Gauvin. CASINO V2.42 - A fast and easy-to-use modeling tool for scanning electron microscopy and microanalysis users. *Scanning*, 29(3):92–101, 2007.

[67] Dominique Drouin, Pierre Hovington, and Raynald Gauvin. CASINO: A new monte carlo code in C language for electron beam interactions-part II: Tabulated values of the mott cross section. *Scanning*, 19(1):20–28, 2006.

[68] Raynald Gauvin and Gilles L'Espérance. A Monte Carlo code to simulate the effect of fast secondary electrons on $\kappa$AB factors and spatial resolution in the TEM. *Journal of Microscopy*, 168(2):153–167, nov 1992.

[69] Hendrix Demers, Nicolas Poirier-Demers, Alexandre Réal Couture, Dany Joly, Marc Guilmain, Niels De Jonge, and Dominique Drouin. Three-dimensional electron microscopy simulation with the CASINO Monte Carlo software. *Scanning*, 33(3):135–146, 2011.

[70] C. Zhang, S. Fukami, H. Sato, F. Matsukura, and H. Ohno. Spin-orbit torque induced magnetization switching in nano-scale Ta/CoFeB/MgO. *Applied Physics Letters*, 107(1):012401, jul 2015.

[71] Edward Jackson, Mingling Sun, Takahide Kubota, Koki Takanashi, and Atsufumi Hirohata. Chemical and structural analysis on magnetic tunnel junctions using a decelerated scanning electron beam. *Scientific Reports*, 8(1):7585, 2018.

[72] William Frost, Marjan Samiepour, and Atsufumi Hirohata. Low-temperature crystallisation of Heusler alloy films with perpendicular magnetic anisotropy. *Journal of Magnetism and Magnetic Materials*, 484:100–104, aug 2019.

[73] P. K. Manna and S. M. Yusuf. Two interface effects: Exchange bias and magnetic proximity. *Physics Reports*, 535(2):61–99, feb 2014.

[74] Mingling Sun, Takahide Kubota, Shigeki Takahashi, Yoshiaki Kawato, Yoshiaki Sonobe, and Koki Takanashi. Buffer layer dependence of magnetoresistance effects in Co 2 Fe 0.4 Mn 0.6 Si/MgO/Co 50 Fe 50 tunnel junctions. *AIP Advances*, 8(5):055902, may 2018.

[75] Jiuqiang Li, Guangqing Zhang, Dongsheng Liu, and Oleg Ostrovski. Low-temperature Synthesis of Aluminium Carbide. Technical Report 6, 2011.

[76] M W Chase, National Institute of Standards (U.S.), and Technology. *NIST-JANAF thermochemical tables.* American Chemical Society ; American Institute of Physics for the National Institute of Standards and Technology, [Washington, D.C.]; Woodbury, N.Y., 1998.

[77] K. Z. Suzuki, Y. Miura, R. Ranjbar, L. Bainsla, A. Ono, Y. Sasaki, and S. Mizukami. Perpendicular magnetic tunnel junctions with Mn-modified ultrathin MnGa layer. *Applied Physics Letters*, 112(6), feb 2018.

[78] Manoj Kumar Yadav, Santosh Kumar Gupta, Sanjeev Rai, and Avinash C. Pandey. Al embedded MgO barrier MTJ: A first principle study for application in fast and compact STT-MRAMs. *Superlattices and Microstructures*, 103:314–324, mar 2017.

[79] E. Chason and T. M. Mayer. Thin film and surface characterization by specular X-ray reflectivity. *Critical Reviews in Solid State and Materials Sciences*, 22(1):1–67, 1997.

[80] E Jackson, Y Wu, W Frost, J-Y Kim, M Samiepour, K Elphick, M Sun, T Kubota, K Takanashi, T Ichinose, S Mizukami, and A Hirohata. Non-

destructive imaging for quality assurance of magnetoresistive random-access memory junctions. *J. Phys. D: Appl. Phys*, 53:14004–14015, 2020.

[81] K. S. Novoselov, A. K. Geim, S. V. Morozov, D. Jiang, Y. Zhang, S. V. Dubonos, I. V. Grigorieva, and A. A. Firsov. Electric field in atomically thin carbon films. *Science*, 306(5696):666–669, oct 2004.

[82] Qiang Liu, Lei Gao, Xingsong Su, Fei Zhou, and Guotao Duan. Interfacial self-assembly of CoPc thin films with their high sensing use as NO2 sensors. *Materials Chemistry and Physics*, 234:94–101, may 2019.

[83] Tsunenori Sakamoto. Rheed Oscillations in MBE and Their Applications to Precisely Controlled Crystal Growth. In *Physics, Fabrication, and Applications of Multilayered Structures*, pages 93–110. Springer US, 1988.

[84] L. R. Fleet, K. Yoshida, H. Kobayashi, Y. Kaneko, S. Matsuzaka, Y. Ohno, H. Ohno, S. Honda, J. Inoue, and A. Hirohata. Correlating the interface structure to spin injection in abrupt Fe/GaAs(001) films. *Physical Review B*, 87(2):024401, jan 2013.